ANALYSIS OF WEAR AND CORROSION PROPERTIES OF 316 L STAINLESS STEEL ADDITIVELY MANUFACTURED USING LASER ENGINEERED NET SHAPING (LENS®)

By

NAVIN SAKTHIVEL

Bachelor of Engineering in Mechanical Engineering

Anna University

Chennai, India

2016

Submitted to the Faculty of the
Graduate College of the
Oklahoma State University
in partial fulfillment of
the requirements for
the Degree of
MASTER OF SCIENCE
July, 2018

ANALYSIS OF WEAR AND CORROSION

PROPERTIES OF 316 L STAINLESS STEEL

ADDITIVELY MANUFACTURED USING LASER

ENGINEERED NET SHAPING (LENS®)

Thesis Approved:

Dr. Sandip P. Harimkar

Thesis Adviser

Dr. James A. Kidd

Dr. Ranji K. Vaidyanathan

Dr. Hitesh D. Vora

Name: NAVIN SAKTHIVEL

Date of Degree: JULY, 2018

Title of Study: ANALYSIS OF WEAR AND CORROSION PROPERTIES OF 316 L STAINLESS STEEL ADDITIVELY MANUFACTURED USING LASER ENGINEERED NET SHAPING (LENS®)

Major Field: MECHANICAL AND AEROSPACE ENGINEERING

Abstract: Additively manufactured stainless steel 316 L complex shaped components are used in various industries like oil and gas, chemical industries etc. for its excellent corrosion resistance and tribological properties. Additive manufacturing of stainless steel 316 L is inevitable in the applications requiring complex shapes, which cannot be manufactured conventionally. In such applications, complex shaped components are fabricated using additive manufacturing. Due to laser melting and rapid solidification in the layer-by-layer densification in additive manufacturing, the microstructural evolution in additive manufacturing is drastically different from conventional manufacturing methods. This results in difference in the electrochemical and tribological behavior of additively manufactured stainless steel 316 L. In this research, corrosion and wear properties of stainless steel 316 L additively manufactured using LENS® was analyzed. Samples were additively manufactured under different processing conditions of laser power, laser scanning speed and powder deposition rate. The results show that in the as-built surfaces, wear is found to be inversely proportional to the laser power. When the effect of surface roughness is eliminated, the wear is found to be directly proportional to laser power. Laser scan speed is found to be directly affecting the weight loss due to wear. The effect of powder deposition rate on the wear and corrosion characteristics of stainless steel 316 L additively manufactured using LENS® is found to be inconsistent. The corrosion potential of stainless steel 316 L additively manufactured using LENS® is lesser than that of wrought stainless steel 316 L. The corrosion potential of stainless steel 316 L additively manufactured using LENS® was higher than the wrought at high laser energy densities. The corrosion potential and subsequently corrosion resistance increased with laser power. It was observed that the additively manufactured stainless steel 316 L using LENS® shows improved pitting resistance than the wrought stainless steel 316 L. The stress relieving heat treatment imparted enhanced pitting corrosion resistance.

TABLE OF CONTENTS

Chapter Page

LIST OF TABLES

LIST OF FIGURES

CHAPTER I

AN OVERVIEW OF ADDITIVE MANUFACTURING AND STEEL

This chapter presents the background on steel, stainless steel, additive manufacturing, additive manufacturing of steel, corrosion and wear properties of stainless steel. It emphasizes the literature on the direct energy deposition of steel and the microstructure evolution and properties obtained during the direct energy deposition of steel.

1.1 Steel

Steel is an alloy of iron and carbon with the composition of carbon varying from 0.06% to 2.0%. Iron-carbon alloy system having carbon content less than 0.005% at room temperature is termed as commercially pure iron [1, 2]. The pure iron is very soft and ductile resulting in low strength. Steel is an iron-based alloy containing 0.06% to 2.0% carbon. Iron-carbon alloy possessing carbon content of more than 2% is termed as cast iron. Pure iron is not used in high strength applications but only in applications requiring magnetic properties [1, 2]. For high strength applications, iron is used in the form of steel. Pig iron containing 4% or 5% carbon is employed in the process of making steel [1, 2]. This composition of 4% or 5% carbon is too high to be used directly in steel. In addition, pig iron contains high amounts of silicon, sulfur, phosphorus, and manganese that are detrimental to the properties of steel [1, 2].

Hence, the pig iron is refined in the process of making steel. In the early days, Bessemer converter is used in the refining of pig iron to steel, which involved blasting air into molten iron to oxidize the excessive carbon content in the pig iron [1, 2]. Currently, the refining of pig iron to steel is accomplished in either (1) basic oxygen furnace (2) the open-hearth furnace (3) electric furnace [1, 2].

1.2 Stainless steel

Stainless steel is an iron-based alloy with a minimum of 10.5% chromium as the main alloying element. The susceptibility of corrosion decreases with the increase in chromium content. Though some tool steels exhibit 12% chromium content, they are not classified as stainless steel [2]. Therefore stainless steels are defined as steels that possess at least 10.5% chromium and exude passivity under oxidation in aqueous environments rendering them corrosion resistant. The innovative technique of adding chromium in low-carbon ferrochromium at the final stages of melting low-carbon steel revolutionized the production of stainless steel in the 1930s [2]. This is owing to the great affinity of chromium for carbon and oxygen. Nevertheless, the same property is responsible for the formation of the passivation layer of chromium. Stainless steel is broadly classified into ferritic stainless steel, martensitic stainless steel, austenitic stainless steel, (PH) alloys, duplex alloys. The composition of carbon in ferritic stainless steel is less than 0.2% and chromium content ranges from 16% - 20% [2]. Ferritic stainless steel has body-centered cubic ferrite microstructure and is brittle in nature. The composition of chromium in martensitic stainless steel varies from 12% to 18% and the carbon content is about 1.2%. They possess body-centered tetragonal martensitic microstructure and are capable of hardening by heat treatment [2]. The precipitation hardened (PH) stainless steels are martensitic stainless steels with low carbon content with specific chromium to nickel ratios like 13:8, 15:5, 17:4. They possess very high strengths and hardness higher than martensitic alloys. Duplex alloys are a class of stainless steels that are a combination of ferrite (α) and austenite (γ) phase to encompass the advantages of both phases [2].

Austenitic steels are an important classification of stainless steel with very low carbon content, chromium composition ranging from 16% to 26% and nickel content varying from 8% to 22%. The presence of nickel stabilizes the austenite phase to exist at room temperature. The austenite phase imparts ductility to the alloy [2].

1.3 Alloy variants of stainless steel

The ferritic stainless steel finds applications in environments highly susceptible to atmospheric corrosion and elevated temperature zones. Common types of ferritic stainless steel are 405,430, 430 F, 446 [2]. Martensitic stainless steels are employed for manufacturing structural components and cutting tools. Common types of martensitic stainless steel include 403, 410, 414, 416, 420, 431, 440 A, 440 B, 440 C [2]. Precipitation Hardened (PH) stainless steel types like 17-4, 15-5, 13-8, 17-7, 15-7 Mo are employed for applications in springs and structural members. Various types of austenitic stainless steel are 201, 202, 301, 302, 303, 304, 305, 308, 309, 310, 314, 316, 317, 321, 347, 304 L and 316 L [2]. The composition of stainless steel 316 L is given in table 1.

Table 1: Composition of stainless steel 316 L (Weight Percentage) [3]

C	Cr	Ni	Mo	Mn	Si	Fe
0.023	17.3	13.1	2.66	1.74	0.73	Balance

1.4 Microstructure of wrought stainless steel 316 L

The microstructure observed in wrought stainless steel 316 L is shown in Fig. 1.1 and Fig. 1.2. It can be seen that the grain size is in the range of 10 μm to 50 μm. The grains in the wrought hot rolled stainless steel 316 L are nearly equiaxed. The low magnification SEM micrograph shows porosities.

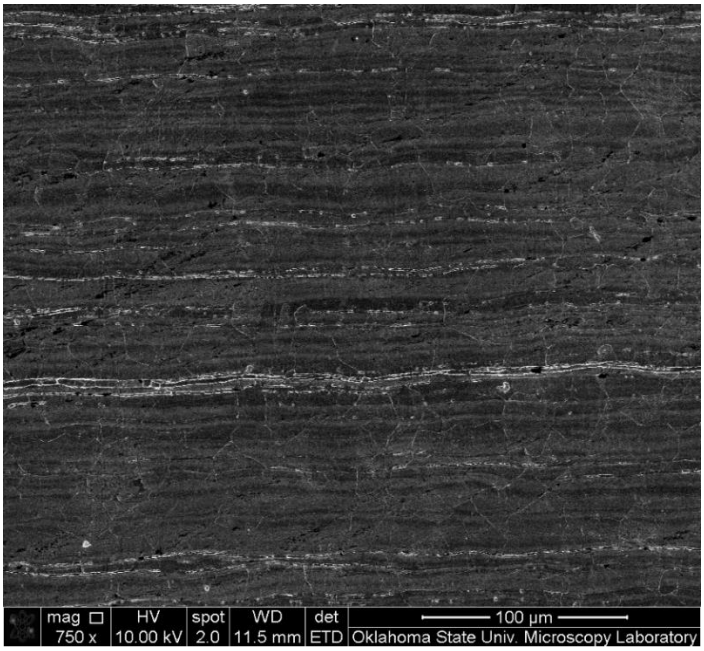

Fig. 1.1 High magnification SEM micrograph of wrought stainless steel 316 L

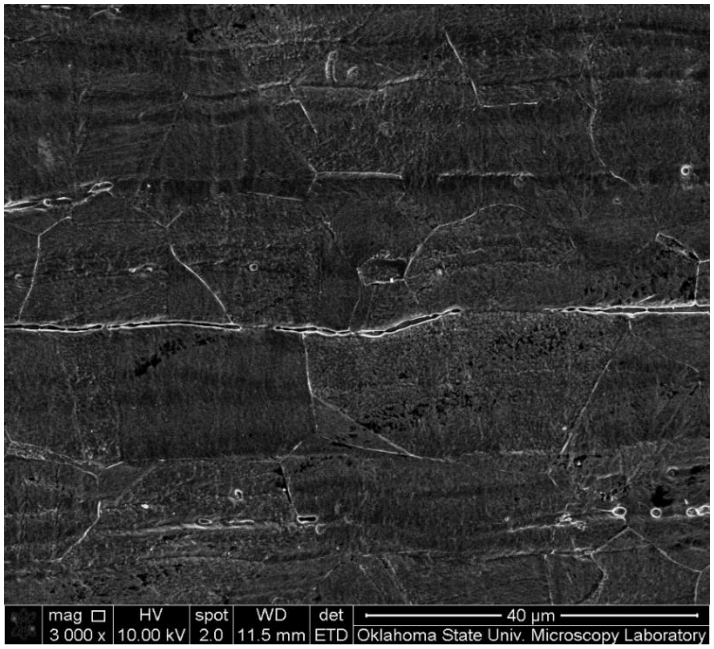

Fig.1.2 Low magnification SEM micrograph of wrought stainless steel 316 L

1.5 Additive manufacturing

Additive manufacturing is defined as “the process of fabricating an object from the 3D CAD file in layer by layer fashion by joining or adding the material while not involving material removal ” [4]. Additive manufacturing is classified into seven broad categories namely direct energy deposition, powder bed fusion, binder jetting, material jetting, material extrusion, vat polymerization and sheet lamination [5]. This is depicted in Fig. 1.3.

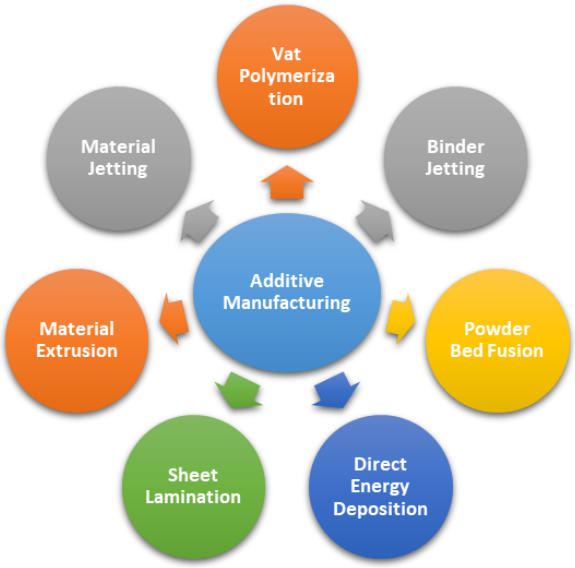

Fig. 1.3 Classification of additive manufacturing

The following sections present the wear mechanisms in steel, corrosion properties of the wrought and additively manufactured steel, effect of heat treatment on additively manufactured steel, thermal behavior and microstructural evolution in the LENS® process. The following sections also present the application of LENS® process in the development of complex alloys and composities, and the objectives of the current research.

1.6 Wear mechanisms in steel

The current research is focused on Laser Engineered Net Shaping (LENS®) process, which falls under the classification of direct energy deposition. This process involves selective deposition of metal powder and simultaneous irradiation of very high-intensity laser beam at the deposition site. Several publications have appeared in the recent years documenting various aspects of direct energy deposition and Laser Engineered Net Shaping (LENS®) process. This includes focus on the effect of processing parameters on mechanical properties, microstructural evolution, phase transformation, modeling etc. In this regard, much research has been done on direct energy deposition and Laser Engineered Net Shaping (LENS®) of steel. Z. Wang et al investigated the microstructural evolution and tensile properties of stainless steel 304 L during direct energy deposition. It was observed that the microstructure turned coarser along the build direction and lower heat input showed finer microstructure and higher yield strength [6].

X. Chen et al discussed the occurrence of γ, δ, σ phases during gas metal arc additive manufacturing. The micro-hardness in this work was observed to increase with the distance from the top surface [7]. The results obtained by Zhong et al during electron beam melting of stainless steel 316 L indicate that columnar grains of size 1 and 9 μm grow towards the temperature gradient. They also explained the reason for the absence of δ ferrite phase [8]. Inventors of LENS® process, David Keicher, and J. E. Smugeresky have researched several aspects of LENS® of stainless steel 316 L. In their research, the maximum surface finish of 8 μm, the maximum yield strength of 86 psi and maximum ultimate tensile strength of 117 ksi was obtained [9-12]. As reported by L. Wang et al, the laser power has to decrease linearly with build height and increase with scan speed for maintaining steady melt pool size during LENS® of stainless 410 [13]. They also observed the occurrence of residual stresses concomitant to high-temperature gradient [14]. R. S. Amano experimentally investigated the laser engineered net shaping (LENS®) of 4140 low alloy steel. Columnar grain structure oriented in the direction of heat flow was identified. The solidification

morphology was cellular to the dendritic and cooling rate of $10^2 - 10^3$ K/s existed during the process [15].

M. L. Griffith et al analyzed the thermal behavior in the H-13 tool steel with regard to the formation of residual stresses, which was found to be the consequence of temperature gradient. The high gradient in the middle regions of the build was observed to result in higher residual stresses. They summarize that at low energy density, low laser power, high scan speed, molten pool solidification is faster, which results in very high yield and ultimate tensile strength [16, 17]. B. Zheng et al heuristically investigated the microstructural evolution in the LENS® of stainless steel 316 L. They found that the melt pool area increased with laser power and cooling rate reduced with the distance from substrate [18, 19]. However, to the authors' best knowledge; very few publications are available in the literature that addresses the issue of wear properties of the additively manufactured material.

Literature shows some attempts to improve the wear performance of additively manufactured stainless steel 316 L components. E. Yasa et al found that laser remelting of SLM® stainless steel 316 improved the wear performance [20]. M. Makinen found that electroplating of nickel on additively stainless steel improves wear properties [21]. Bandar AlMangour et al employed shot peening technique as a post-processing method to improve the wear characteristics of additively manufactured 17-4 stainless steel [22]. R. P. Mudge et al proposed that the LENS® regenerated layer is more corrosion and wear resistant [23]. Y. Sun et al investigated the wear behavior of selective laser melting of 316 L stainless steel under dry sliding conditions. In this research, the effect of laser processing parameters and the wear was related to the percentage volume composition of porosity. They reported higher wear of SLM® stainless steel 316 L compared to wrought stainless steel 316 L. Severe wear was observed in the case of SLM® stainless steel 316 L whereas mild wear was observed in the hot rolled bulk wrought stainless steel 316 L sample. This was explained due to the porosity of the SLM® stainless steel 316 L [24]. The key limitation or gap in the above-delineated works is that they are not pertaining to the study of the wear properties

in direct energy deposition – laser engineered net shaping (LENS®) of stainless steel 316 L and heuristically investigate the effect of processing parameters on the wear properties.

Little attention has been paid to concomitantly juxtapose the microstructural evolution and the wear mechanism of material with the literature. Closest work is that of Y. Sun et al which deals with the wear properties of selectively laser-melted stainless steel 316 L [24]. During LENS®, the rapid solidification phenomenon and layer-by-layer deposition involving re-melting result in different wear characteristics when compared to conventional processes and other methods of additive manufacturing. Hence, the evaluation of wear characteristics in LENS® process is very significant need for the application of stainless steel 316 L in the industries previously mentioned.

1.7 Corrosion properties of wrought and additively manufactured steel

Stainless steel 316 L is an austenitic steel used in chemical industries, oil and gas industries, biomedical applications, pressure vessels, boilers and heat exchangers etc. for its excellent corrosion resistance properties. The corrosion resistance is due to the formation of passive chromium oxide film [25]. The corrosion resistance is uncompromised in the aqueous and aerated environment.

The thermal characteristics during the process determine the mechanical properties like strength, resilience, toughness, wear resistance etc. Also, the thermal history determines the phases of evolution and the recrystallization phenomenon as well. The complicated thermal history during the LENS® process is due to the number of heating-reheating cycles. The powders when deposited are laser heated instantly to form a molten pool, which undergoes rapid quenching. The rate of quenching decreases with subsequent layers of deposition [19]. J. E. Smugeresky et al found the correlation effect between the surface mechanical properties of finish and surface hardness to the thermal processing conditions [10]. They found that the best surface finish was obtained in 316 L stainless steel at a laser processing power of 325 W with an average flow rate and it is found to be independent of traverse speed. They also confounded the fact that best hardness values were

obtained when powder size is very fine and at the minimal possible laser power [10]. In the same 316 L stainless steel, high-density fine microstructure metallic parts were obtained when the powders were coaxially fed. The microstructure was found to coarsen when the deposition layer thickness increases. Microstructure homogeneity was found to be maintained when the laser power and laser traverse speed is controlled to maintain nearly constant melt pool size. Cooling rate between 10^3 and 10^4 K/s yields an optimum micro-hardness of 300 HV (3.18 GPa) [18].

During additive manufacturing or direction energy deposition or LENS® process, the rapid solidification phenomenon and layer by layer deposition involving re-melting result in distinct microstructures when compared to conventional processes where slow cooling occurs. In the wrought material, the microstructure is more homogenized. This has culminated in drastic changes in mechanical, chemical, tribological, corrosion properties of additively manufactured metals with property enhancement in some cases. The phases obtained in additive manufacturing are seldom uncommon in the cast and wrought material.

Corrosion properties of additively manufactured stainless steels show the paramount difference to their wrought manufactured counterparts. This is attributed to the increased Gibb's free energy of the grains resulting from additive manufacturing. The bonds at grain boundaries in additive manufacturing are strained resulting in increased Gibb's free energy. The increased Gibb's free energy drives the corrosion of the grains, which is in accordance with Nerst equation (1) .

$$\Delta G_i = -n_i F E \quad (1)$$

Where ΔG_i is the Gibb's free energy driving the corrosion, n_i is the charge exchanged in the corrosion, F is the Faraday's constant, E is the corrosion potential measured.

The microstructure of stainless steel 316 L manufactured in LENS® process shows non-uniform dendrites which affects corrosion characteristics of LENS® of stainless steel 316 L. The evaluation of corrosion properties of stainless steel 316 L processed by LENS® process is significant due to its applications in pressure vessels, biomedical implants, oil and gas industries, boilers and heat exchangers, marine applications. The literature on additive manufacturing is a testimony for the

opulence of research work on the mechanical behavior of additively manufactured steels. Very limited publications can be found delving on the corrosion properties of additively manufactured steels according to the authors' best knowledge. However, the following are the works on laser melting, laser re-melting, direct metal laser sintering of steels which precedent as precursors for the current research work. U. K. Mudali and R. K. Dayal studied the effect of laser surface melting of austenitic stainless steel 316 and found that the laser surface melting improves inter-granular corrosion resistance [26]. Surface modification of austenitic stainless steel by laser re-melting has been found to enhance corrosion resistance [27]. M. R. Stoudt et al investigated the influence of post-build microstructure on the electrochemical behavior and pitting corrosion resistance of Direct Metal Laser Sintered (DMLS®) 17-4 PH Stainless steel. They found that additively manufactured 17-4 PH stainless steel is more resistant to localized corrosion and pitting compared to wrought [28]. Sun et al say that reduced breakdown potential of SLM® stainless steel 316 L makes it more susceptible to corrosion [24].

Michal Zietala et al analyzed the corrosion properties of stainless steel 316 L fabricated using laser engineered net shaping LENS®. It was seen that the corrosion potential of stainless steel 316 L fabricated using LENS® and classical manufacturing methods are similar [29]. R. P. Mudge et al investigated the application of LENS® in repair and found that the regenerated layer is more corrosion resistant and wear resistant [23]. Similarly, D. D. Gu applied laser additive manufacturing to prepare wear resistant and corrosion resistant coatings [30]. Although several studies have indicated the corrosion behavior of additive manufacturing of stainless steel 316 L, no attention has been paid to investigate the effect of processing parameters on the corrosion characteristics in the LENS® of stainless steel 316 L. To the authors' knowledge, the corrosion characteristics of LENS® stainless steel 316 L have been scarcely investigated from the microstructural evolution point of view. This delineated gap established is the motivation of the current research to heuristically investigate the effect of LENS® parameters on the microstructure and concomitantly the effect of

microstructure on the potentiodynamic polarization corrosion characteristics of stainless steel 316 L.

1.8 Effect of heat treatment in additive manufacturing of steel

Residual stresses impose insidious implications in the processing and properties of metal additive manufacturing since inception. This is because the residual stresses directly correlate the internal strained bonds, dislocations to the macroscopic properties of tensile properties, hardness, surface finish, wear and corrosion properties. The residual stresses are results of rapid melting and rapid solidification, which is a virtue of laser-assisted processing. The residual stresses result in very serious repercussions like thermal distortion, dimensional inaccuracy, and surface finish and directly impair the material properties. Internally, the heat treatment relieves the stresses by accomplishing the phase transformations of a metastable phase to equilibrium phases and impart microstructural changes relieving strained incoherent compositions [31].

In some cases, heat treatment homogenizes non-homogeneous microstructures. On the mesoscale, the strained atomic bonds are thermally relaxed and evolve as strain free bonds in the event of stress relieving heat treatments. Literature is a testimony to the research work on the leveraging effects of heat treatment in all the techniques of additive manufacturing. They are delineated in the following sections.

Aref Yadollahi et al studied the effect of heat treatment on the mechanical and microstructural properties of stainless steel 316 L during Direct Laser Deposition (DLD), LENS® system was used in the process. Heat treatment was found to increase the size of grains. Microstructural homogenization was observed. The inter-layer porosity was observed to have vanished completely. The low angle grain boundaries were found to be transformed into high angle grain boundaries. Heat treatment has been found to induce twinning substructures. They are formed due to the lowering of interfacial free energy. Indeed, the formation of the high angle grain boundaries is the result of twin boundary disorientation. The ductility was found to increase substantially. Yield

strength was observed to decrease by 17% and ultimate tensile strength was found to decrease by 5%. However, no significant microstructural change was observed in the bottom, middle or in the top regions [32]. Aref Yadollahi et al investigated the effect of build orientation and heat treatment on the fatigue behavior of selective laser melting of 17-4 PH stainless steel. It was found that solution annealing and peak-aging resulted in the recrystallization and homogenization of microstructure. The hardness, fatigue life and tensile strength were found to be enhanced upon heat treatment [33]. The effect of heat treatment was investigated on the microstructure and mechanical properties of Selective Laser Melting (SLM®) of 18 Ni-300 steel by K. Kempen et al. Aging heat treatment is a recommended heat treatment for maraging steel. Hardness was found to be ameliorated by 20 HRC points. The nickel-rich intermetallic precipitates were uniformly distributed during gaining of martensite [34]. Z. H. Liu et al found that hardening and tempering heat treatment improved the hardness, fracture toughness and impact toughness of SLM® of M-2 high-speed steel parts [35]. H. Khalid Rafi et al recommended that post-process heat treatment is mandatory for achieving the required optimum tensile properties in 17-4 precipitation hardenable steel manufactured by SLM® process [36].

M. L. Montero Sistiaga et al exclusively studied the effect of heat treatment of 316 L stainless steel produced by SLM® technique. It was observed that the heat treatment above 950 ·C dissolved the network of cellular dendritic microstructure and no tangible grain morphology difference was observed. However, it had the detrimental effect on hardness, yield strength, and ultimate strength when compared to the as-built condition [37]. William E. Luecke and John A. Slotwinski et al found that annealing at 650 ·C for 1 hour enhanced the micro-hardness and tensile strength but reduced the yield strength of SLM® processed austenitic stainless steel [38]. M. A. Taha et al investigated the effect of scan speed and post heat treatment on selective laser melting of ultra-high carbon steel. Annealing heat treatment of heating and holding for a duration of one hour was carried out on the SLM® processed ultra-high carbon steel at different conditions of temperature namely

700 ·C, 750 ·C, 950 ·C. The results indicate that the porosity and cracks were cemented during the post heat treatment [39].

Sudha Cheruvathur et al studied the post-heat treatment of additive manufacturing of 17-4 PH stainless steel. Post heat treatment was conducted at 650 ·C and 1050 ·C for a duration of 1 hour. The microstructure was found to be homogenized after the post-processing heat treatment. The dendritic microstructure was found to be dissolved completely. The post-processing heat treatment yielded a phase composition of 90% martensite and 10% retained austenite [40]. T. Niendorf and F. Brenne processed high manganese steel by SLM® for the first time. They found that no post heat treatment was necessary for improving the mechanical properties [41]. Bo Song et al investigated the microstructural evolution, effect of residual stresses and tensile behavior of vacuum heat-treated iron parts manufactured by SLM®. Vacuum annealing imparted grain refinement and improved the ultimate tensile strength [42].

Having delineated the effect of heat treatment in the additive manufacturing process, the motivation for investigating the pitting characteristics in the LENS® of stainless steel 316 L arises. Pitting is characterized by several methods like potentiodynamic polarization corrosion tests, current transients, laser profilometry, scanning electron microscopy post-immersion tests etc. R. K. Gupta et al employed laser profilometry and current transients to characterize and study the metastable pitting characteristics in aluminum alloys [43]. R. F. Patella et al employed 3D laser profilometry to study the pits in cavitation of copper, stainless and aluminum. They promulgated a characterization of pits by eliminating the positive points. In the proposed methodology, the maximum depth of valleys is considered as the measurement of pitting [44]. To the authors' best knowledge, a literature gap exists in the evaluation of the effect of heat treatment in the LENS® of stainless steel 316 L in the pitting corrosion characteristics in the chloride environment. The effect of stress-relieving heat treatment was scarcely investigated from the point of view of different processing conditions in the pragmatic chloride environment for the prolonged duration. The current research endeavors to cement the lucidly defined literature gap.

1.9 Thermal behavior in the LENS® process

The thermal characteristics during the process determine the mechanical properties like strength, resilience, toughness, wear resistance etc. Also, the thermal history determines the phases of evolution and the recrystallization phenomenon as well. The complicated thermal history during the LENS® process is due to the number of heating-reheating cycles. The powders when deposited are laser heated instantly to form a molten pool, which undergoes rapid quenching. The rate of quenching decreases with subsequent layers of deposition [19]. J. E Smugeresky et al found the correlation effect between the surface mechanical properties of finish and surface hardness to the thermal processing conditions [10]. They found that the best surface finish was obtained in 316 L stainless steel at a laser processing power of 325 W with an average flow rate and it is found to be independent of traverse speed. They also confounded the fact that best hardness values were obtained when powder size is very fine and at the minimal possible laser power [10]. In the same 316 L stainless steel, high-density fine microstructure metallic parts were obtained when the powders were coaxially fed. The microstructure was found to coarsen when the deposition layer thickness increases. Microstructure homogeneity was found to be maintained when the laser power and laser traverse speed is controlled to maintain nearly constant melt pool size. Cooling rate between 10^3 and 10^4 K/s yields an optimum micro-hardness of 300 HV (3.18 GPa) [18]. In the light of understanding the thermal behavior phenomena in LENS® process, it is important to note that the temperature gradient during the process of deposition determines the buildup temperature and accumulation of residual stresses in the component. Liang Wang et al investigated the residual stress development in LENS® of AISI 410 stainless steel plates. Their results recommend the employment of high laser traverse speed to reduce the magnitude of residual stress [14].

1.10 Microstructural evolution in the LENS® process

The virtue of layer by layer deposition and non-equilibrium solidification associated with the LENS® process led to the development of various complex alloys. This would have been difficult to fabricate in other conventional processes. Felix A. Espana et al developed CoCrMo alloy bio-implants, which has improved load bearing capabilities. It was designed with 70% porosity to substitute the conventional bio-implants with the lightweight load bearing capabilities. The design was made to mimic natural bone. This bio-implant was found to minimize the wear-induced osteolysis. This research stands as a standing proof vouching for the fact LENS® fabrication does not alter the material properties of biocompatible alloys [45]. Further Vamsi Krishna Balla et al developed porous tantalum structures for bone implants with Young's modulus varying between 1.5 and 20 GPa with pore volume varying between 27% to 55% [46]. LENS® of Ti implants with porosity volume between 17-58% showed the mechanical strength of 24-463 MPa and low Young's modulus of 2.6-44GPa [47]. Porous NiTi shape memory alloy biomedical stents were fabricated in LENS® process. NiTi samples with 12-36% porosity showed high compressive strength and recoverable strain (shape memory effect) and low Young's modulus between 2 and 18 GPa. LENS® processing of NiTi showed an increased amount of cubic B2 phase and increased reverse transformation temperatures when compared to conventional processes [48]. Nickel aluminide inter-metallics (Ni3Al and NiAl) fabricated using LENS® process exhibits high solidification and sub-solidus cracking susceptibility and crack-free deposits [49]. Similarly, Carbide-Particle-Reinforced Titanium Aluminide-Matrix composites were developed using LENS® process [50]. Cermets like WC-Co was successfully fabricated using LENS® process which is very difficult to fabricate using conventional processes [51].

P. C. Collins developed compositionally graded titanium-vanadium and titanium-molybdenum alloys, compositionally graded yttria-stabilized zirconia coating on stainless steel and compositionally and structurally graded T-TiO2 structures with large compositional variation across the lengths [52, 53] [54]. AISI 4140 Stainless steel was fabricated through LENS® process [19]. In addition, LENS® was used for surface modification of AISI 410 martensitic stainless steel.

At high scan speed and at low laser power, high amount of retained austenite is observed in the microstructure. This results in high strength of austenite [55]. I. Kunce et al employed LENS® process to fabricate a high entropy alloy ZrTiVCrFeNi, which has high hydrogen storage capacity [56]. LENS® has also been successfully and effectively employed to fabricate bulk metallic glass and bulk metallic ceramics [57], when compared to conventional processes like welding, casting etc. This subsequently results in rapid solidification and reheating resulting in non-equilibrium phases like martensite and bainite. Segregation of alloying elements occurs during solidification due to partitioning. The substitutional alloy elements undergo slow diffusion and homogenize during the process of solidification [17]. M. L. Grifith et al found that when the molten pool during LENS® deposition solidifies quickly, it results in high yield strength and high ultimate tensile strength values in the component [17]. This occurs at a low energy density of the laser beam [17]. During the process of solidification in LENS®, columnar growth was observed with varying dendritic arm spacing from the substrate with varying orientation of the dendritic arms based on the laser traverse speed and location of the molten pool. For higher laser speeds, secondary and tertiary arms were not produced. In such high laser speeds, dendritic to cellular structural transition was seen. At high energy densities associated with the laser beam, an effect of surface tension and capillary rise called Marangoni effect is seen which results in the localized high-temperature gradient. During the existence of such a high-temperature gradient, the dendrites tend to coarsen and re-melt [58].

The association of various processing parameters of LENS® plays a significant role in the microstructure evolution. When the laser power is high and it results in high energy density, which results in a relatively uniform temperature gradient. This results in low residual stress and uniform microstructure with cellular structure. During this process, a columnar epitaxial growth is seen which results in the dendritic structure with secondary and tertiary arms that later forms the cellular microstructure. During high laser traverse speeds, the laser energy densities are low and result in dendritic structure devoid of the formation of secondary and tertiary arms resulting in high tensile

strength with low hardness compared to one formed in high energy density. This can be substantiated from the findings of L. Wang et al who propound that the laser power varies linearly with the number of layers for all laser traverse speeds [13].

It is interesting to comprehend the microstructure evolution in LENS® of Ti-6Al-4V, an important aerospace alloy. The microstructure characterization reveals the gradient alpha and the layer-band striations form in layer after the deposition of layer n+3 [59]. This is called Basketweave Widmanstatten alpha which forms in a matrix of retained beta phase in Ti-6Al-4V.

Apart from these phases in Ti-6Al-4V, R. Banerjee et al found the existence of other phase transition in the graded alloy of Ti-Vanadium. The phase transformations include Beta-Widmanstatten alpha, beta to omega and martensitic beta to hexagonal alpha [60].

A precipitation of alpha grain boundary in compositionally graded Ti-8Al-Xv alloy was found during the LENS® deposition process. This is due to the columnar growth of Beta phase and the tendency to obtain near Burger's orientation of the Alpha phase [61]. The kinetics of globularization of Widmanstatten alpha phase is rapid fine/acicular microstructure at sub-transus temperature. Beta annealing and water quenching are found to develop a martensitic-alpha microstructure with a precaution of avoiding distortion. In super-transus temperatures, recrystallization of the columnar beta-grain structure occurs [62]. In titanium-based metal matrix composite like nickel-titanium-carbon metal matrix composite show primary and eutectic titanium carbides with FCC structure of Titanium carbide. These composites show the relatively high hardness of 370 VHN and steady-state friction coefficient of approximately 0.5, which makes it suitable for application in wear resistant applications when compared to other Nickel based alloys [63]. Raj Banerjee et al found that the absence of equilibrium phases and metastable phases in LENS® resulting in high exothermic enthalpy of mixing of elements can play a predominantly determining role in the homogeneous mixing during solidification resulting in the fairly uniform microstructure. This was experimentally proved with a mixture of 25% Nickel and 75% Molybdenum powder in LENS® process [64].

1.11 Application of LENS® in the development of complex alloys and composites

Due to the virtue of layer by layer deposition and non-equilibrium solidification associated with the LENS® process, various complex alloys have been developed using LENS® process which otherwise would have been difficult to fabricate in other conventional processes. Felix A. Espana et al developed CoCrMo alloy bio-implants, which has improved load bearing capabilities. It was designed with 70% porosity to substitute the conventional bio-implants with the lightweight load bearing capabilities. The design was made to mimic natural bone. This bio-implant was found to minimize the wear-induced osteolysis. This research stands as a standing proof vouching for the fact LENS® fabrication does not alter the material properties of biocompatible alloys [45]. Further Vamsi Krishna Balla et al developed porous tantalum structures for bone implants with Young's modulus varying between 1.5 and 20 GPa with pore volume varying between 27% to 55% [46]. LENS® of Ti implants with porosity volume between 17-58% showed the mechanical strength of 24-463 MPa and low Young's modulus of 2.6-44GPa [47]. Porous NiTi shape memory alloy biomedical stents were fabricated in LENS® process. NiTi samples with 12-36% porosity showed high compressive strength and recoverable strain (shape memory effect) and low Young's modulus between 2 and 18 GPa. LENS® processing of NiTi showed an increased amount of cubic B2 phase and increased reverse transformation temperatures when compared to conventional processes [48]. Nickel aluminide inter-metallics (Ni3Al and NiAl) fabricated using LENS® process exhibits high solidification and sub-solidus cracking susceptibility and crack-free deposits [49]. Similarly, Carbide-Particle-Reinforced Titanium Aluminide-Matrix composites were developed using LENS® process [50]. Cermets like WC-Co was successfully fabricated using LENS® process which is very difficult to fabricate using conventional processes [51].

P.C. Collins developed compositionally graded titanium-vanadium and titanium-molybdenum alloys, compositionally graded yttria-stabilized zirconia coating on stainless steel and compositionally and structurally graded structures with large compositional variation across the

lengths [52, 53] [54]. AISI 4140 Stainless steel was fabricated through LENS® process [19]. In addition, LENS® was used for surface modification of AISI 410 martensitic stainless steel. At high scan speed and at low laser power, high amount of retained austenite is observed in the microstructure. This results in high strength of austenite [55]. I. Kunce et al employed LENS® process to fabricate a high entropy alloy ZrTiVCrFeNi, which has high hydrogen storage capacity [56]. LENS® has also been successfully and effectively employed to fabricate bulk metallic glass and bulk metallic ceramics [57].

1.12 Objectives

The following are the objectives of the current research.

i) To investigate the effect of laser processing parameters such as laser power, laser scan speed, and powder deposition rate on the corrosion and wear properties of stainless steel 316 L additively manufactured using LENS® process.

ii) To compare the wear and corrosion properties of the stainless steel 316 L additively manufactured using LENS® process with the wrought stainless steel 316 L.

iii) To evaluate the effect of stress-relieving heat treatment on the pitting corrosion characteristics of stainless steel 316 L.

CHAPTER II

MATERIALS AND METHODS

This chapter presents the materials, systems, instruments, and the methodologies employed in the research.

2.1 Research approach

The research started by processing simple cuboid samples of dimension 12 mm × 12 mm × 6 mm under four different levels of laser power as shown in Table 2. The corrosion potential was evaluated as described in the following sections. At a constant laser power of 350 W that resulted the highest corrosion potential, further samples of the same dimension were processed at varying levels of laser scan speed as shown in the Table 2. In order to investigate the effect of powder deposition rate on the corrosion and wear properties, samples were processed at four different levels of powder deposition rate at constant laser power and laser scan speed.

Corrosion analysis started by investigating the potentiodynamic polarization corrosion characteristics of wrought stainless steel 316 L under different conditions of heat treatment and shot blasting. The potentiodynamic polarization corrosion potential was evaluated. This was followed by the surface roughness and material density evaluation. The XY plane (Build

plane designated as per ISO/ASTM 52900:2015) of the samples were polished for 15 minutes using 400 grit silicon carbide paper and again by 800 grit silicon carbide paper for another 15 minutes in a mechanical grinder polisher operating at 300 rpm. This eliminates the effect of surface roughness. The potentiodynamic polarization corrosion was conducted on the polished XY planes of the samples pertaining to varying conditions of laser scan speed and powder deposition rate (S.No.4-7). This test was reprised to investigate and validate the trend obtained previously. The samples were then bisected and polished for scanning electron microscopy. This was followed by heat treatment of one set of the bisected samples. The bisected halves were lacquered before being placed in the immersion corrosion environment (10 % dilute HCl) for 120 hours.

The research approach is to evaluate the effect of processing conditions on the microstructural features and subsequently evaluating the effect of the obtained microstructural features on the properties. This is illustrated in Fig. 2.1. In this research, the effect of processing conditions namely laser power, laser scan speed, powder deposition, the effect of heat treatment on microstructural evolution, microstructural features of wear, pitting corrosion properties are evaluated. The consequence of the microstructural features on the macroscopic properties is analyzed and reported. The macroscopic properties include corrosion potential, wear weight loss, pitting corrosion rate, corrosion penetration rate in pitting and maximum pitting depth.

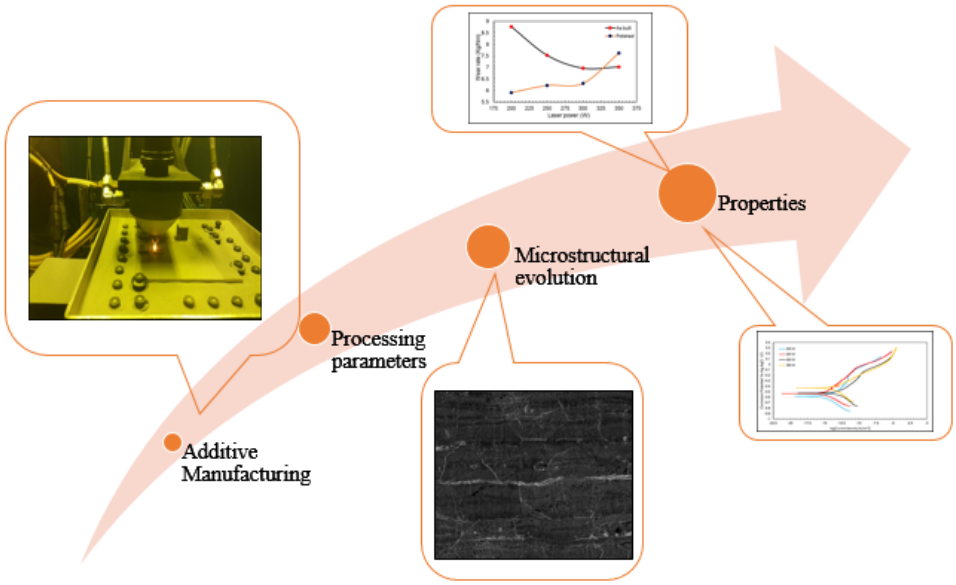

Fig. 2.1 Schematic of the research approach

2.2 Optomec LENS® additive manufacturing system

Stainless steel 316 L powder (Praxair Surface Technologies) of particle size range +45 µm/-150 µm was used for the experimentation in the Optomec (Albuquerque, New Mexico), LENS® 450 XL machine equipped with 400 W IPG Fiber laser system. The system is shown in Fig. 2.2 and Fig. 2.3. Simple cuboids of dimension 12 mm × 12 mm × 6 mm (as shown in Fig. 2.4 and Fig. 2.5) were printed using different processing conditions as shown in Table 2.

The laser energy density per unit volume is given in equation (2)

$$E = \frac{P}{Vs.t.d} \tag{2}$$

Where “E” is the volume laser energy density, “P” is the laser power, “Vs” is the laser scan speed, “t” is the layer thickness and “d” is the hatch spacing. This equation is obtained from [65].

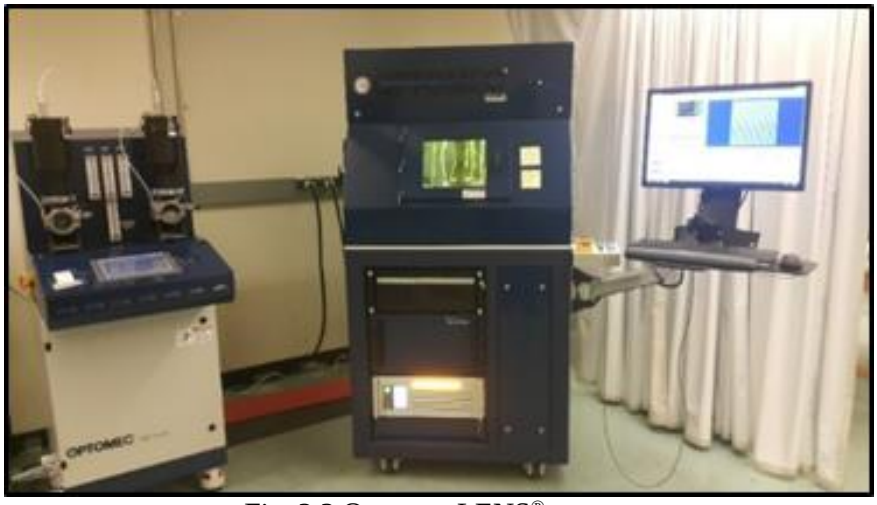

Fig. 2.2 Optomec LENS® system

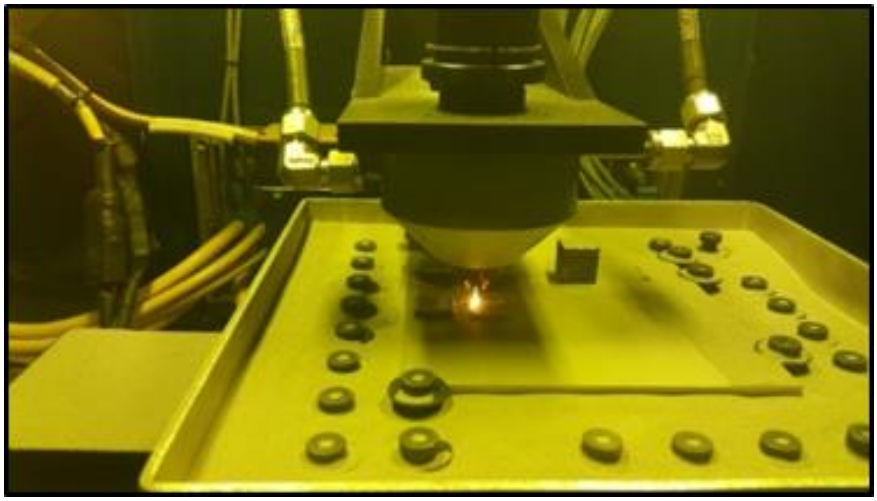
Fig. 2.3 Deposition system

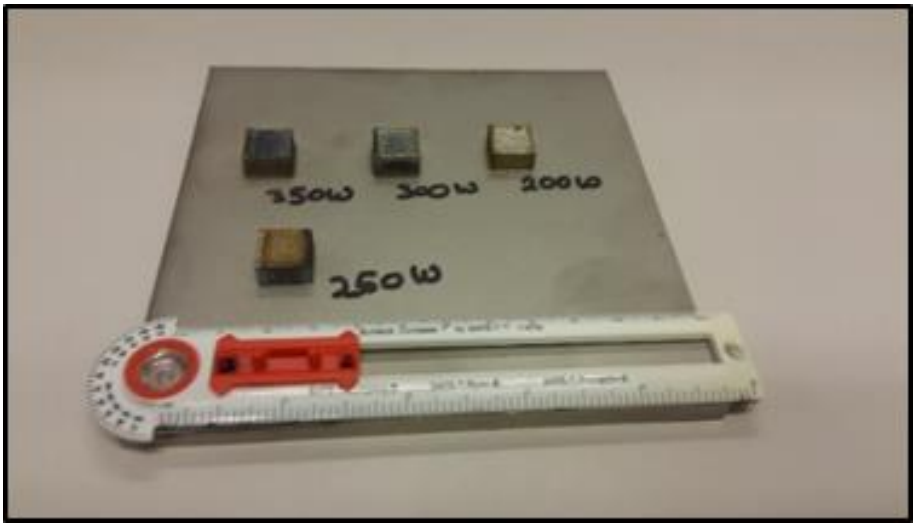

Fig. 2.4 Additively manufactured stainless steel 316 L

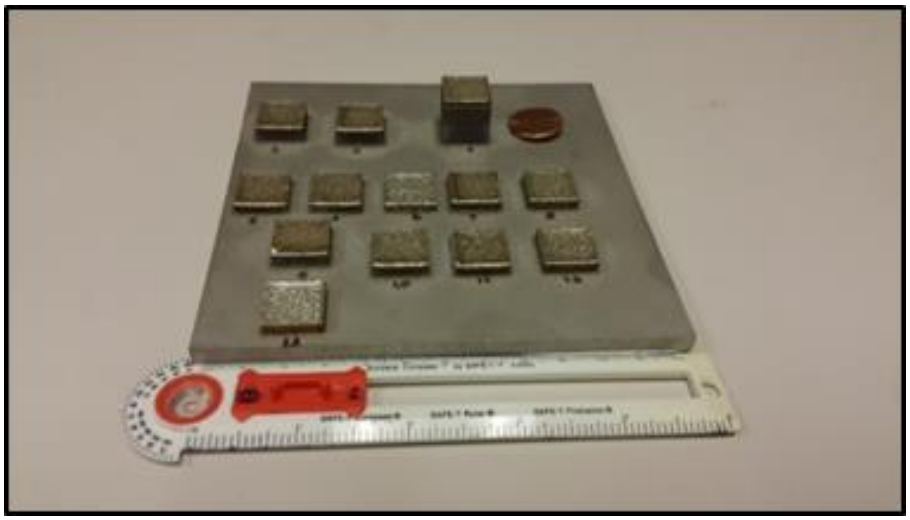
Fig. 2.5 Additively manufactured stainless steel 316 L

2.3 Processing conditions

Table 2: Processing conditions of LENS® of stainless steel 316 L

S.No.	Laser Power (W)	Laser scanning speed (inch/min)	Layer thickness (inch)	Hatch spacing (inch)	Powder feed rate (rpm)	Oxygen level (ppm)	Laser energy density per unit volume (J/mm^3)
1.	200	20	0.01	0.015	6	20-100	248.996
2.	250	20	0.01	0.015	6	20-100	311.246
3.	300	20	0.01	0.015	6	20-100	373.495
4.	350	20	0.01	0.015	6	20-100	435.744
5.	350	15	0.01	0.015	6	20-100	569.555
6.	350	25	0.01	0.015	6	20-100	341.744
7.	350	30	0.01	0.015	6	20-100	284.777
8.	350	20	0.01	0.015	4	20-100	435.744
9.	350	20	0.01	0.015	8	20-100	435.744
10.	350	20	0.01	0.015	10	20-100	435.744

2.4 Profilometer and profilometry

The surface roughness and depth of wear track of the as-built profiles of the XY plane (Build planes designated as per ISO/ASTM 52900:2015) were measured using 3D optical profilometer (Nanovea, Irvine, CA) and Nanovea professional 3D software.

2.5 Micro-hardness evaluation

Micro-hardness hardness mapping of XY plane (Build planes designated as per ISO/ASTM 52900:2015) was evaluated in Vicker's hardness tester (Clark's instrument). The system was operated with a load of 300 g and a dwell time of 15 seconds.

2.6 Ball on disk tribometer and tribometry

The XY plane of the samples was analyzed for dry wear characteristics in a Ball on disc tribometer (Nanovea, Irvine, CA) with the application of a normal load of 10 N at sliding velocity of 150 rpm. ASTM G99 stainless steel ball (Nanovea, Irvine, CA) of 3 mm diameter was employed as the counter body to create a wear track of 4 mm diameter. The weight loss of the samples was measured after a duration of 3600 seconds under dry sliding conditions.

The weight loss of the wrought material was also evaluated on a wrought hot rolled stainless steel 316 L sample purchased from McMaster-Carr Supply Company. The densities of the printed samples were calculated using Archimedes principle.

2.7 Potentiodynamic polarization corrosion test

Potentiodynamic polarization corrosion tests were performed for the printed samples in the as-built condition of the XY plane in a glass-flat electrochemical cell containing 3.5 wt % NaCl solution. In this potentiodynamic polarization corrosion test, the printed samples were used as the working electrode in each run, 3.5 M Ag,AgCl/KCl is used as the reference electrode and platinum counter electrode was employed. The counter electrode is connected to the power output of the computer interface VersaSTAT 4 module, which employs a commercial software VersaStudio as a user interface. VersaSTAT 4 uses PARstat2263 Revision 2263 potentiostat as the polarization corrosion test is carried out in potentiostatic mode. The corrosion current is measured through the working electrode in a work exposure area of one cm^2. In the first step, an open circuit test was conducted for 1800 seconds with 1 second per point at zero drift rate. In the second step, the tafel corrosion test was conducted with a step height of 1 milliVolt and step time of 1 second from an initial potential of -0.25 V to a final potential of + 0.75 V versus the open circuit. The discussed tafel test is a corrosion technique that utilizes a single voltage scan or ramp program from an initial potential to a final potential versus open circuit at E_{corr}.

2.8 Sample preparation and etching for SEM

The samples were bisected across the centerline across the XY plane using 7'' diamond saw cutter at 350 rpm. The cross sections were mechanically polished in a wheel grinder polisher at 300 rpm for minutes in 600 grit SiC paper (Silicon Carbide), 15 minutes in 800 grit SiC paper, 20 minutes in 1200 grit paper at the same rpm. The samples were micro-polished with alumina slurry of 0.3 µm particle size for 5 minutes to obtain a very good finish for vivid results in the scanning electron microscopy. The cross-section surfaces were etched for 8 seconds using an Adler's etchant solution. The Alder's etchant contains 60% - 70% hydrochloric acid, 15% of anhydrous ferric chloride and 3% cupric ammonium chloride.

2.9 Stress relieving heat treatment

One set of the cross-section samples were heat treated by soaking at a temperature of 380 ·C for 30 minutes. The purpose of the heat treatment is for stress relieving. The scales formed post-heat treatment is polished and removed. Stress relieving heat treatment is done by heating the samples in an induction furnace at 380 ·C and holding for a duration of 30 minutes to relieve the internal residual stresses as explained previously. This is a proposed ad promulgated by Hao Yun-Wei et al [66]. The heat treatment temperature of stainless steel 316 L is limited by the susceptibility to sensitization phenomenon at higher temperatures.

2.10 Immersion corrosion test

Immersion corrosion tests were conducted by immersing the as-built samples and heat-treated samples in an acid mixture of 10% HCl solution for 120 hours at room temperature while measuring the weight loss of the sample in a balance of 0.1 mg accuracy. The samples were lacquered to expose only a constant area of 107.17 mm^2. The lacquering of edges prevent crevice corrosion and facilitate corrosion only by pitting during the immersion corrosion.

2.11 Scanning electron microscopy

Scanning Electron Microscopy characterization was performed on the cross sections of the samples using FEI Quanta 600F FE ESEM (Field Emission Environmental Scanning Electron Microscope) instrument. All the SEM micrographs were captured in high vacuum mode using Secondary Electron Detector – ETD (Everhart-Thornley Detector).

2.12 X-ray diffraction

Analysis of phases by X-ray diffraction was conducted on the cross-sections using the X-ray diffractometer (BRUKER AXS Inc, Madison, WI) operating with Cu-Kα radiation ($\lambda = 1.54178$ A°). The diffraction angle 2θ varied between 30^{o} and 80^{o} degrees.

CHAPTER III

MICROSTRUCTURE OF STAINLESS STEEL 316 L ADDITIVELY MANUFACTURED USING LENS®

This chapter presents the evolution of the microstructure during laser engineered net shaping (LENS®) of stainless steel 316 L. The microstructure evolution of stainless steel samples is studied under different conditions of LENS® processing.

The microstructure of the XZ plane of the samples corresponding to variation in laser power and laser scan speed was studied. Dendritic grain morphology was observed in the stainless steel 316 L additively manufactured in the LENS® process (Fig. 3.1 - Fig. 3.14). The grain size as observed in the microstructure in the LENS® additive manufacturing process was smaller when compared to the wrought stainless steel 316 L as seen from the figures Fig. 1.1 and Fig. 1.2.

The microstructure of the stainless steel 316 L additively manufactured in the LENS® process obtained is similar to the literature [7, 27-29, 67]. The columnar grains grow parallel to build direction <001> - towards temperature gradient (ΔT). Melt pool previously solidified was partly re-melted during the deposition of successive layers showing the difference in grain morphology at the layer boundaries. Melt pool overlapping in all directions indicates that the laser energy density was ample for densification to form a solid body [8].

Melt pool previously solidified was partly re-melted during the deposition of successive layers showing difference in grain morphology at the layer boundaries. In the layer boundaries, the dendritic arm spacing was found to be smaller than the inner regions of a layer. At vicinity to substrate, cooling rate being high results in smaller mean grain size. At the top layers microstructure was observed to be irregular and approaching near equiaxed morphology. At the bottom layers, the dendrites were fine columnar and while approaching the top layers, coarse columnar dendrites were seen.

As laser power increases, columnar dendritic to equiaxed transition was lucidly observed in the layers and the boundaries showed regions of columnar dendrites and equiaxed at higher power levels whereas only columnar dendrites were observed at lower power levels. In addition, columnar dendrites became coarser as laser power increased. As the laser power increased, the cooling rate decreased due to the high temperature gradient and high energy density, concomitantly the dendritic arm spacing increased with decrease in cooling rate. This resulted in an increase of dendritic arm spacing with increase in laser power.

The dendrites were observed to be regular at lower scan speeds. At higher scan speeds, the dendrites were observed to be irregular. The network of dendritic arms were not found in the higher levels of laser scan speed as opposed to lower laser scan speed.

The following section shows the SEM micrographs of samples processed at different conditions. The low magnification micrographs marked as “a”, “b”, “c”, “d” represents the respective regions as shown in the high magnification micrographs.

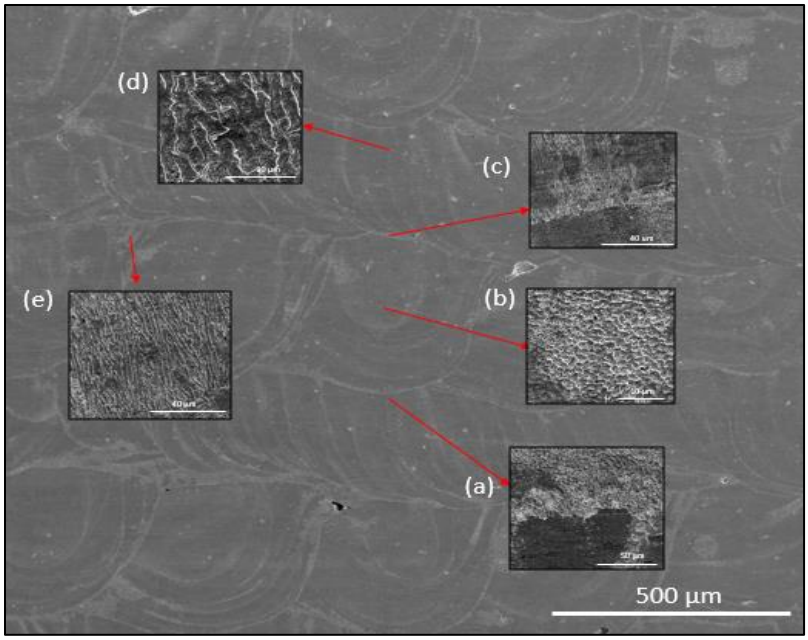

Fig. 3.1 SEM micrograph of the sample (Laser power: 200 W, Scan speed: 20 in/min, powder deposition rate: 6 rpm)

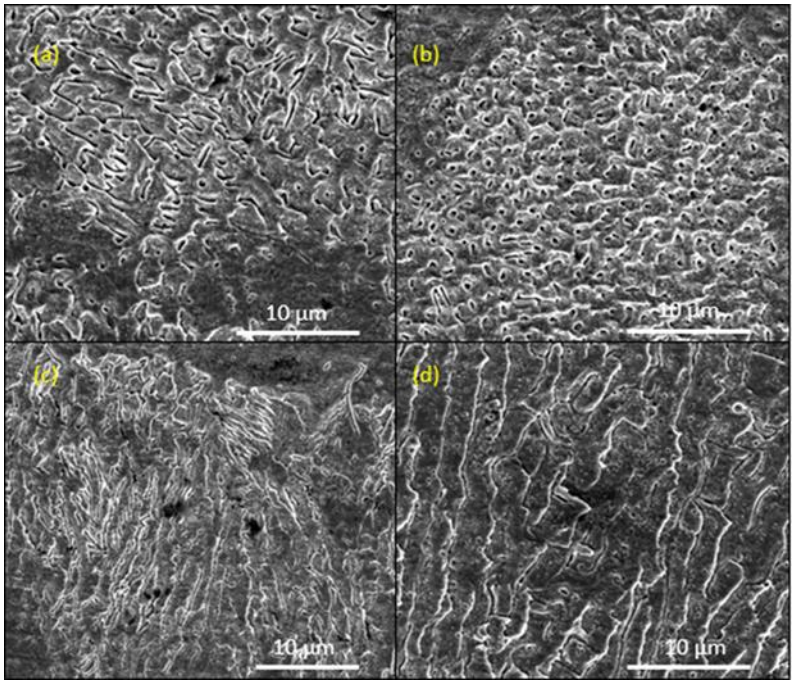

Fig. 3.2 Micrographs of insets of respective regions as shown in Fig.3.1

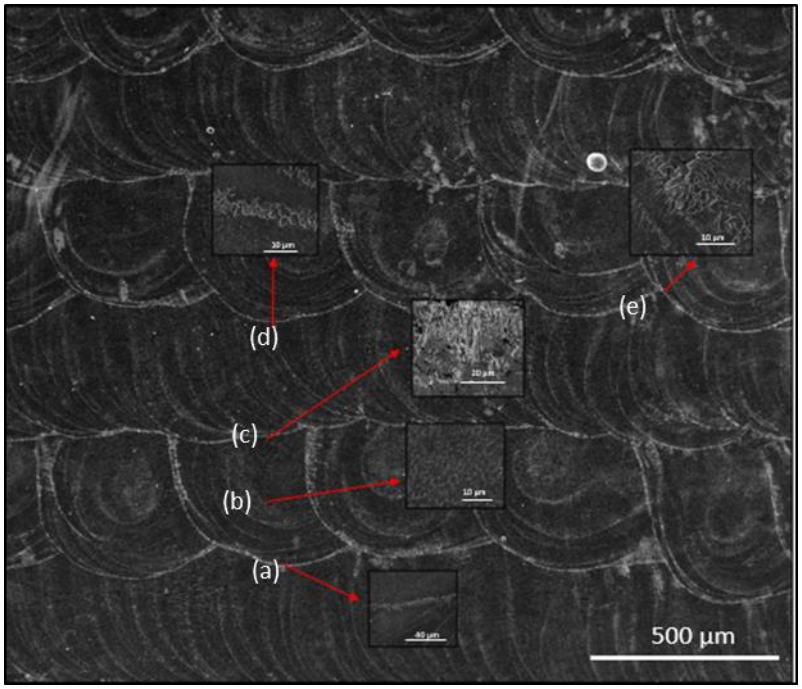

Fig. 3.3 SEM micrograph of the sample (Laser power: 250 W, Scan speed: 20 in/min, powder deposition rate: 6 rpm)

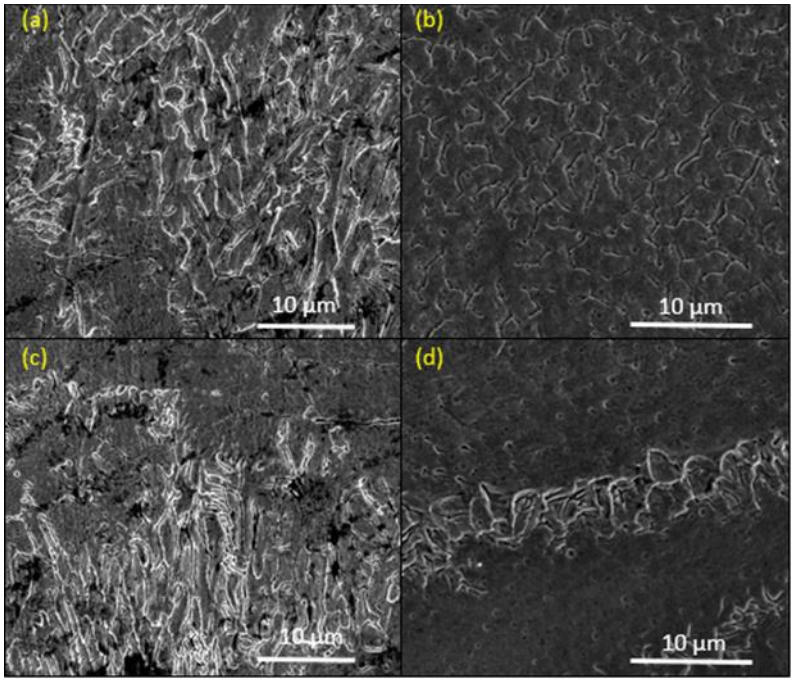

Fig. 3.4 Micrographs of insets of respective regions as shown in Fig.3.3

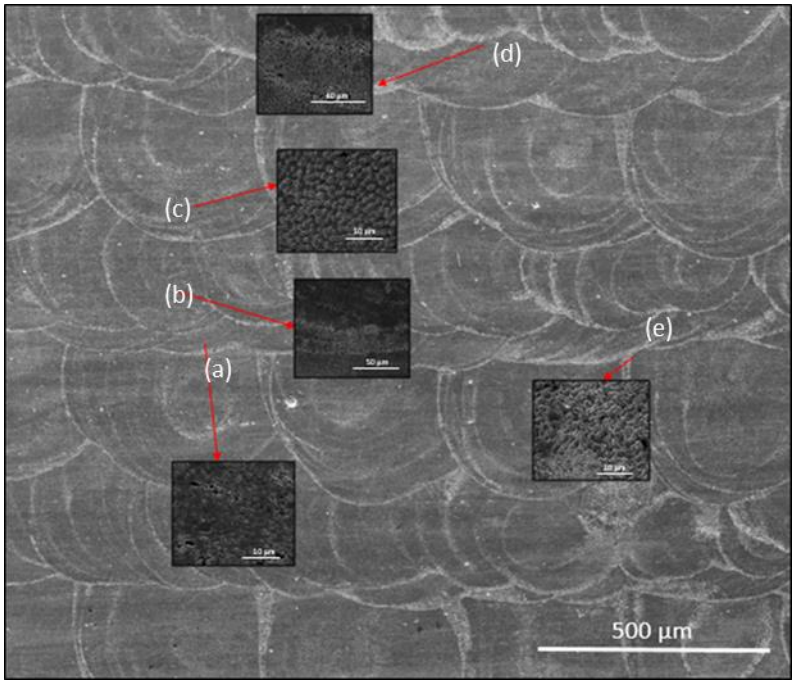

Fig. 3.5 SEM micrograph of the sample (Laser power: 300 W, Scan speed: 20 in/min, powder deposition rate: 6 rpm)

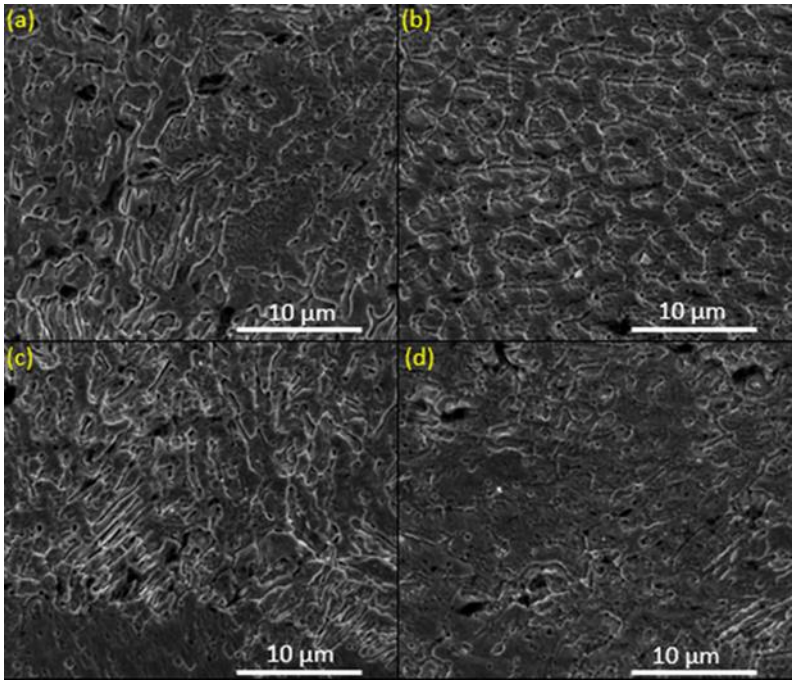

Fig. 3.6 Micrographs of insets of respective regions as shown in Fig. 3.5

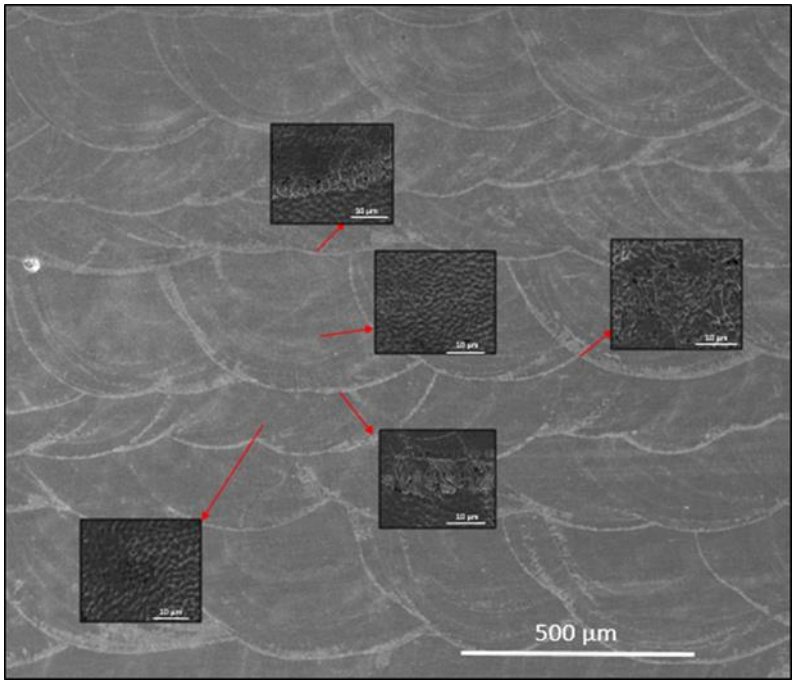

Fig. 3.7 SEM micrograph of the sample (Laser power: 350 W, Scan speed: 20 in/min, powder deposition rate: 6 rpm)

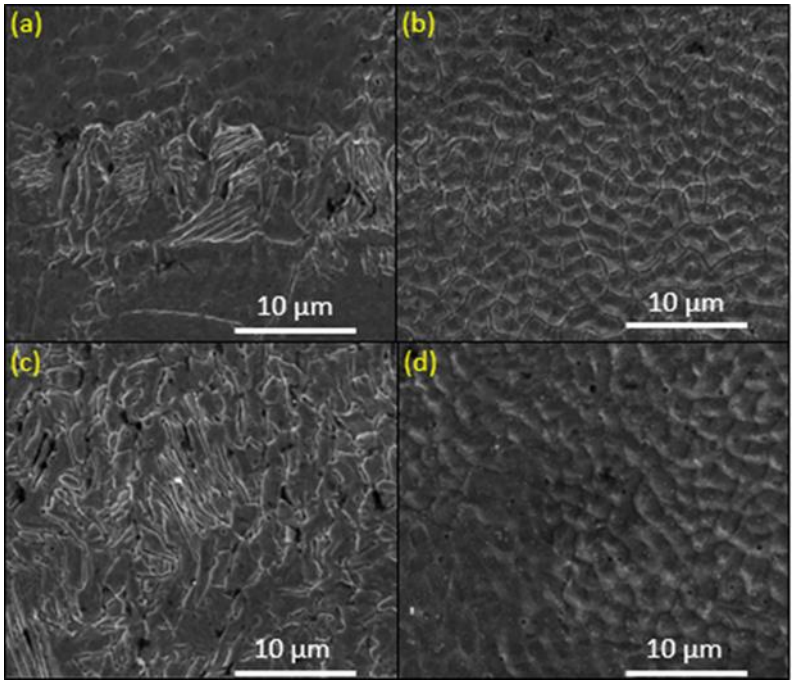

Fig. 3.8 Micrographs of insets of respective regions as shown in Fig. 3.7

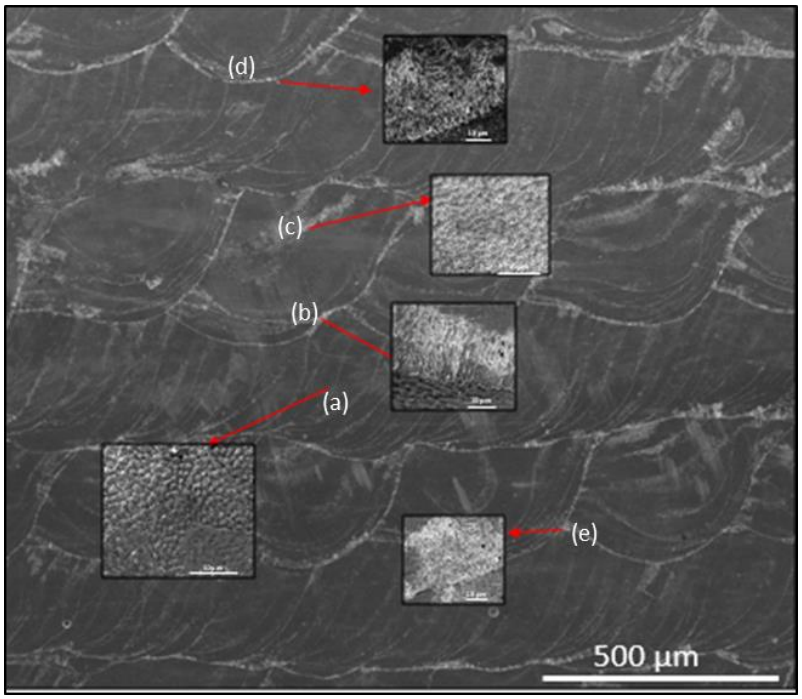

Fig. 3.9 SEM micrograph of the sample (Laser power: 350 W, Scan speed: 15 in/min, powder deposition rate: 6 rpm)

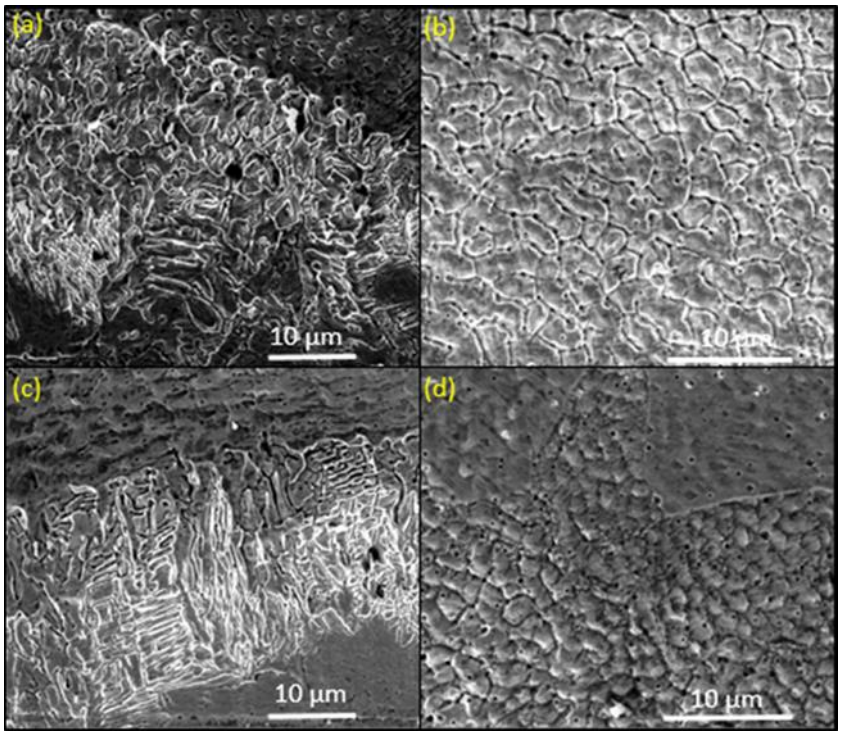

Fig. 3.10 Micrographs of insets of respective regions as shown in Fig. 3.9

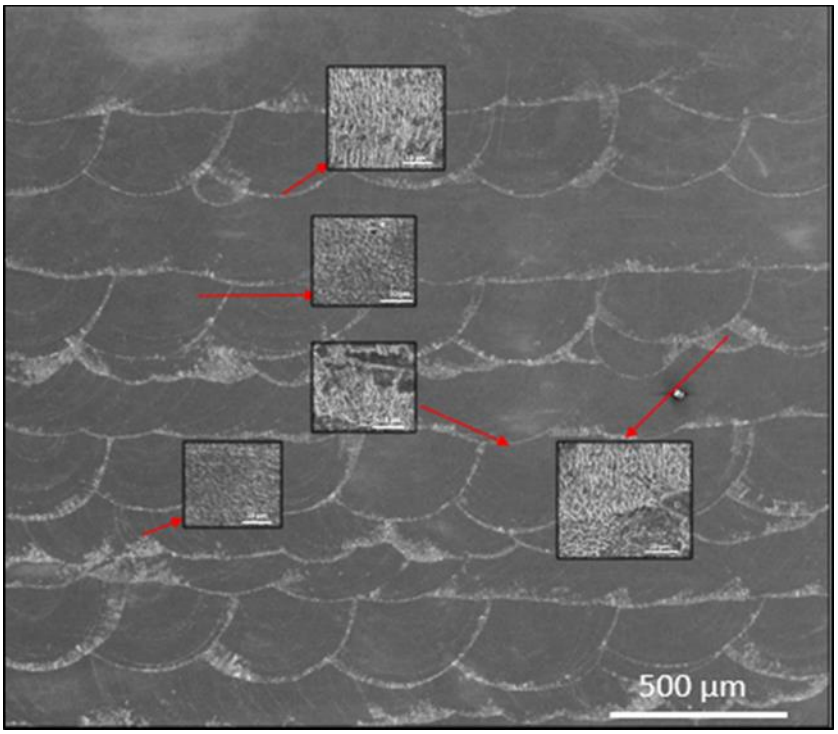

Fig. 3.11 SEM micrograph of the sample (Laser power: 350 W, Scan speed: 25 in/min, powder deposition rate: 6 rpm)

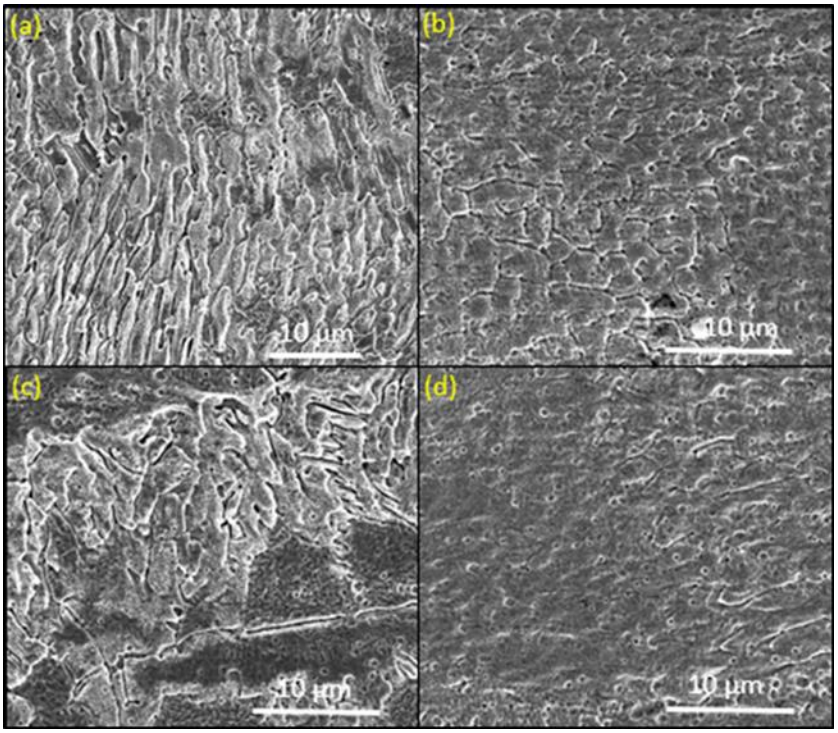

Fig. 3.12 Micrographs of insets of respective regions as shown in Fig. 3.11

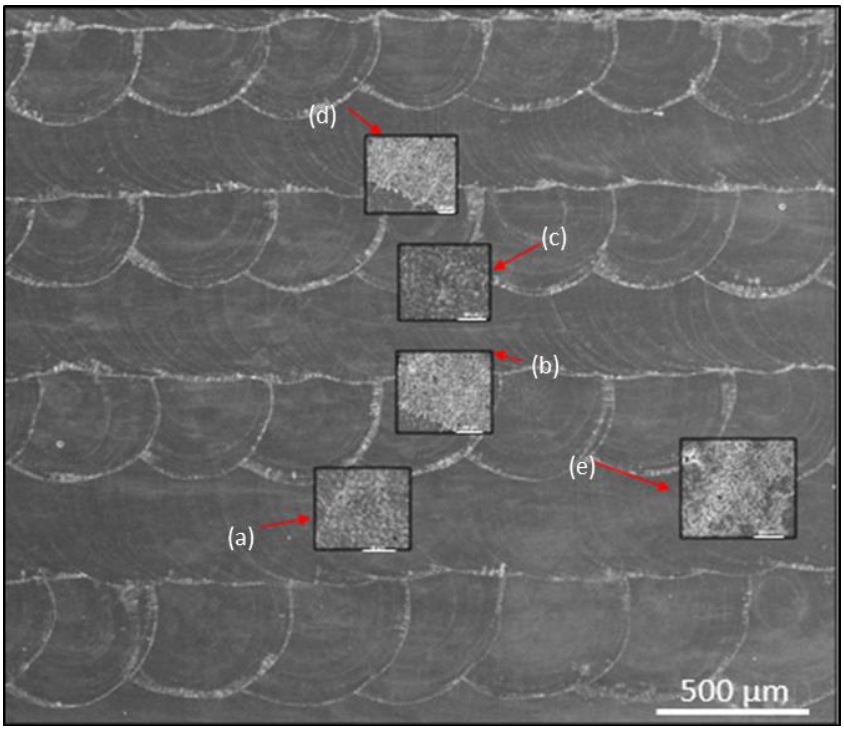

Fig. 3.13 SEM micrograph of the sample (Laser power: 350 W, Scan speed: 30 in/min, powder deposition rate: 6 rpm)

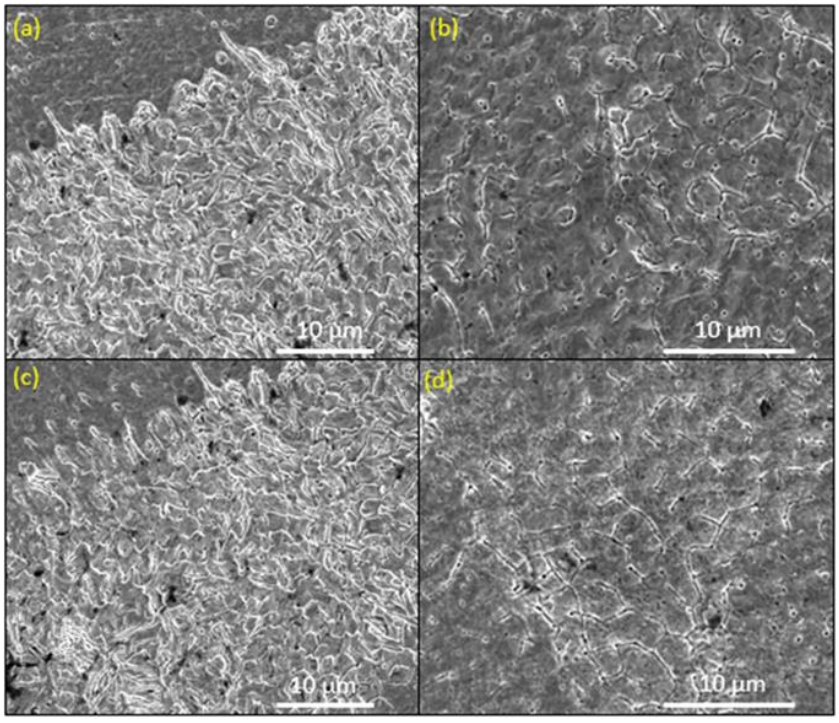

Fig. 3.14 Micrographs of insets of respective regions as shown in Fig. 3.13

CHAPTER IV

WEAR ANALYSIS

The current chapter discusses the wear characteristics of wrought stainless steel 316 L. The effect of LENS® parameters such as laser power, laser scan speed, and powder deposition rate on the wear properties are evaluated.

4.1 Wear characteristics of wrought stainless steel 316 L

We started by investigating the wear characteristics of wrought stainless steel 316 L. The wear characteristics of the wrought stainless steel 316 L sample is also discussed in the further sections comparing with the LENS® processed samples manufactured at different levels of laser power and laser scanning speed. The wear track of wrought stainless steel 316 L is shown in Fig. 4.1 and Fig. 4.2. The results are shown in Table 3. As an outcome of surface roughness, the worn debris is trapped between the asperities and compacted due to the subsequent sliding action of the stainless steel slider ball. This was also observed by Junhu Meng et al [68]. This type of oxidative wear is found to be the reason for mild wear in stainless steel [69]. Oxidation is a result of frictional heating due to the dry sliding action [70]. Oxidative wear is favored when dry sliding conditions prevail, and an oxide film of sufficient thickness is formed under prolonged duration under the condition that the material has sufficient integrity to support the oxide film [71]. As discussed earlier, the microstructural difference between the additive manufacturing stainless steel 316 L and the wrought stainless steel 316 L results in the increased wear resistance of

stainless steel 316 L additively manufactured in the LENS® process. This is because the stainless steel 316 L additively manufactured in the LENS® process exude dendritic grain morphology with smaller grains compared to coarse equiaxed grains in wrought stainless steel 316 L that accounts for increased micro-hardness of stainless steel 316 L.

Table.3: Results of wear analysis of wrought stainless steel 316 L

S.No.	Parameter	Value
1.	Weight Loss (mg)	5.1
2.	Coefficient of friction	0.72
3.	Hardness - LENS® sample	205-240 Hv
4.	Hardness –wrought sample	188.85 Hv

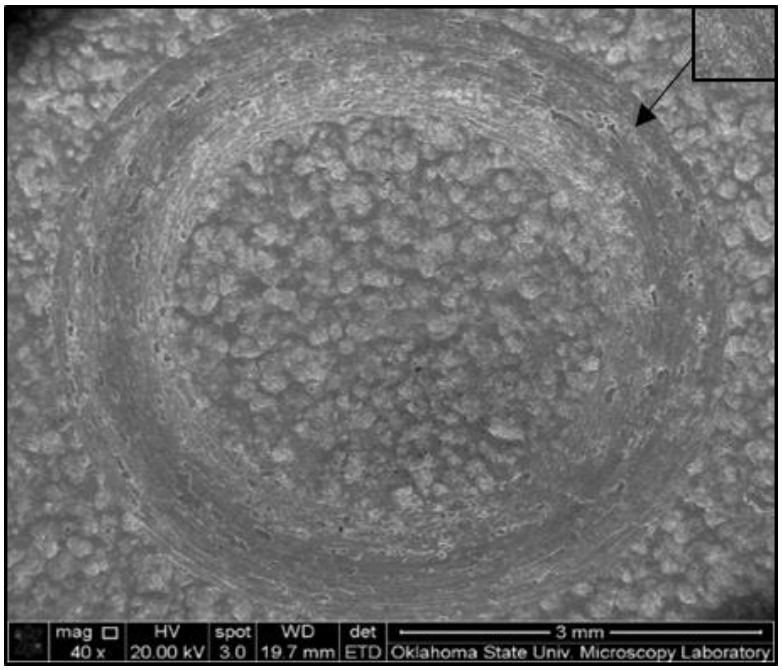

Fig. 4.1 SEM of wear track of wrought stainless steel 316 L

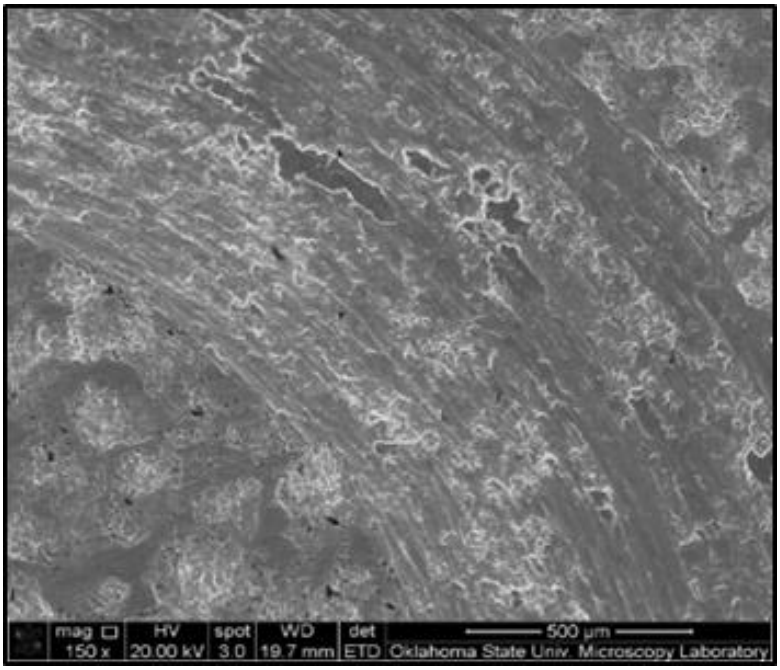

Fig. 4.2 SEM of inset of wear track shown in Fig.4.1

4.2 Effect of laser power

This research work is an endeavor of a modest contribution to the ongoing research discussions on substantiation of the wear characterization and mechanism of stainless steel 316 L material against ASTM G99 stainless steel ball slider in addition to the investigation of the effect of LENS® parameters on the same. A dichotomous relationship of weight loss with laser power was observed that extrapolates the mechanism of wear in additively manufactured stainless steel 316 L during LENS® process. The weight loss decreases with laser power in the as-built XY plane surface and vice versa in the case of the polished XY plane surface eliminating the influence of surface roughness. This phenomenon is eventually explained in the following sections. The wear occurs by the formation and detachment of tribo-oxide layer. Compressive stresses result due to the sliding action. This results in the plastic deformation of the material in the wear track. The resultant is held loosely or compacted to the surface of the material. Frictional heating of the deformed material is the reason for the oxidization and subsequent formation of tribo-oxide layer. This is brittle in nature and subjected to crack propagation resulting in material fracture or delamination. Owing to surface

roughness and powder densification, the worn debris is trapped between the asperities and compacted due to the subsequent sliding action of the stainless steel slider ball.

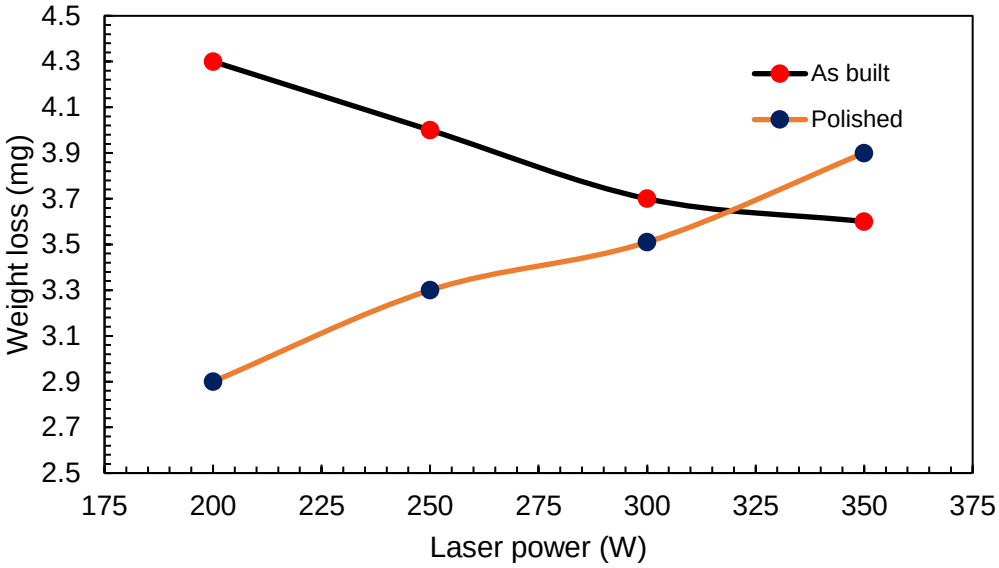

Fig. 4.3 Weight loss measured after 60 minutes

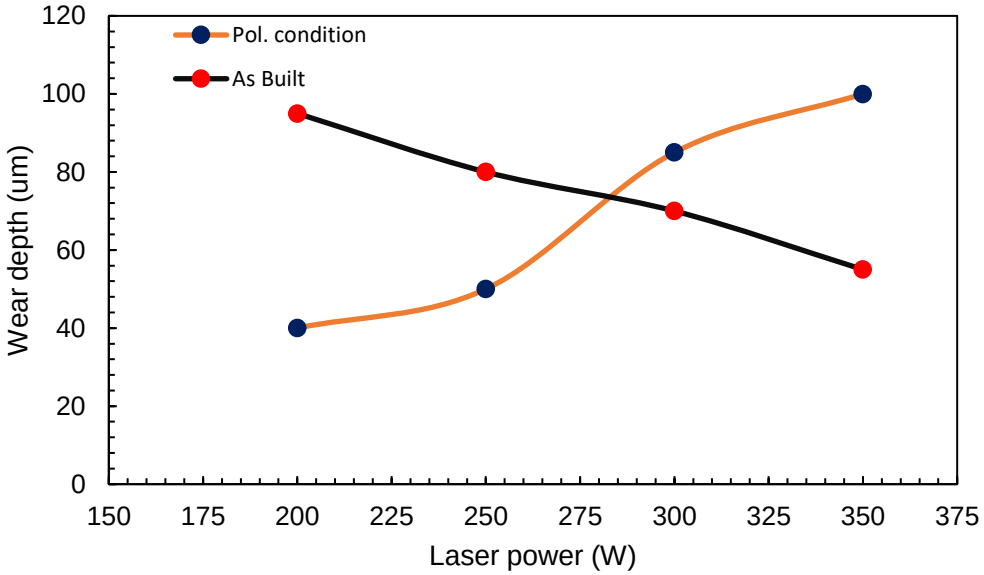

Fig. 4.4 Wear depth measured from profilometry

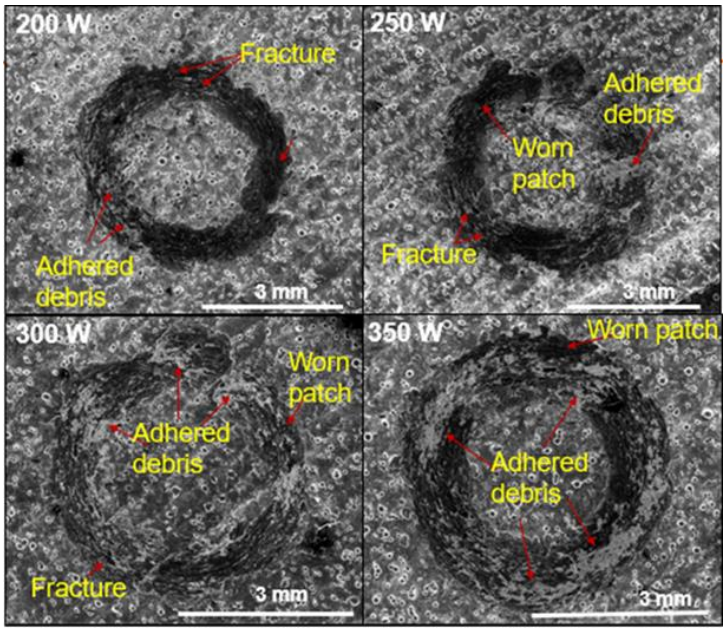

Fig. 4.5 SEM of as-built samples processed at different levels of laser power

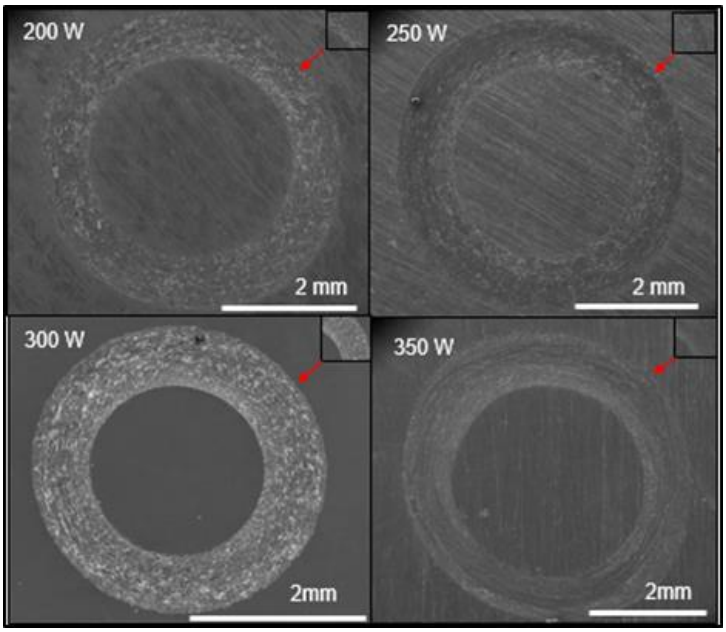

Fig. 4.6 SEM of samples processed at different levels of laser power showing wear tracks on polished XY plane

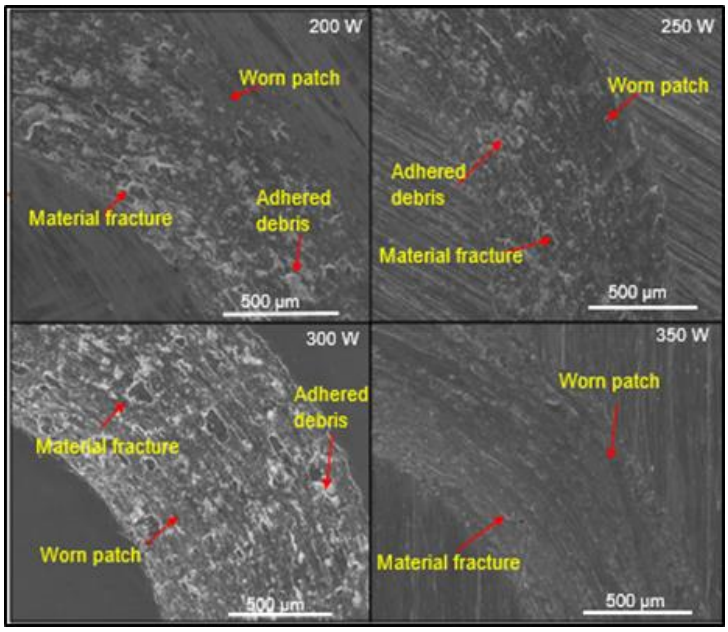

Fig. 4.7 SEM of insets of wear track as shown in Fig. 4.6

As the laser power increases, the laser energy density increases resulting in increased powder densification. This results in increased resistance to plastic deformation subsequently resulting in less delamination and material fracture. As a result, the plastically deformed material patch is not delaminated due to higher powder densification and surface roughness. As a consequence of frictional heating for a duration of 60 minutes, the material on the wear track is oxidized and a tribo-oxide layer is formed. As the test continues, the worn material, which is oxidized is adhered on the wear track. Hence, as the power increases, the weight loss due to wear decreases as shown in Fig. 4.3. This trend is also reinstated and supported by the analysis of the wear track depth as shown in Fig. 4.4.

In the polished surface, when the laser power increases, the adhesion is not favored due to smooth surface. The adhesion of wear debris is not favored by the trapping of surface asperities as in the case of as-built surface where surface roughness (Ra) is a dominating factor. The comparison of surface roughness of the as-built and polished surface is shown in Fig. 4.8. The weight loss and wear depth of both the cases are shown in Fig. 4.3. The adhesion is favored by internal porosities, which inversely depends on the density of the sample. As laser power increases, it results in increase

in laser energy density and powder densification resulting in increase of the density as illustrated in Fig. 4.9. At the lower values of laser power, the powder densification is less. The discussed condition results in more sites for trapping wear debris. Hence, powder densification is the dominating factor in determining the wear characteristics. The scanning electron micrographs of the wear tracks characterized by adherence of wear debris, material fracture, and worn patches reinstate the relationship of laser power as shown in Fig. 4.5 and Fig. 4.6. In both the cases of as-built surface and polished surface, the weight loss due to wear is lesser than that of the wrought stainless steel 316 L implying that the wear performance of the additively manufactured steel can be improved through the LENS® process operating at higher laser energy densities. This is explained due to the higher hardness resulting from the LENS® process.

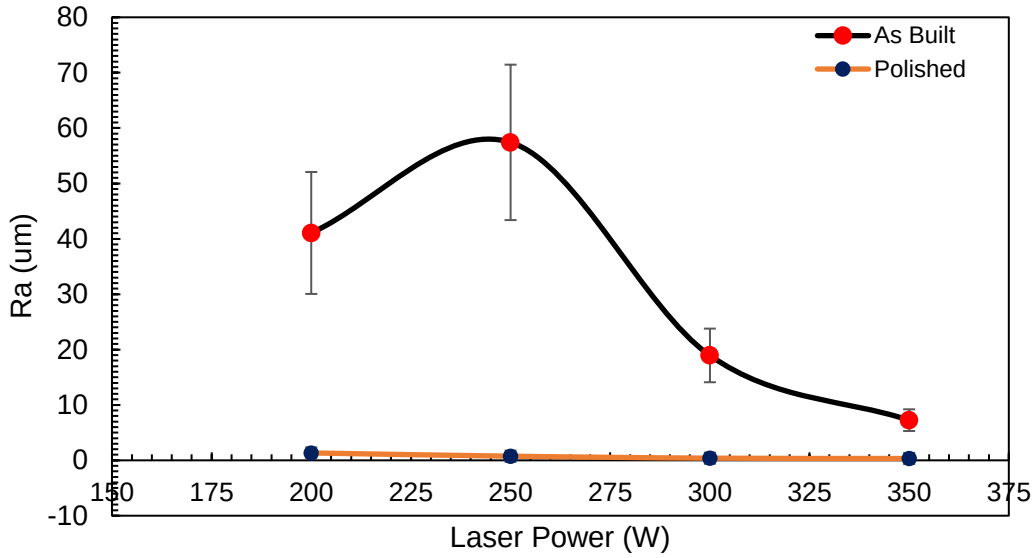

Fig. 4.8 Variation of surface roughness with laser power

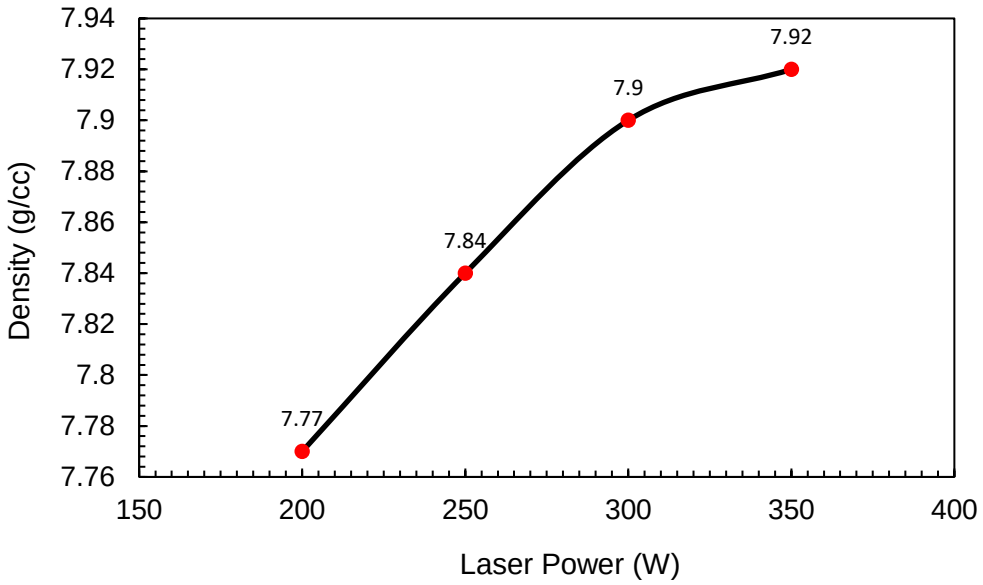

Fig. 4.9 Density from Archimedes method

4.3 Effect of laser scan speed

Weight loss due to wear increases with an increase in laser scanning speed as shown in the Fig. 4.12. This is explained due to the reason of the laser energy density increase with the decrease in laser scan speed resulting in improved powder densification. The improvement of powder densification with the increase in laser scan speed was validated by the inverse proportionality relationship of the material density with laser scan speed as shown in Fig. 4.11.

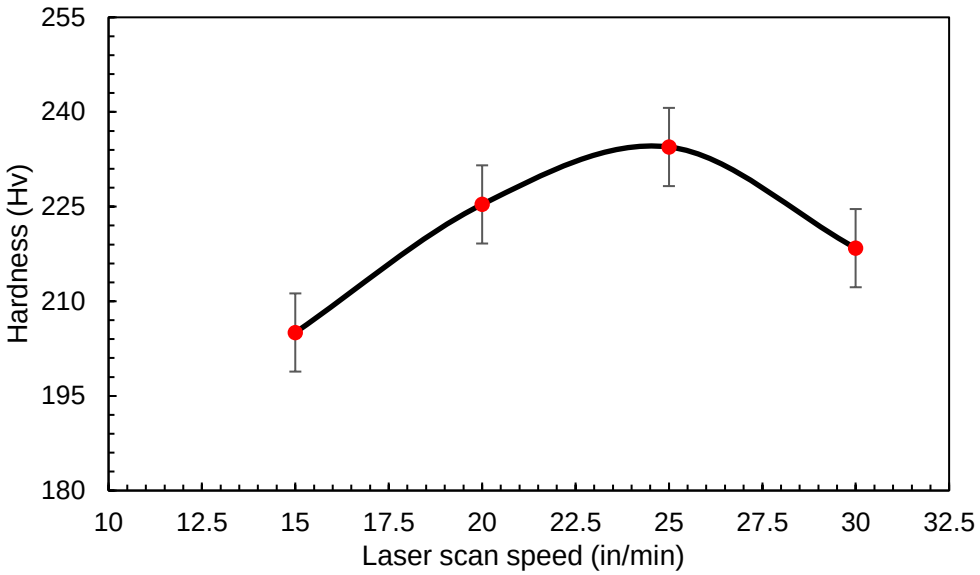

Fig. 4.10 Variation of hardness with laser scan speed

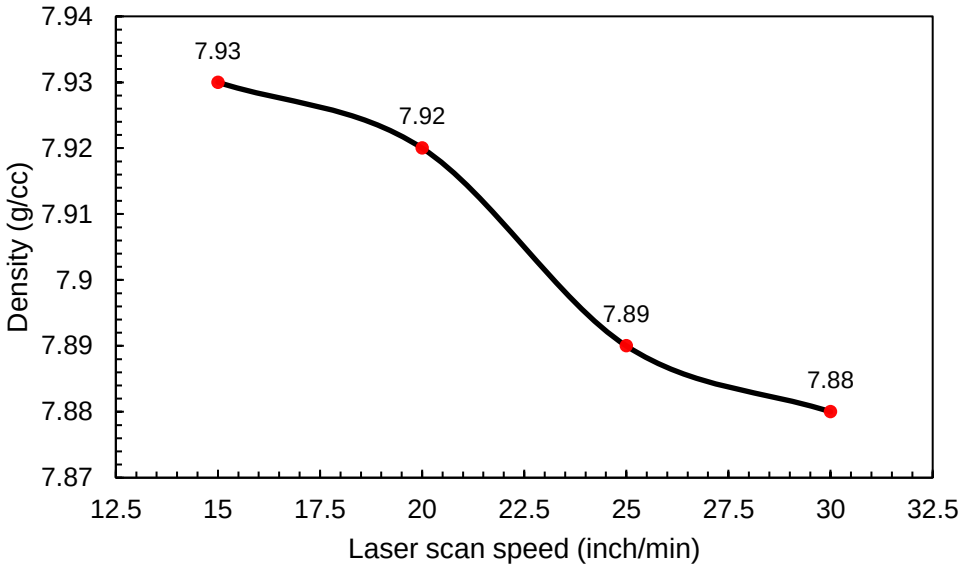

Fig. 4.11 Variation of density with laser scan speed

Increased powder densification results in more resistance to plastic deformation and delamination. The deformed, un-delaminated material oxidizes due to frictional heating of the wear test and oxidizes to form tribo-oxide layer, which is adhered to the wear track due to the compaction of the rotating wear ball or removed as worn debris after the wear test. The mechanism is substantiated in scanning electron microscopy. The features of adhered debris, worn patches, and material fracture

characterize the scanning electron micrographs of the wear tracks. Similar wear track features were obtained during the dry sliding wear characterization of stainless steel 316 L [24, 68, 72]. The figures Fig. 4.13 and Fig. 4.14 depicts that adherence of debris is reduced as a function of increasing scan speed; material fracture is enhanced with increased scan speeds, and the worn patch is more at higher scan speeds. As laser scan speed increases, the adhesion of wear debris is less and material wear is high. The deformation and resistance to delamination results in the material layer oxidizing are inversely proportional to powder densification. Poor powder densification results in low material integrity and low resistance to deformation resulting in increased wear at higher laser scan speeds. Relatively high laser energy density equivalent to the highest laser power sample contributes to wear phenomenon here with the lack of adhesion sites. Hence, the weight loss due to wear increase with increasing laser scan speeds.

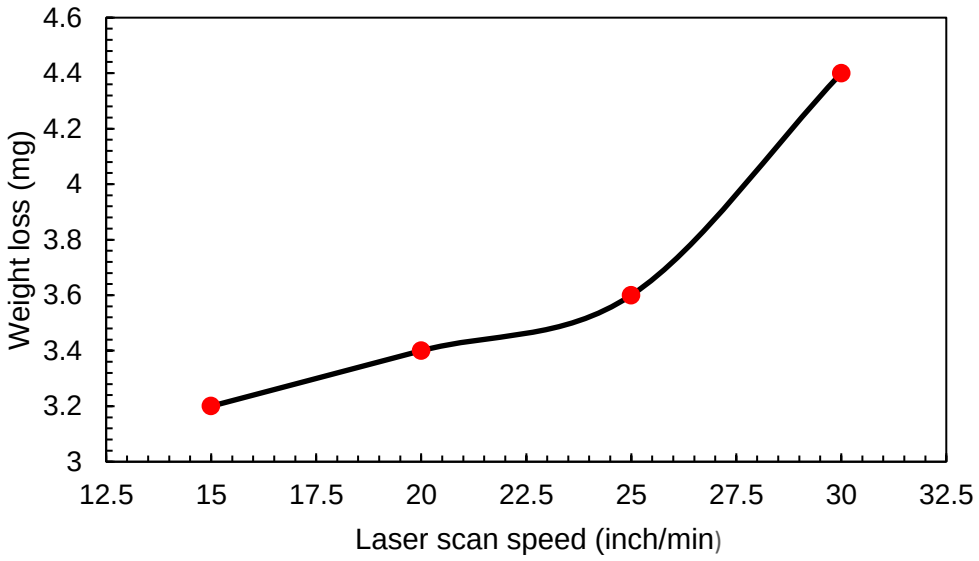

Fig. 4.12 Weight loss after 60 minutes

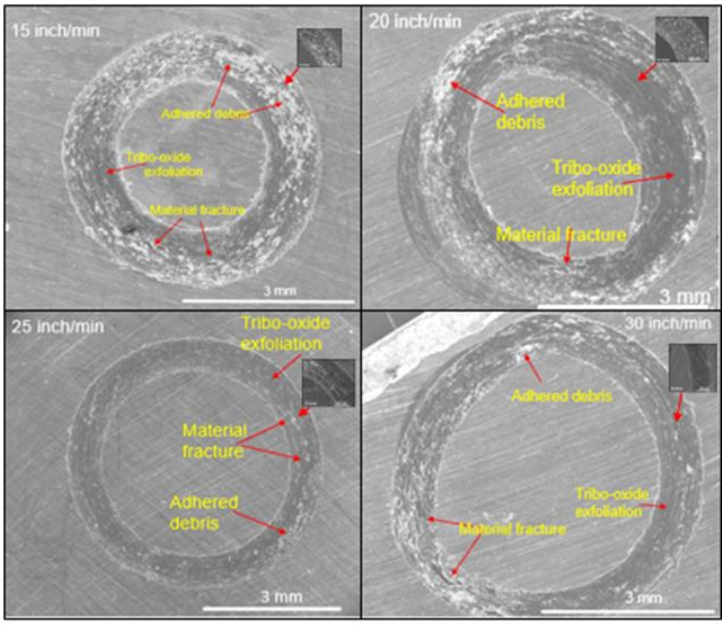

Fig. 4.13: SEM of samples processed at different levels of laser scan speed

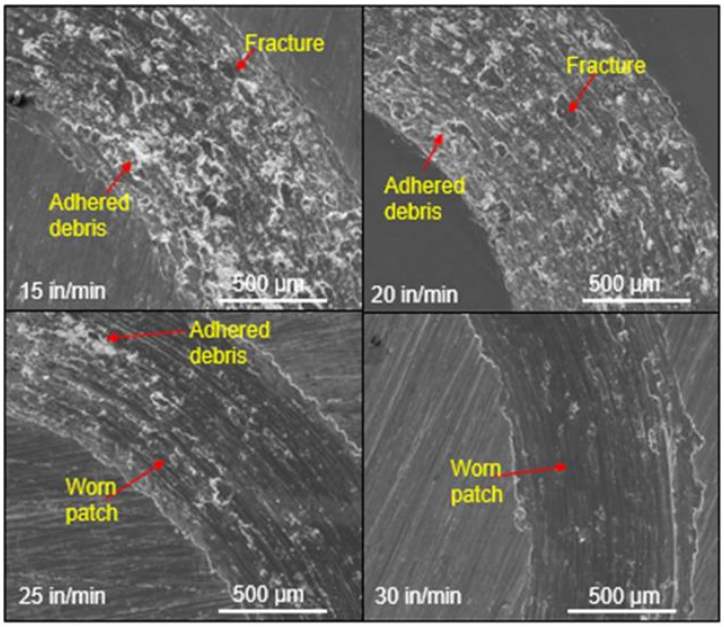

Fig. 4.14: SEM of insets of wear track as shown in Fig. 4.13

At lower laser scan rates when laser energy density is high, the weight loss due to wear is observed to be lesser than that of wrought stainless steel 316 L sample. Hence, this wear performance of additively manufactured sample is better than that wrought at high laser energy densities. This result encompasses the weight loss of 5.1 mg at the same conditions of wear characterization. The scanning electron micrograph of the wrought stainless steel 316 L wear track (Fig. 4.1) illustrates

the characteristic feature of material fracture predominating. The higher wear resistance of the additively manufactured sample is also attributed to the increased hardness as reported in Table 3 and Fig. 4.10. It is of paramount importance to reiterate and juxtapose the research work of Y. Sun et al [24]. They have experimentally studied and demonstrated the wear behavior of SLM® of 316 L stainless steel under dry sliding conditions. The sliding wear test was conducted using a pin-on-disk for a duration of 3600s at 120 rpm. The spherical slider employed was a stainless steel bearing ball of 6 mm diameter. A contact load of 10 N was applied in the experimentation. The effect of laser processing parameters and the wear was related to the percentage volume composition of porosity. They reported higher wear of SLM® stainless steel 316 L compared to wrought stainless steel 316 L. The arrived at the conclusion that the wear increases with the increase in laser scanning speed in selective laser melting (SLM®) of stainless steel 316 L.

4.4 Effect of powder deposition rate

The effect of powder deposition rate was found to be inconsistent with the tribological characteristics of stainless steel 316 L processed by LENS® process as observed in Fig. 4.15. This is because the powder deposition rate is not related to laser energy density. Powder deposition rate does not influence the microstructural evolution during the LENS® process. The obtained minimal weight loss at the powder deposition rate of 8 rpm instigate that recommendation of 8 rpm powder deposition rate as a good candidate concerning the print duration.

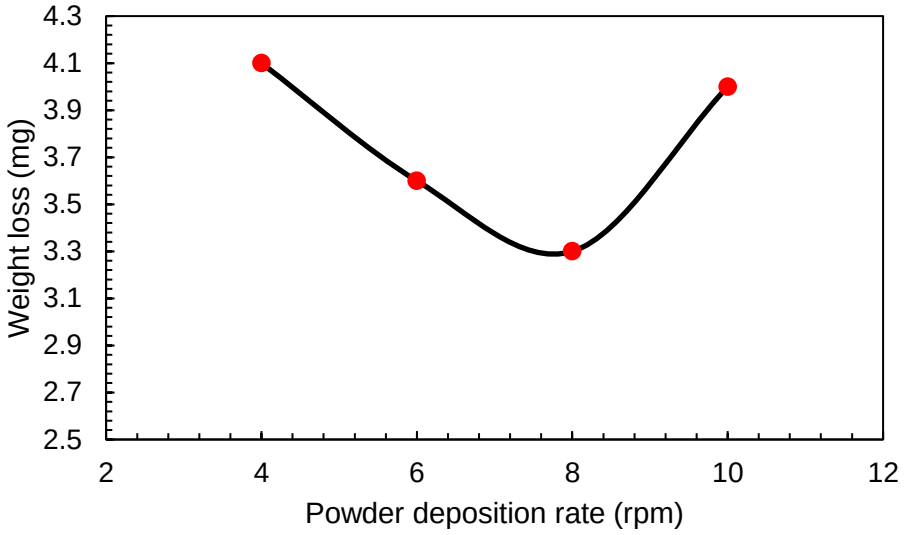

Fig. 4.15 Weight loss measured after 60 minutes of wear testing

CHAPTER V

CORROSION ANALYSIS

The current chapter discusses the potentiodynamic polarization corrosion characteristics of wrought stainless steel 316 L. The effect of LENS® parameters such as laser power, laser scan speed, and powder deposition rate on the potentiodynamic polarization corrosion properties are evaluated.

5.1 Corrosion characteristics of wrought stainless steel 316 L

The E_{corr} values in this experimentation are comparable to those in the literature [24, 27-29, 73-76]. Hence, the E_{corr} of wrought sample obtained in this experiment as depicted in Fig. 5.1 is used for comparing with the stainless steel 316 L additively manufactured in the LENS® process.

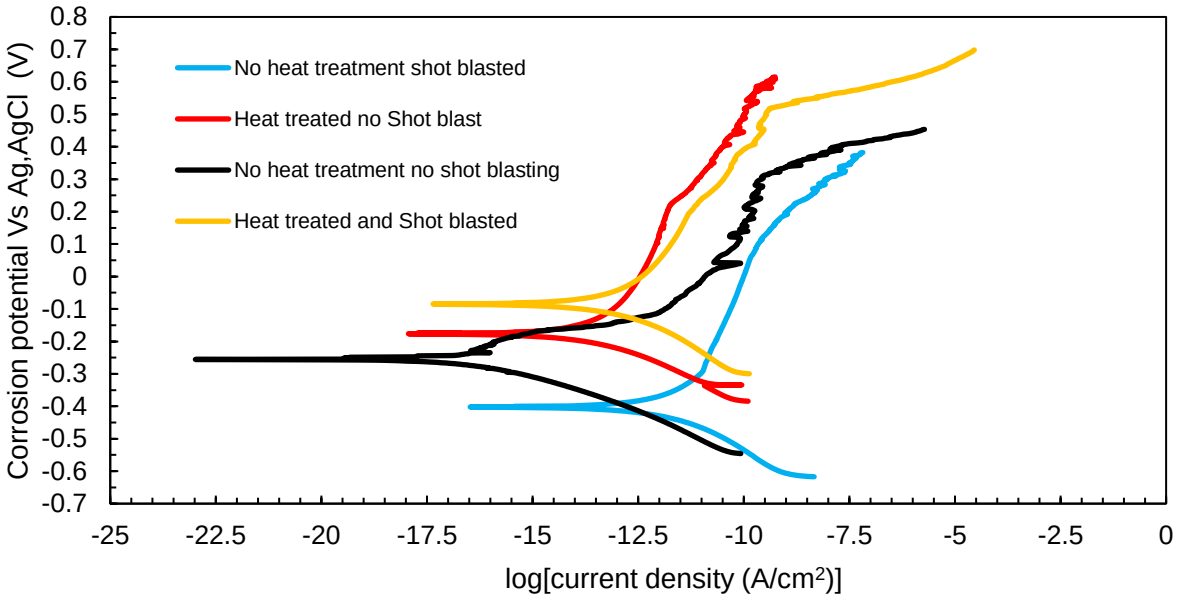

Fig. 5.1 Electrochemical characteristics of wrought stainless steel 316 L

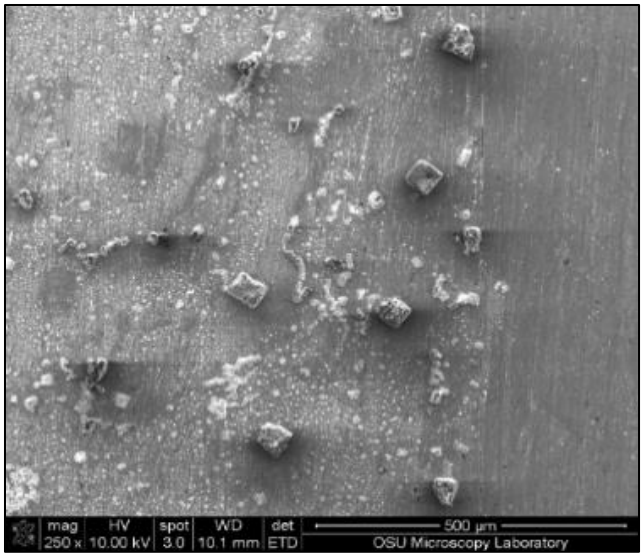

Fig. 5.2 Corrosion product chromium oxide in wrought stainless steel 316 L

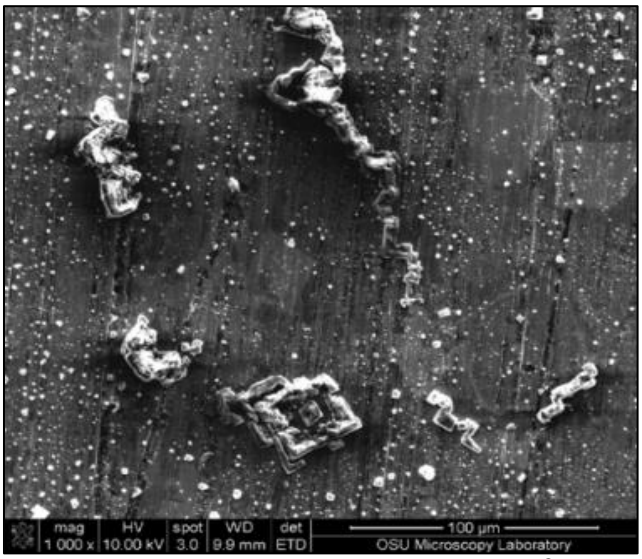

Fig. 5.3 Corrosion product chromium oxide in LENS® stainless 316 L

Strehblow et al, Stefanov et al, Stoudt et al found that a passivation layer of chromium oxide is formed in chloride-rich aqueous environment [25, 28, 77] as shown in Fig. 5.2 and Fig. 5.3.

5.2 Effect of laser power

Phase transformations can potentially result in a difference of corrosion behavior. The phases observed are consistent with the phases present in the stainless steel 316 L powder at all power

levels as shown in Fig. 5.4 indicating that the samples processed at different levels of laser power are homogeneous in phase composition [8, 29, 67, 73]. The sharp peaks indicate the residual stresses are minimal. However, no δ ferrite phase is observed which results from rapid solidification. This is observed and explained by Yuan et al. At low scan speeds and subsequent cooling rates, there exists ample time for the complete phase transformation of δ ferrite to γ austenite leaving lesser than 0.1% of ferrite if any present. Lesser than 0.1% is undetectable in XRD [8]. The occurrence of the phases is also validated from the Schaeffler diagram from the Cr and Ni equivalence [8, 29, 67, 73].

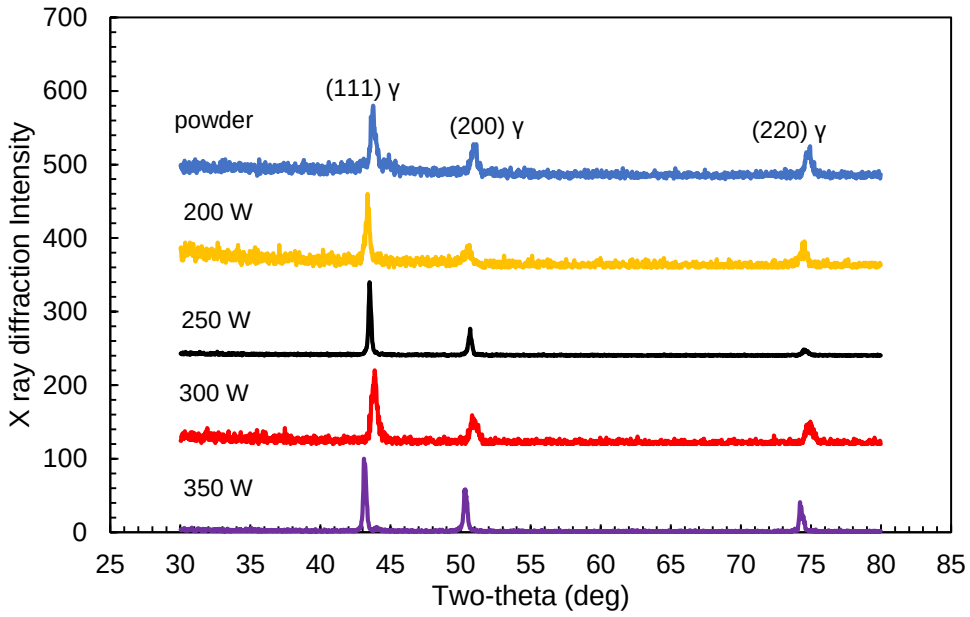

Fig. 5.4 Phase compositions as seen in X-ray diffraction characterization

The micrographs obtained in this research is similar and comparable to the ones obtained by I.Y.Khalfallah et al in the laser treatment of austenitic stainless steel [27]. The stainless steel 316 L additively manufactured in the LENS® process microstructure vary drastically from the microstructure of wrought stainless steel 316 L. Yuan et al report grain size range of 1-9 µm during additive manufacturing of stainless steel 316 L [8]. Khalfallah et al observe grain size range of 2-3 µm during high solidification [27]. This is comparable to the average grain size range obtained in this research. The smaller grain size as explained earlier details the incidence of lower corrosion

potential of the additive manufacturing samples compared to the wrought stainless steel 316 L. It is observed from Fig. 5.5 and Fig. 5.6 that the corrosion potential increases with the increase in laser power. This signifies that as the laser power increases, the corrosion resistance increases.

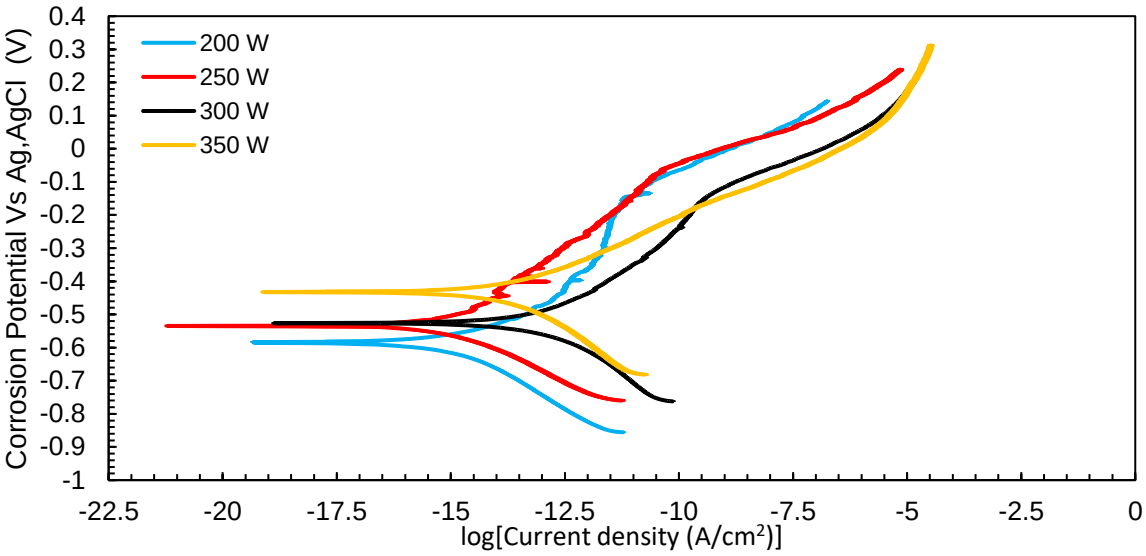

Fig. 5.5 Comparison of electrochemical behavior at various power levels

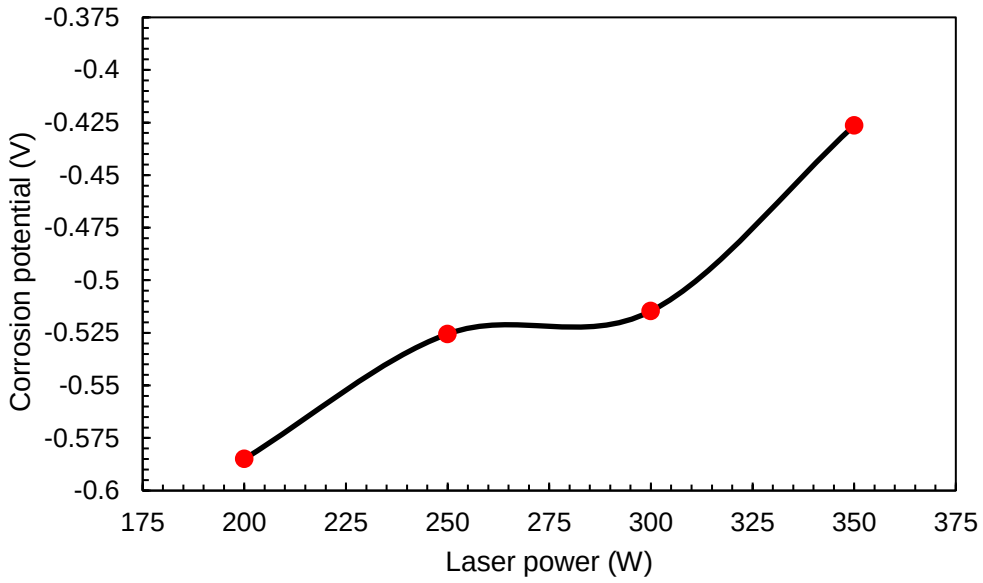

Fig. 5.6 Variation of corrosion potential with laser power

5.3 Effect of laser scan speed

The phases were consistent in all the samples and were comparable to the phases occurring in the stainless steel 316 L powder as seen in Fig. 5.7. The peaks were sharp indicating that the residual stresses developed during the printing are minimal. This presents the discussion that the phases are homogeneous and do not contribute to a difference in corrosion behavior. It can be observed that the corrosion potential increases with an increase in the laser scan speed overall. This indicates that the corrosion resistance is higher at higher levels of laser scan speed. This is observed in the figures Fig. 5.8, Fig. 5.9 and Fig. 5.10.

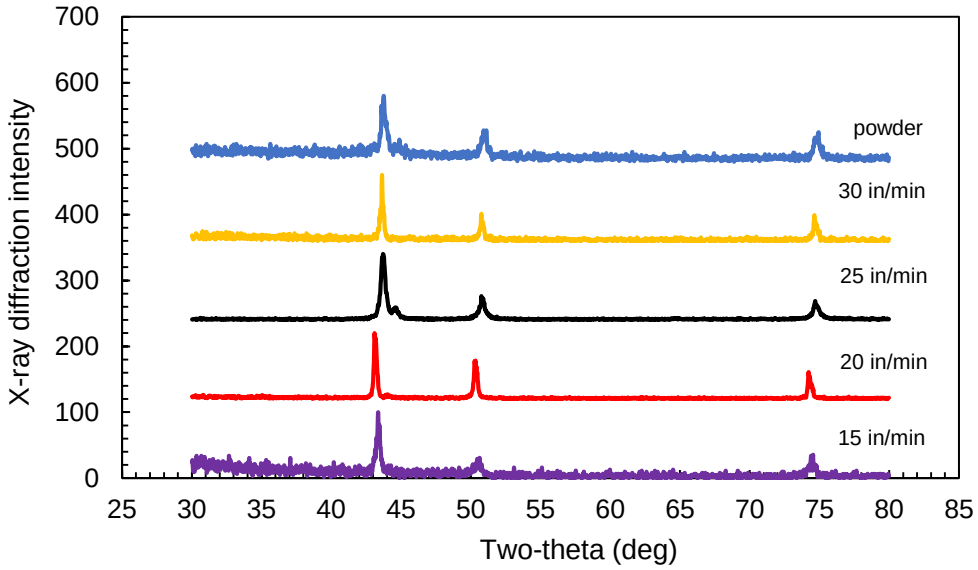

Fig. 5.7 Phase composition as seen in X-ray diffraction characterization

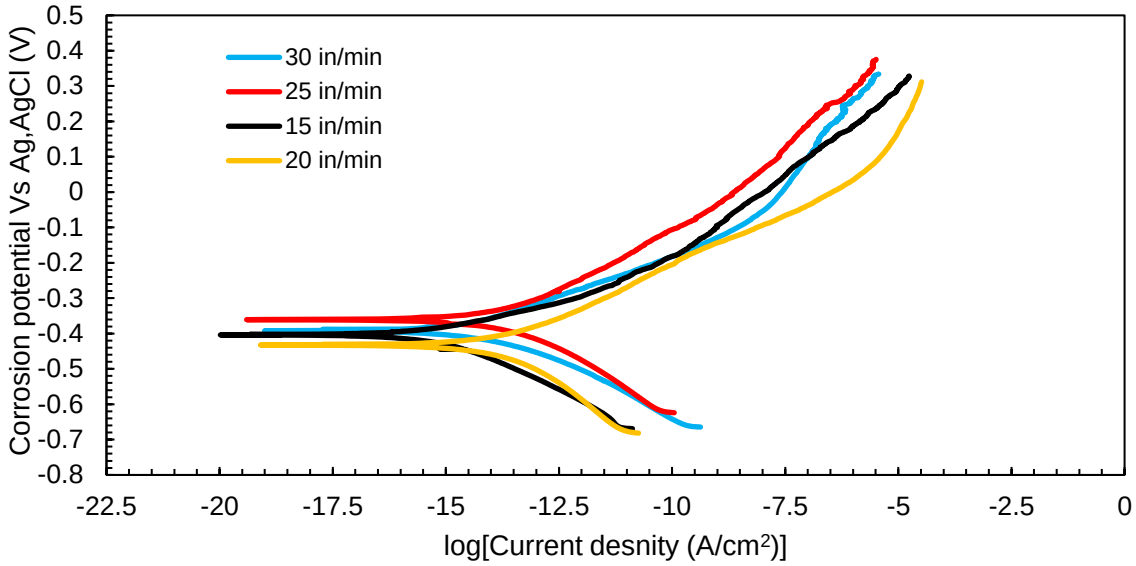

Fig. 5.8 Comparison of electrochemical behavior at various scan speed levels i) As Built

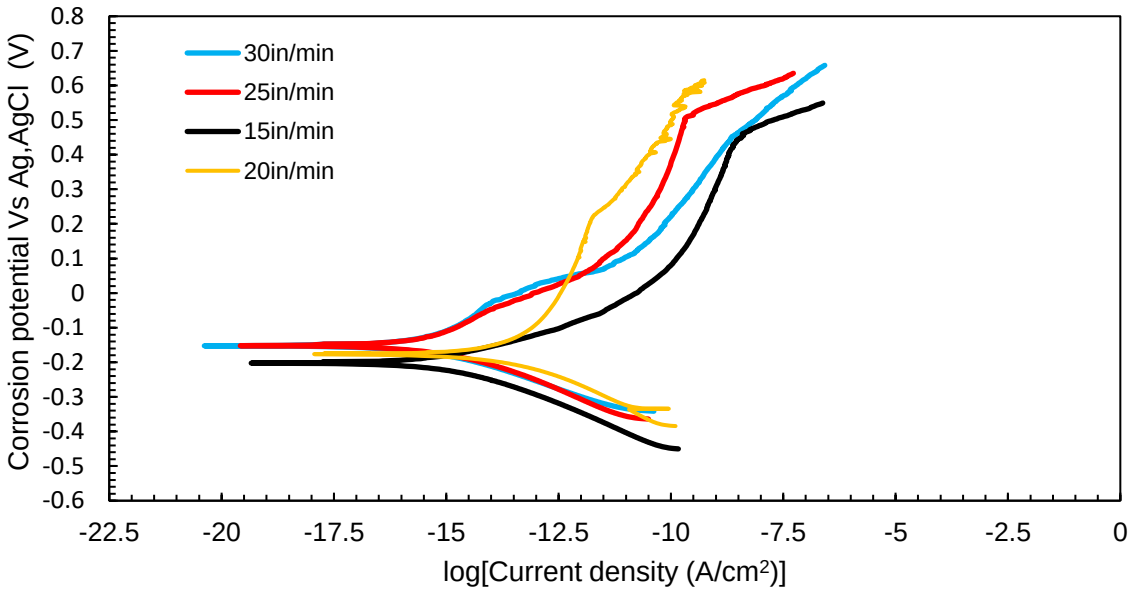

Fig. 5.9 Comparison of electrochemical behavior at various scan speed levels ii) Polished

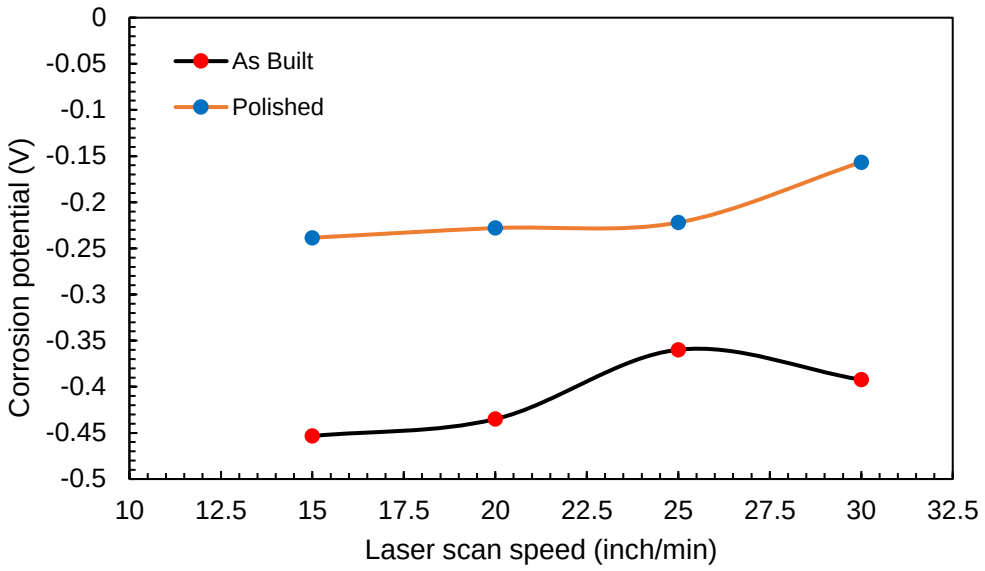

Fig. 5.10 Variation of corrosion potential with laser scan speed

The discrepancy of reduction in corrosion potential from 25 inch/min to 30 inch/min as seen in Fig. 5.10 is attributed to the sporadic increase in surface roughness increase in the as-built surface depicted in Fig. 5.11. This discrepancy is validated through the observation in the polished surface. This is illustrated in Fig. 5.10.

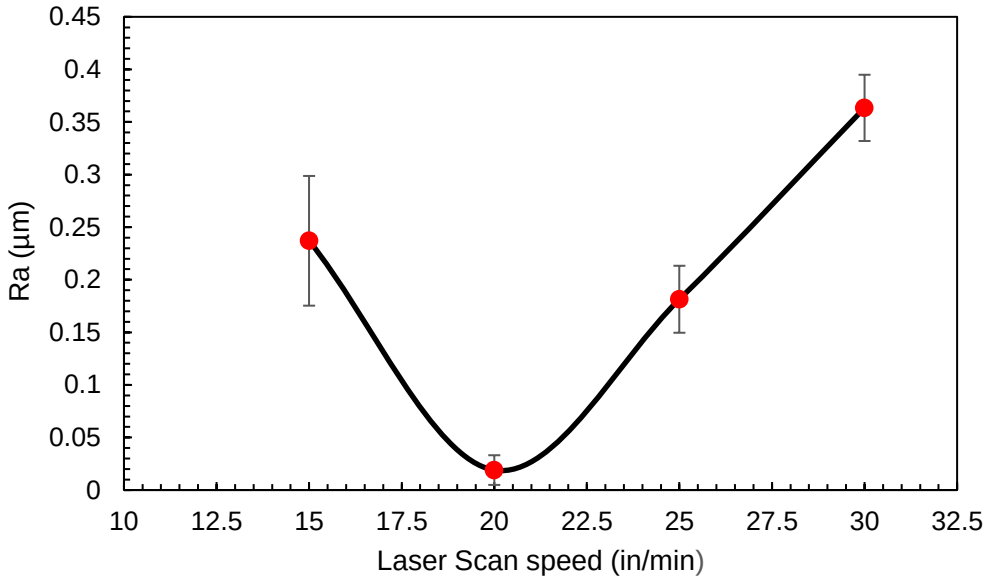

Fig. 5.11 Variation of surface roughness with laser scan speed

5.4 Effect of powder deposition rate

The effect of powder deposition rate was not consistent with the corrosion characteristics of stainless steel 316 L processed by the LENS® process in both as-built surface and polished surface. This is observed in figures Fig. 5.12, Fig. 5.13 and Fig. 5.14. This is because the powder deposition rate does not influence the laser energy density or powder densification. Hence, it does not induce any changes in the microstructural evolution. The processing parameters are always studied by extrapolating its effect on the macroscopic properties directly. However, the processing parameters directly affect the microstructural evolution, which in turns affects the macroscopic properties.

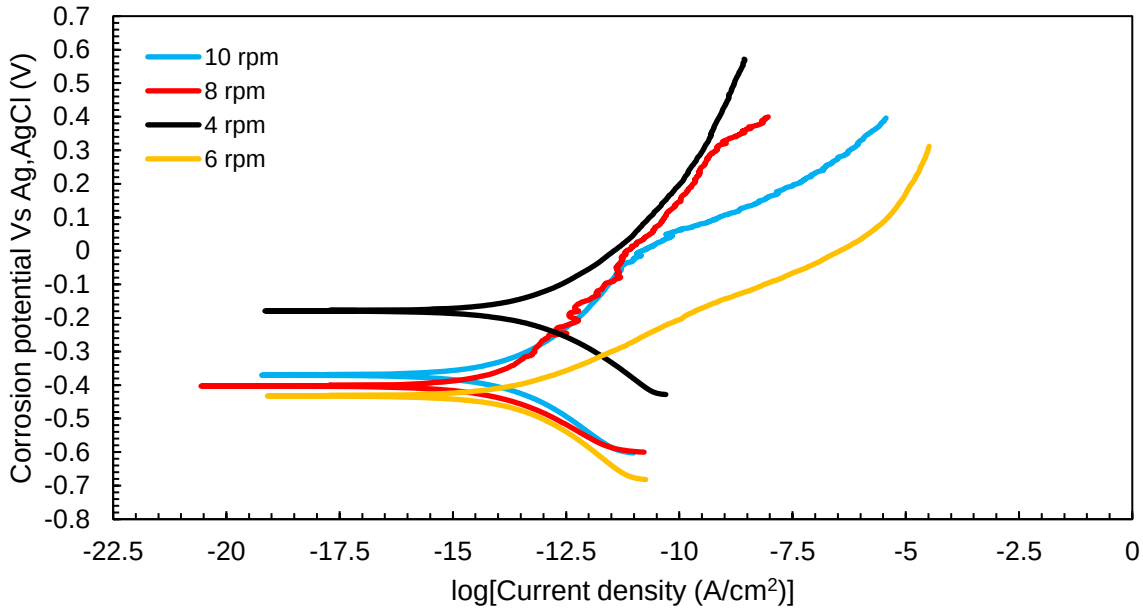

Fig. 5.12 Comparison of electrochemical behavior at various powder deposition rates i) As Built

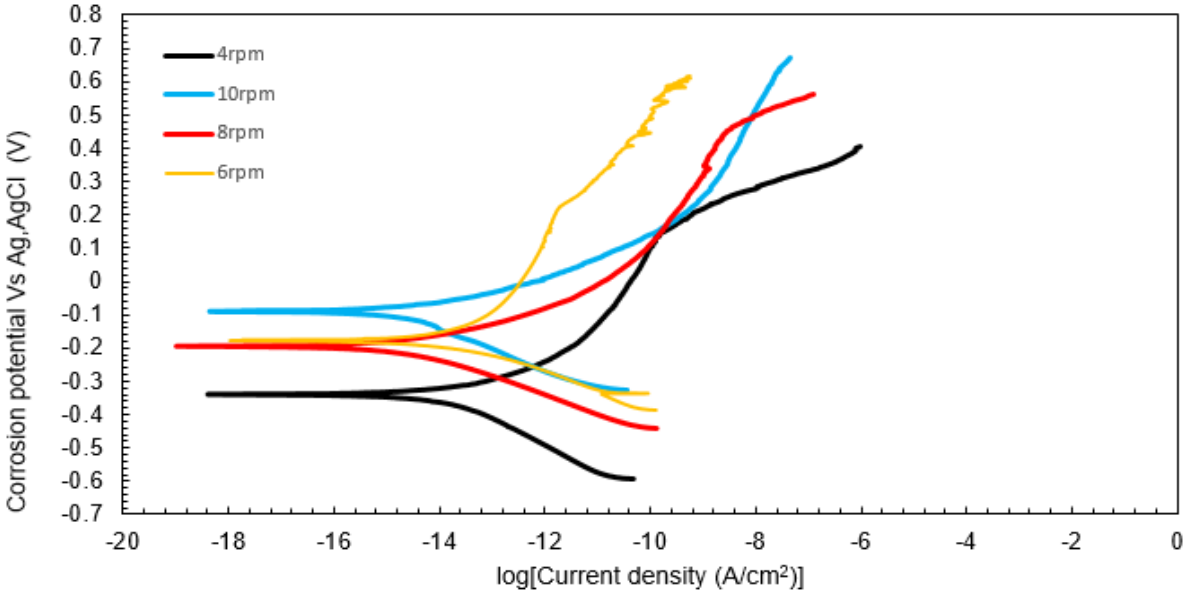

Fig.5.13 Comparison of electrochemical behavior at various powder deposition rates ii) Polished

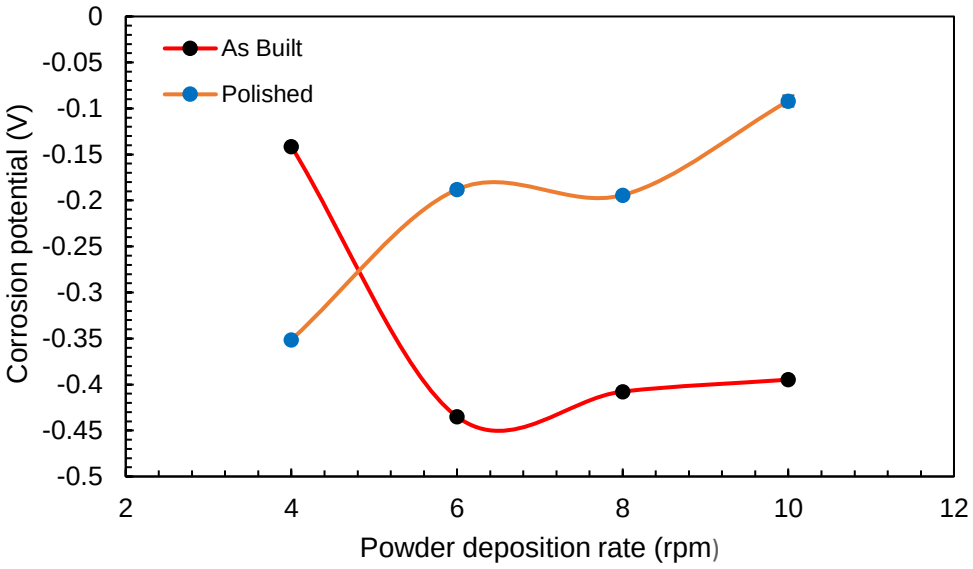

Fig. 5.14 Variation of corrosion potential with powder deposition rate

5.5 Analysis of pitting corrosion

The following sections discuss the pitting corrosion characteristics of wrought stainless steel 316 L in 10% dilute HCl environment. The effect of LENS® parameters such as laser power, laser scan speed, and powder deposition rate on the pitting corrosion properties are evaluated.

The polarizability of HCl and the dipole-ion interaction between the H_2O and HCl molecules result in the increased concentration of H^+ and Cl^- ions in the 10% dilute HCl solution. Stainless steel 316 L, being a metal alloy has the tendency to lose electrons in oxidation. The pool of electrons is loosely held constituting the metallic bond. During pitting, the electrons are lost at the site of corrosion initiation due to oxidation. The electrons are transferred to the surface where reduction reaction occurs. The reduction is the electrochemical process of the gain of electrons. In this case, the electrons are consumed in the process of reducing [78]. The energy dispersive spectroscopy analysis (EDS) of non-pitted and pitted sample is shown in Fig. 5.16 and Fig. 5.18 respectively.

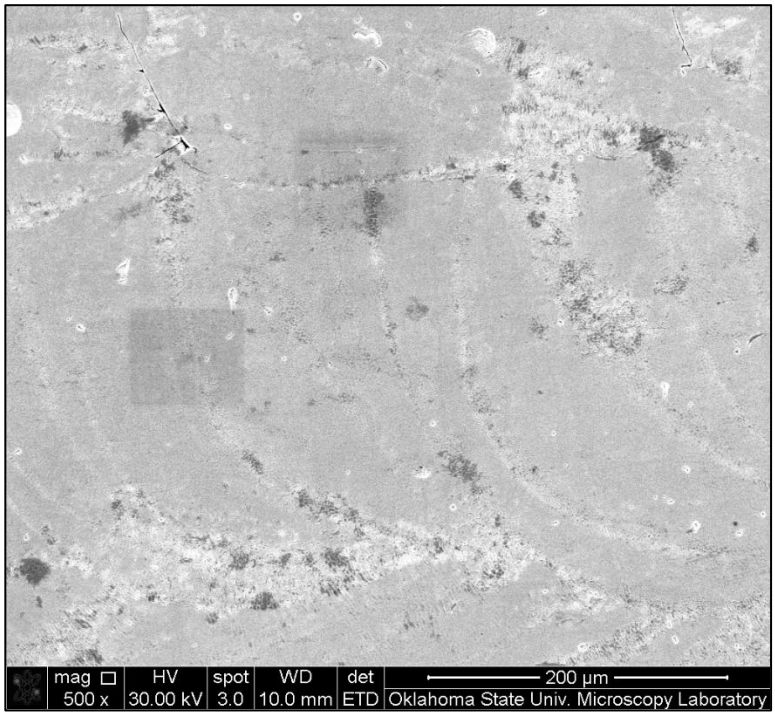

Fig. 5.15 SEM of as-built non-pitted stainless steel 316 L

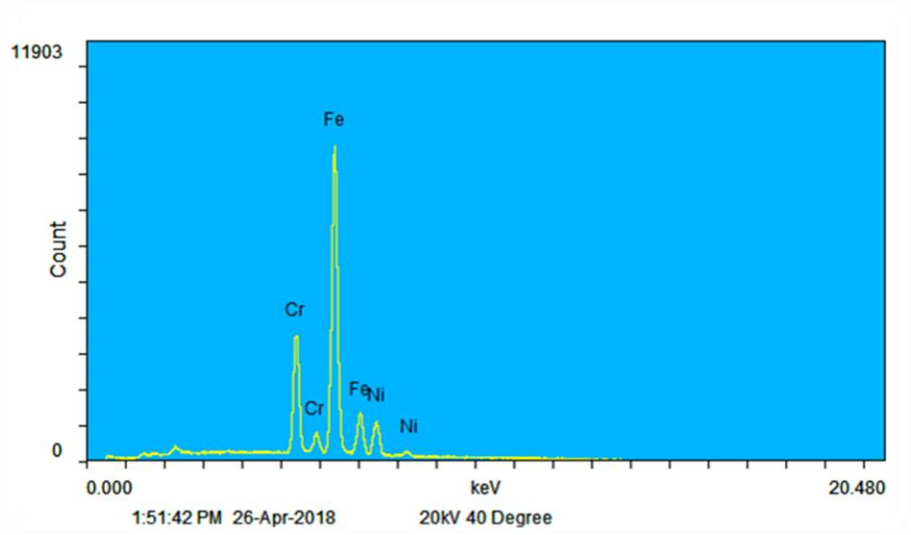

Fig. 5.16 EDS corresponding to the SEM shown in Fig. 5.15

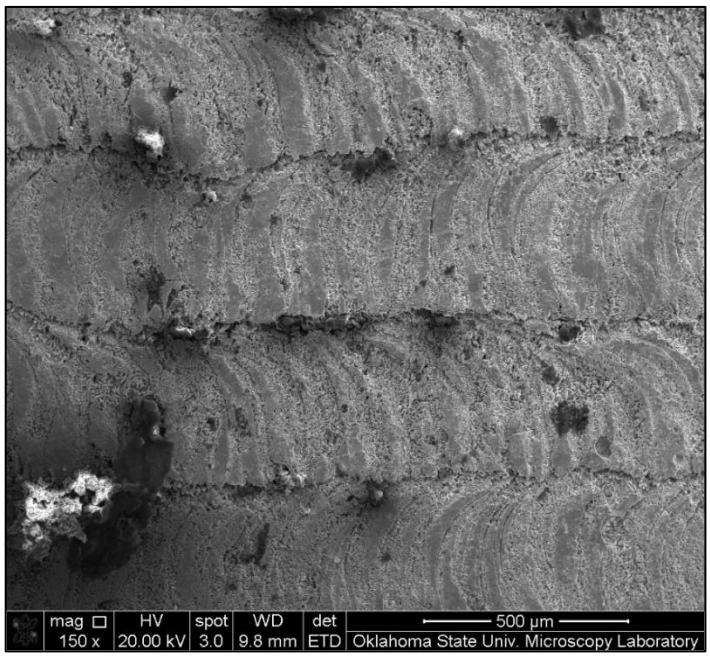

Fig. 5.17 SEM of pitted stainless steel 316 L

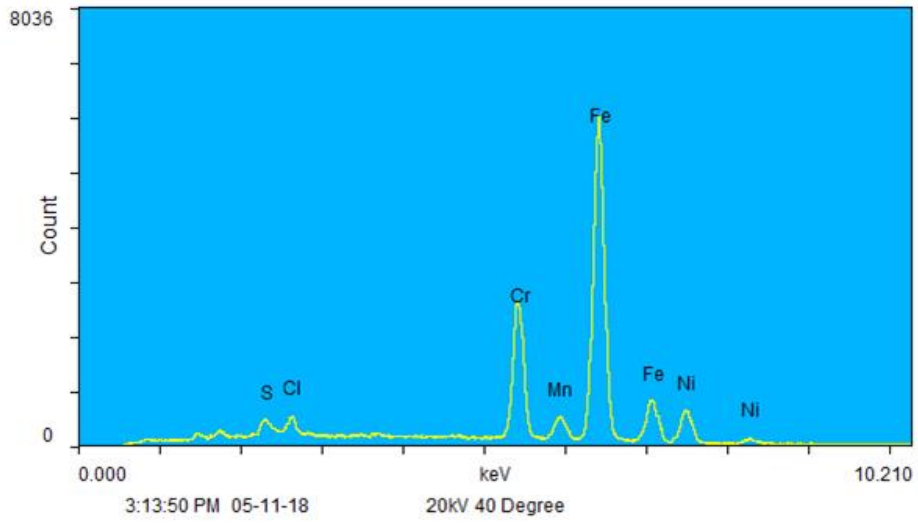

Fig. 5.18 EDS corresponding to the SEM shown in Fig. 5.17

The scanning electron micrographs (SEM) show that the form of corrosion that occurred in the additive manufacturing – LENS® processed stainless steel 316 L is pitting as illustrated in the figures Fig. 5.19 – Fig. 5.39). Scanning electron microscopy and the SEM images are the manifestations of the internal material phenomenon that is traceable to the macroscopic material properties. The SEM images (Fig. 5.19 – Fig. 5.39) showed no trace of scaling or deposition thereby negating the possibility of uniform attack type of corrosion. SEM depicted no trace of galvanic corrosion for there was no homogeneous metal contact. The edges of the samples were intentionally lacquered to inhibit crevice corrosion. Grain boundary sensitization was not observed (with the exception of a discrepancy explained in later sections). This subverts the incidence of intergranular corrosion in the experimentation. The SEMs exuded no evidence for crack initiation, crack propagation, erosion attacks, selective leaching to account the corrosion mechanism to stress crack corrosion, erosion corrosion, or selective leaching.

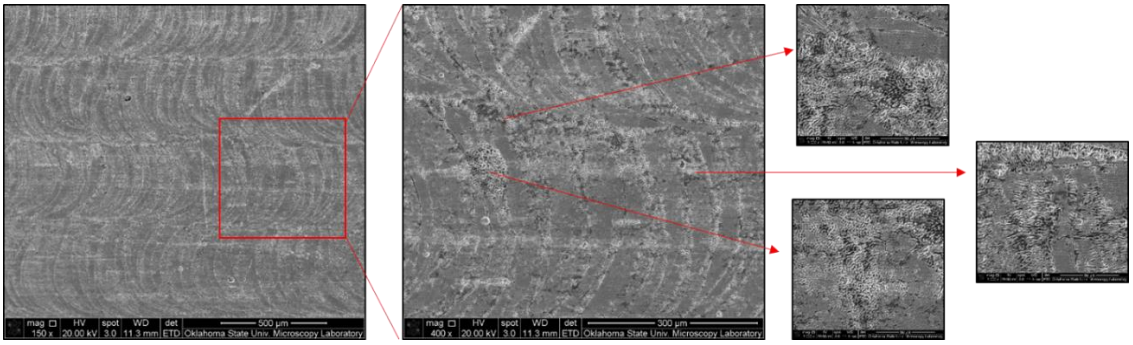

Fig. 5.19 SEM showing pitting of as-built sample processed at laser power - 200 W, scan speed - 20 inch/min, powder deposition rate- 6 rpm

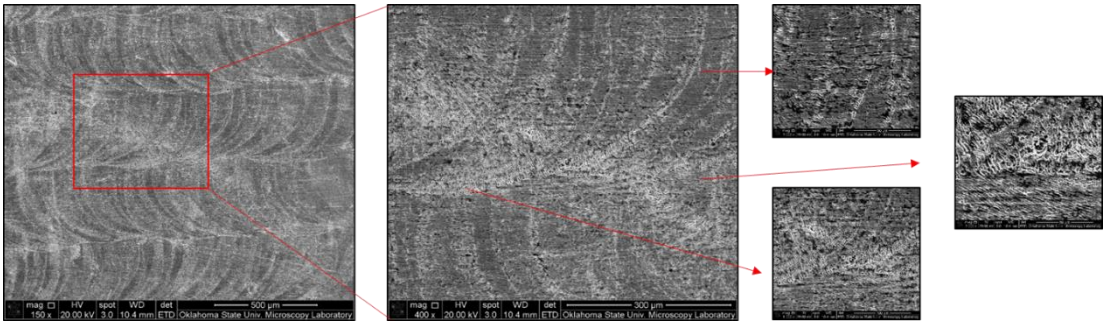

Fig. 5.20 SEM showing pitting of as-built sample processed at laser power-300 W, scan speed - 20 inch/min, powder deposition rate- 6 rpm

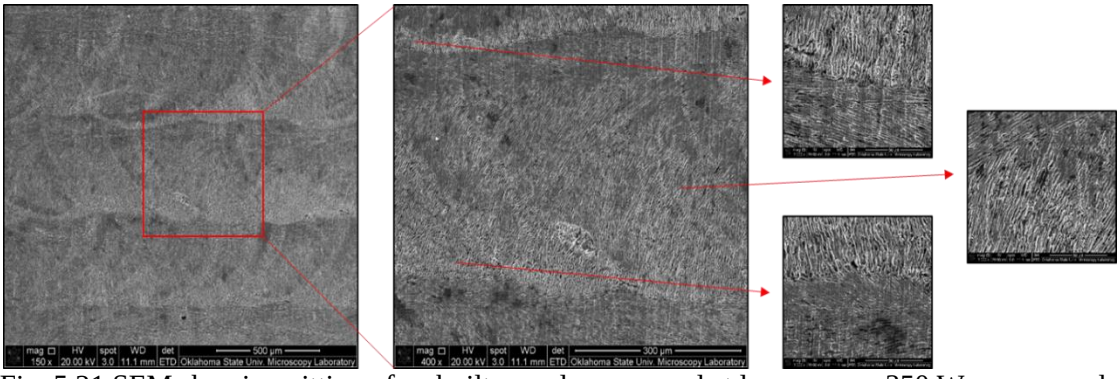

Fig. 5.21 SEM showing pitting of as-built sample processed at laser power-350 W, scan speed - 20 inch/min, powder deposition rate-6 rpm

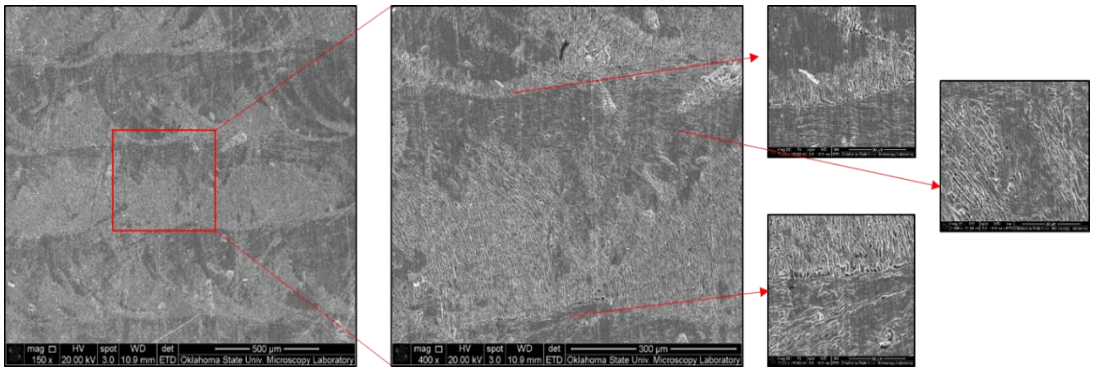

Fig. 5.22 SEM showing pitting of as-built sample processed at laser power-350 W, scan speed -15 inch/min, powder deposition rate-6 rpm

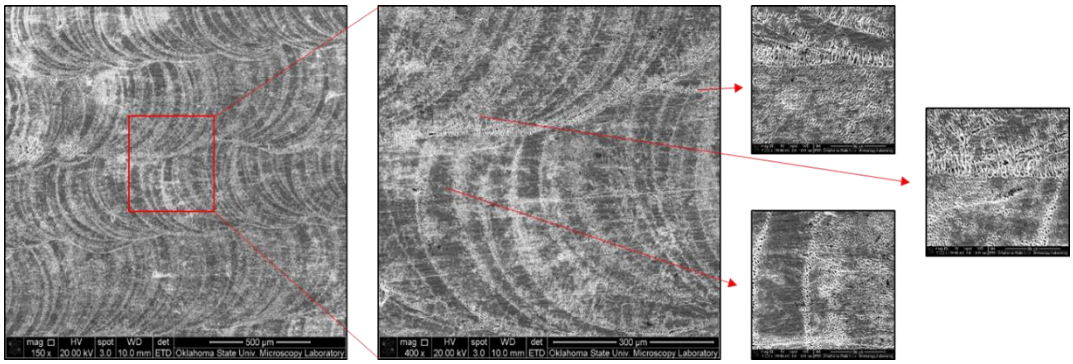

Fig. 5.23 SEM showing pitting of as-built sample processed at laser power-350 W, scan speed -25 inch/min, powder deposition rate -6 rpm

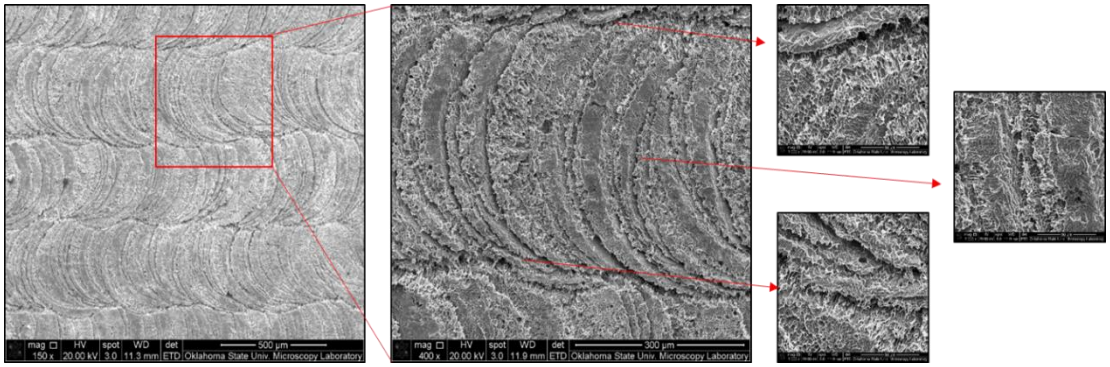

Fig. 5.24 SEM showing pitting of as-built sample processed at laser power-350 W, scan speed-20 inch/min, powder deposition rate-4 rpm

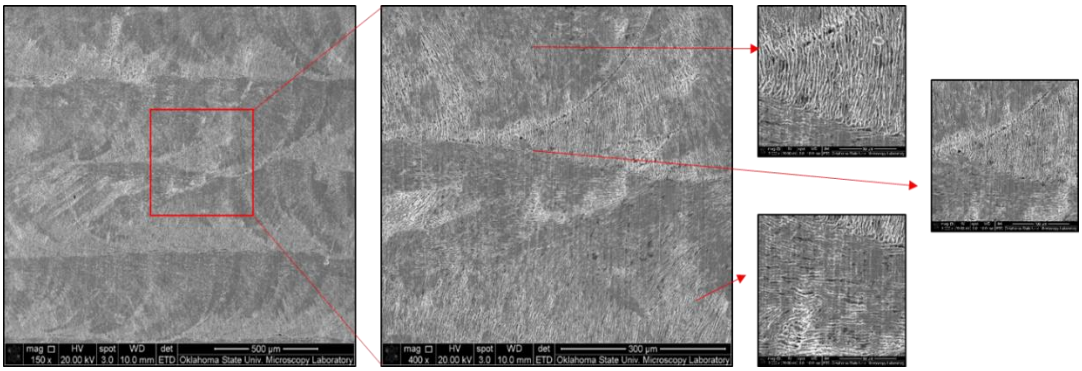

Fig. 5.25 SEM showing pitting of as-built sample processed at laser power-350 W, scan speed-20 inch/min, powder deposition rate-8 rpm

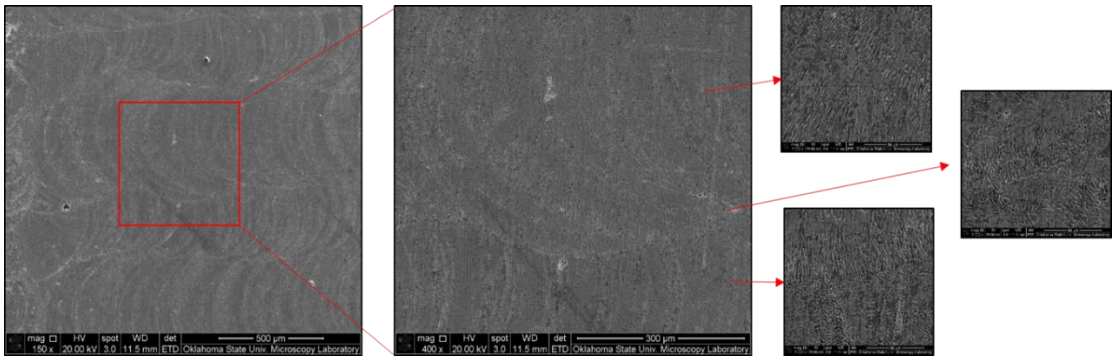

Fig. 5.26 SEM showing pitting of as-built sample processed at laser power-350 W, scan speed-20 inch/min, powder deposition rate-10 rpm

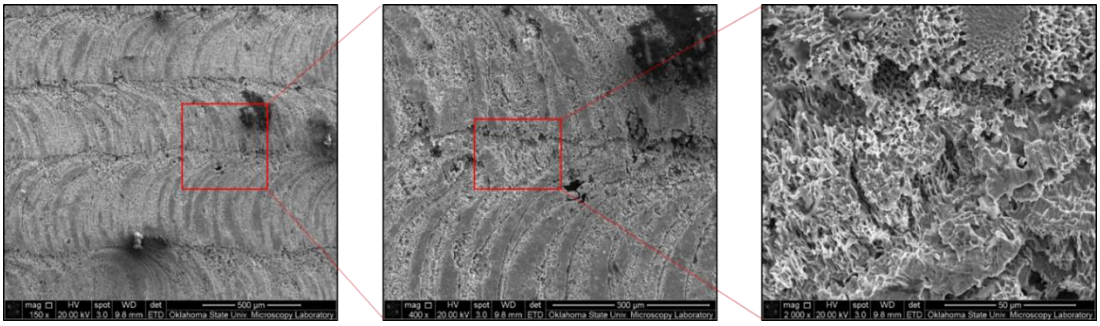

Fig. 5.27 SEM showing pitting of heat-treated sample processed at laser power 200 W, scan speed-20 inch/min, powder deposition rate-6 rpm

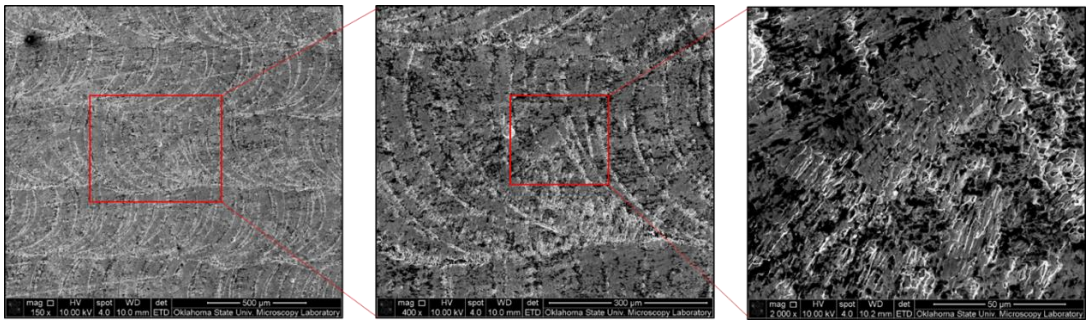

Fig. 5.28 SEM showing pitting of heat-treated sample processed at laser power 300 W, scan speed-20 inch/min, powder deposition rate-6 rpm

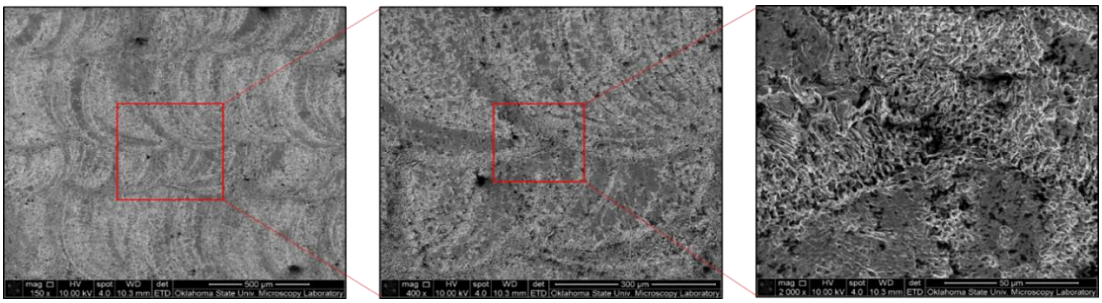

Fig. 5.29 SEM showing pitting of heat-treated sample processed at laser power-350 W, scan speed-20 inch/min, powder deposition rate-6 rpm

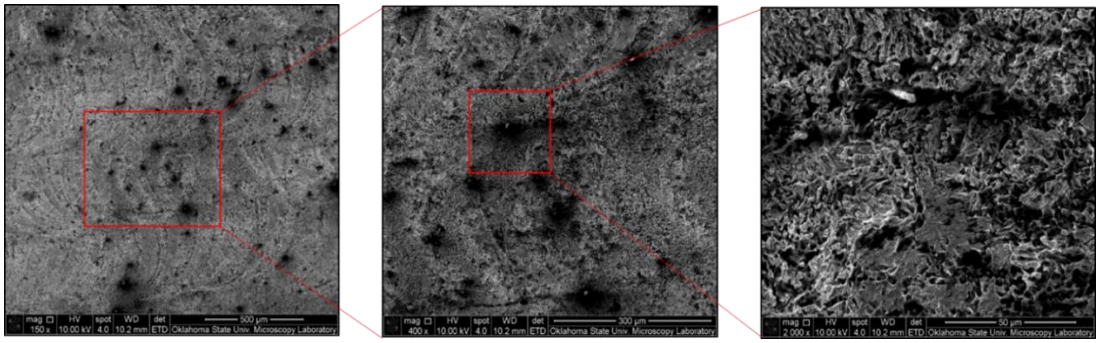

Fig. 5.30 SEM showing pitting of heat-treated sample processed at laser power-350 W, scan speed-15 inch/min, powder deposition rate-6 rpm

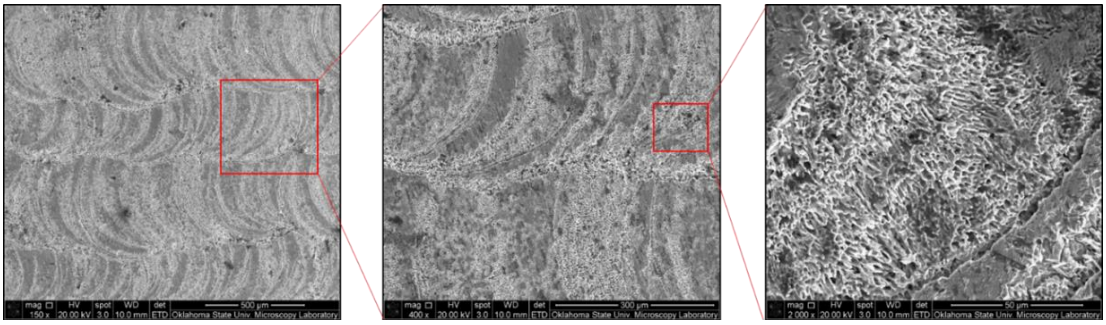

Fig. 5.31 SEM showing pitting of heat-treated sample processed at laser power-350 W, 25 inch/min, powder deposition rate-6 rpm

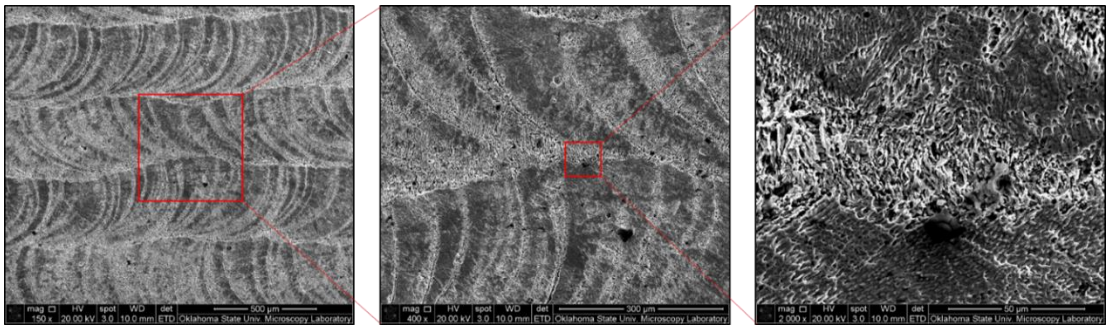

Fig. 5.32 SEM showing pitting of heat-treated sample processed at laser power- 350 W, scan speed-30 inch/min, 6 rpm

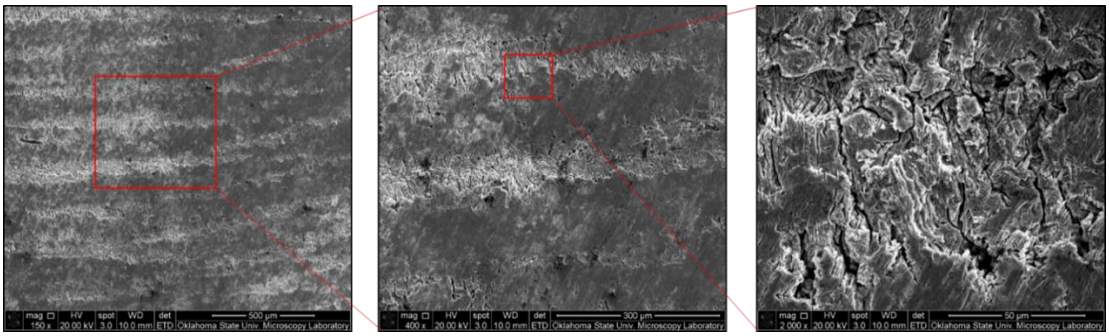

Fig. 5.33 SEM showing pitting of heat-treated sample processed at laser power-350 W, scan speed-20 inch/min, powder deposition rate-4 rpm

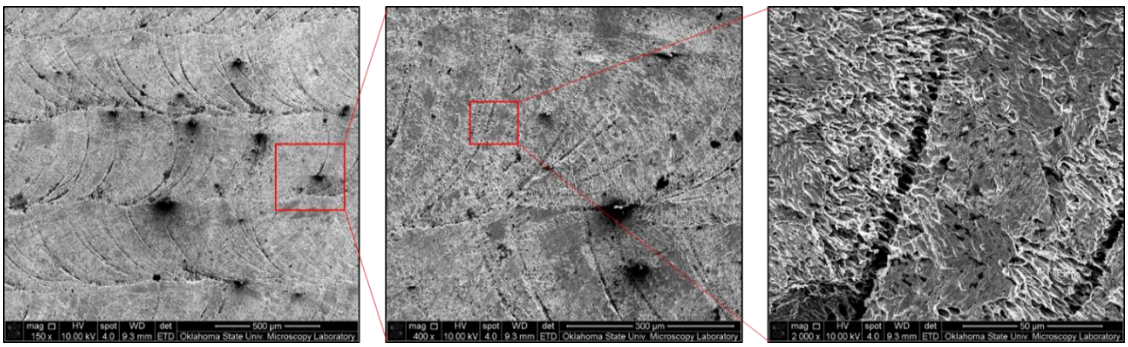

Fig. 5.34 SEM showing pitting of heat-treated sample processed at laser power-350 W, scan speed-20 inch/min, powder deposition rate-8 rpm

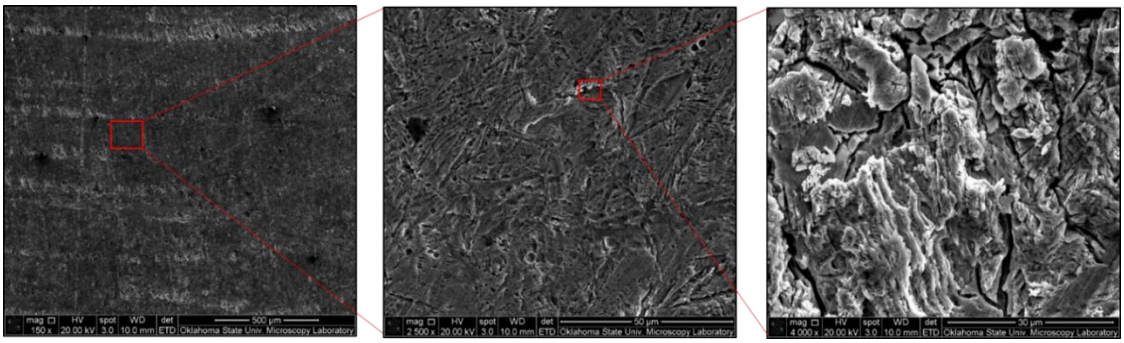

Fig. 5.35 SEM showing pitting of heat-treated sample processed at laser power-350 W, scan speed-20 inch/min, powder deposition rate-10 rpm

Heat treatment process has imparted improved properties in additive manufacturing – direct energy deposition of stainless steel 316 L as indicated earlier in the literature review. The results of the corrosion rate, corrosion penetration rate and maximum pitting depth comparing the properties between as-built and heat-treated conditions vividly showed improvement of pitting resistance in the heat treated samples. The heat treatment for 30 minutes duration at 380 ·C and subsequently slow cooling has served the purpose of stress relieving. The heat treatment process has reduced the internal residual stresses substantially. This is evidently illustrated in the figures (Fig. 5.36 – Fig. 5.39) where uniform and homogeneous pitting is observed.

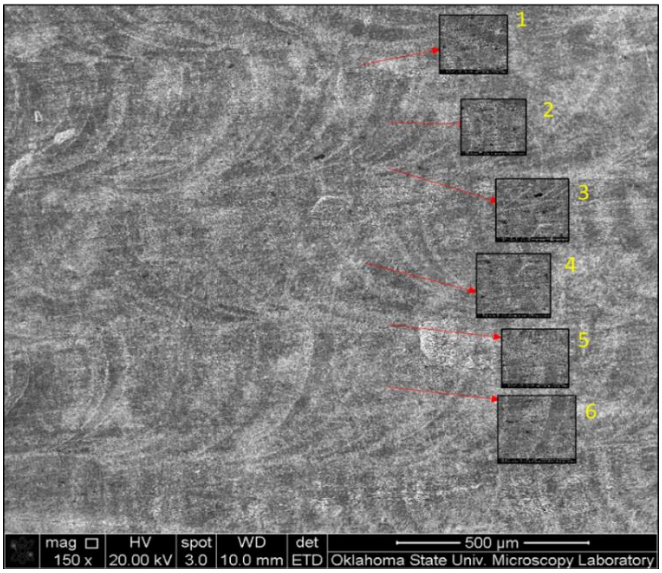

Fig. 5.36 SEM showing pitting of as-built sample processed at laser power-350 W, scan speed-30 inch/min, powder deposition rate-6 rpm

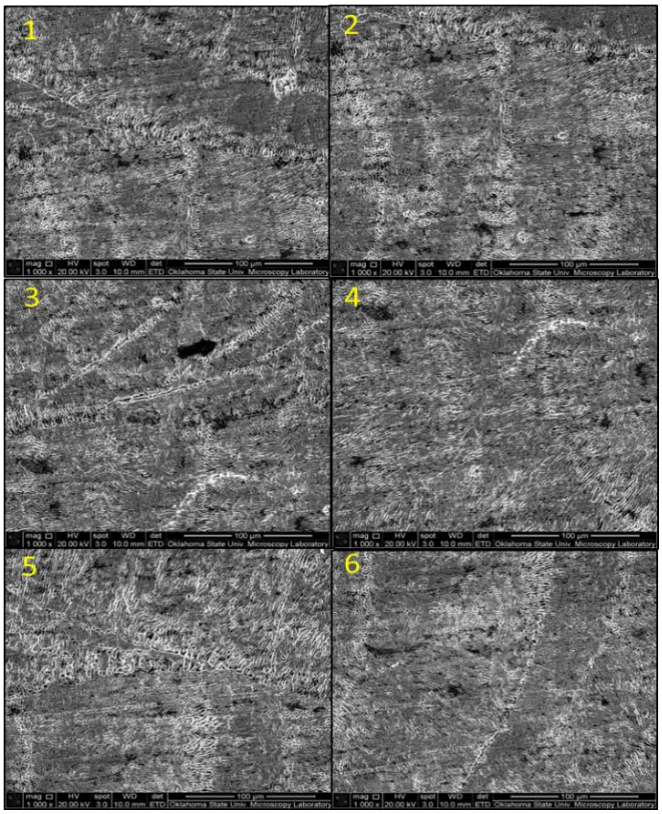

Fig. 5.37 SEM-insets of Fig. 5.36

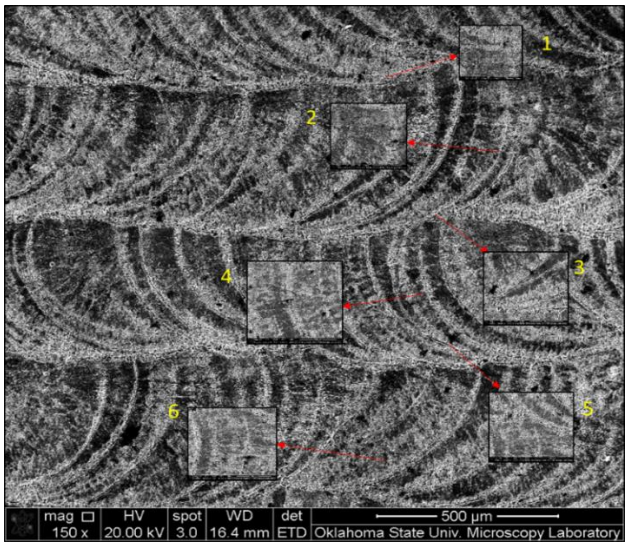

Fig. 5.38 SEM showing pitting of heat-treated sample processed at laser power-350 W, scan speed-30 inch/min, powder deposition rate-6 rpm

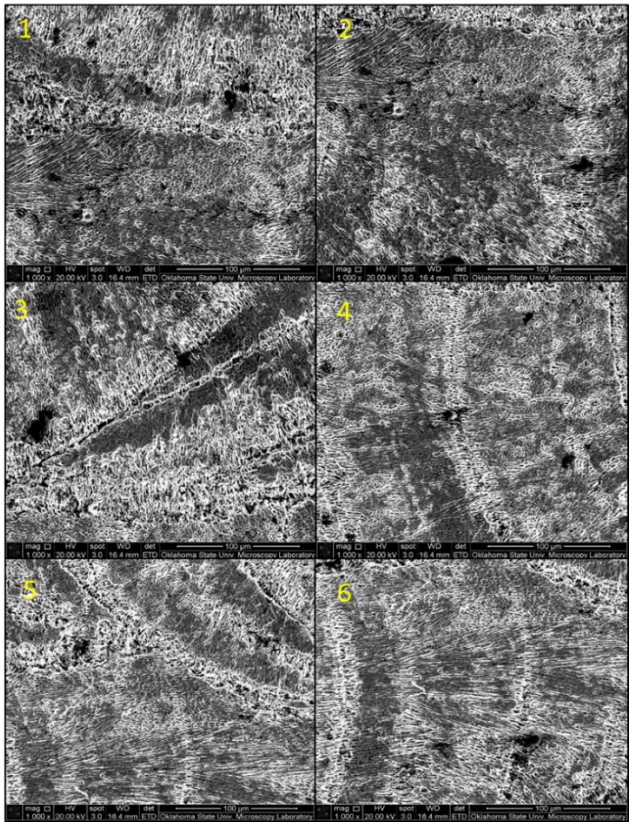

Fig. 5.39 SEM-insets of Fig. 5.38

Homogeneity in pitting is observed at the micro-level as seen in the figures during the stress releveling heat treatment. The pitting depth is reduced at the bulk level in the event of heat treatment. As a result, the pitting resistance is improved in the property scale. This above explanation details the mechanism during heat treatment that ameliorates the corrosion properties of the additively manufactured stainless steel 316 L. The residual stresses are minimized consequently due to the above-discussed internal phenomenon. Enhanced pitting corrosion resistance is a manifestation of the internal phenomenon during heat treatment.

However, to the best knowledge in all researches pertaining to the effect of heat treatment on the properties during additive manufacturing – direct energy deposition of stainless steel 316 L, heat treatment has been promulgated to minimize the internal residual stresses and thermal distortions during the building process. In the current research also, the internal residual stresses were minimized or reduced but the stresses were not completely eliminated. This is because the heat

treatment does not re-melt and form new grains by nucleation and growth. The persisting grains are strain relaxed during the stress-relieving heat treatment and the grains were formed as the result of rapid melting and rapid solidification during the additive manufacturing process. Hence, the corrosion rate, corrosion penetration rate, depth of pitting were different for the different conditions of LENS® processing as observed in the figures Fig. 5.40 – Fig. 5.48.

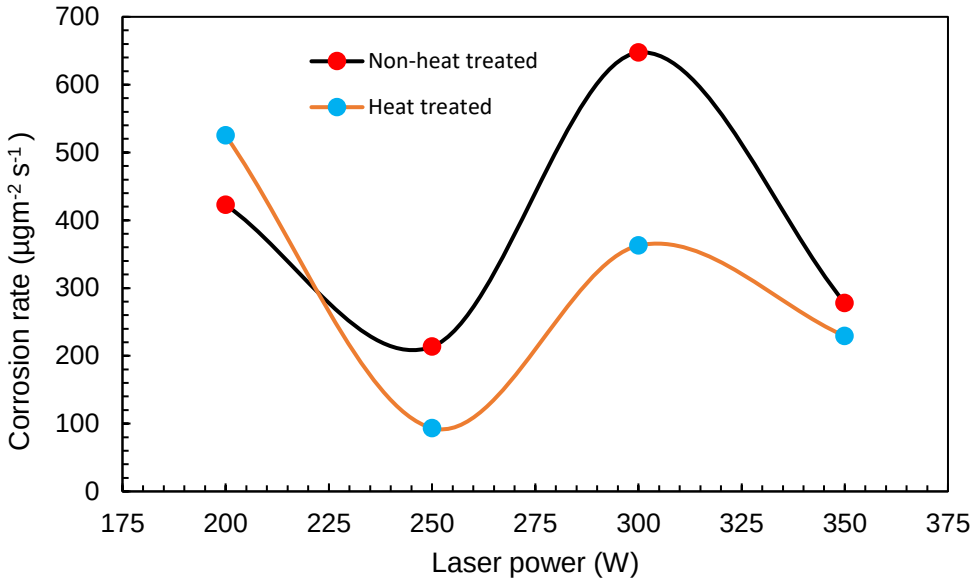

Fig. 5.40 Variation of corrosion rate with laser power

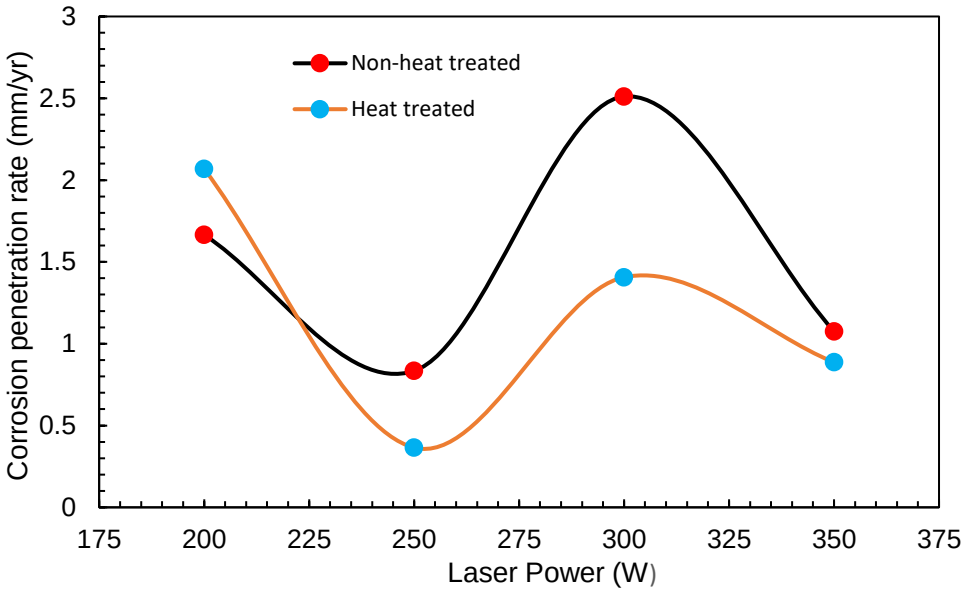

Fig. 5.41 Variation of corrosion penetration rate with laser power

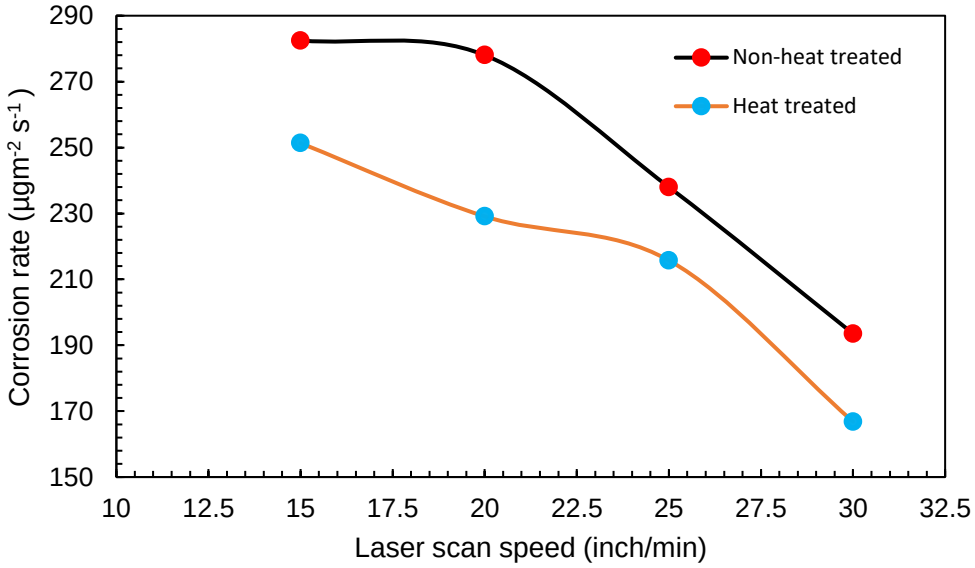

Fig. 5.42 Variation of corrosion rate with laser scan speed

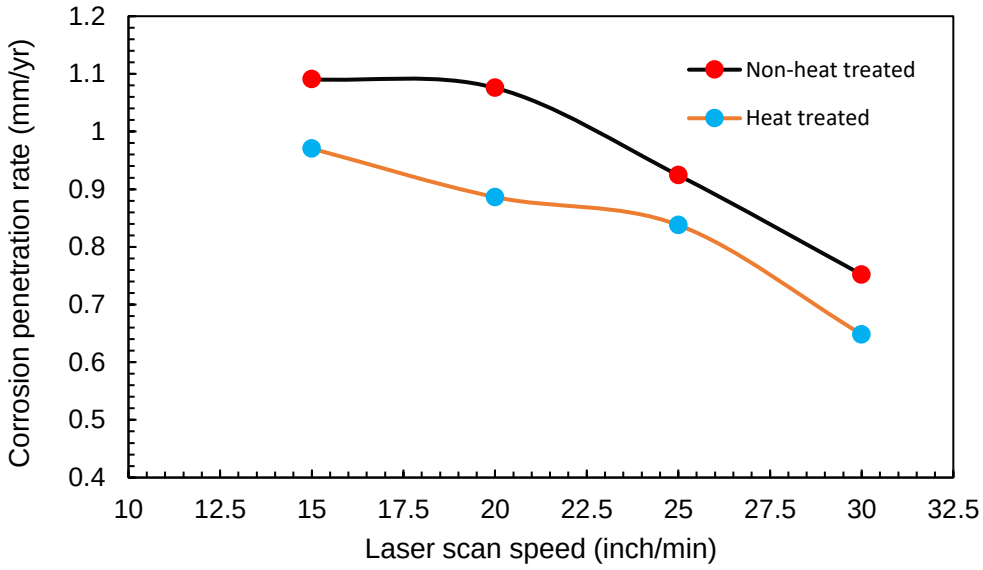

Fig. 5.43 Variation of corrosion penetration rate with laser scan speed

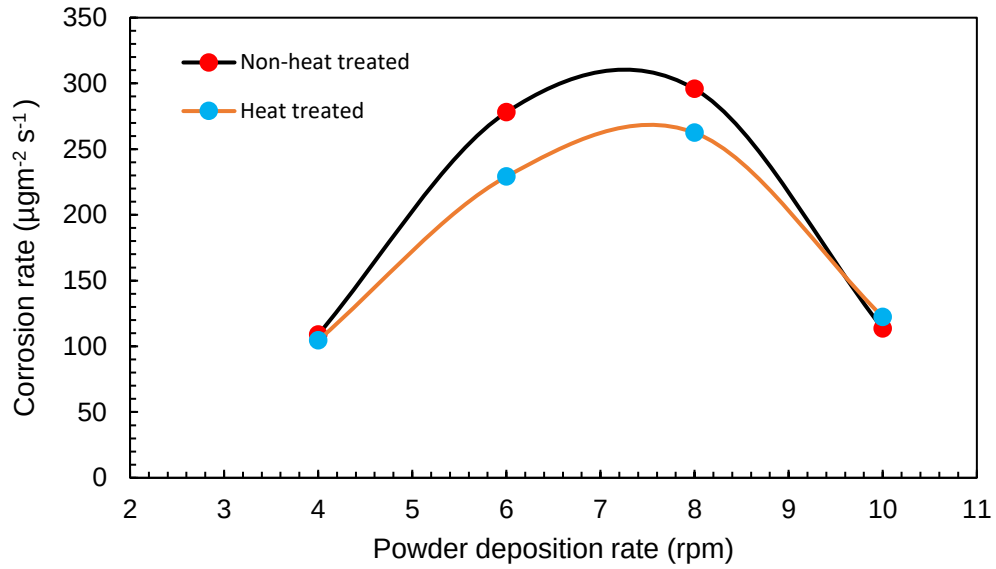

Fig. 5.44 Variation of corrosion rate with powder deposition rate

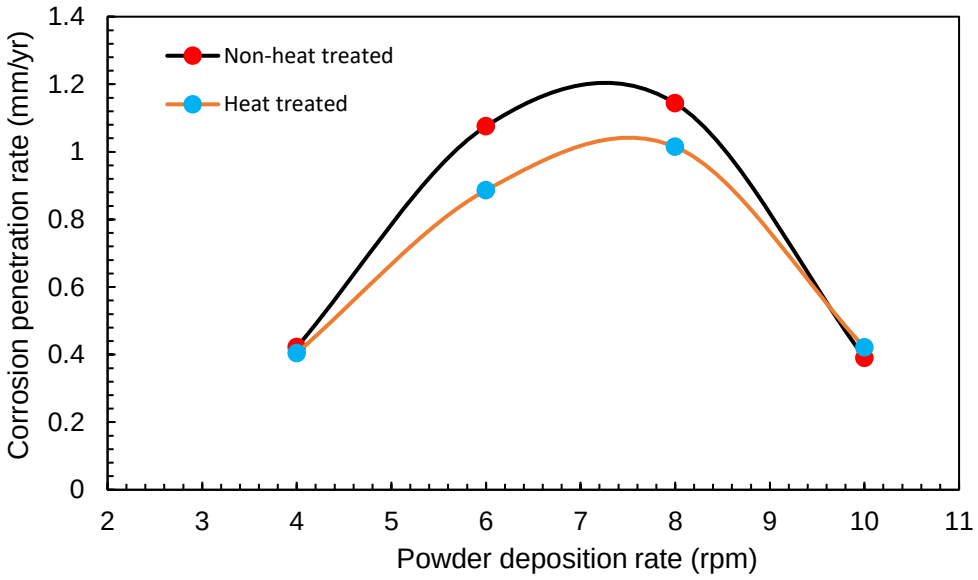

Fig. 5.45 Variation of corrosion penetration rate with powder deposition rate

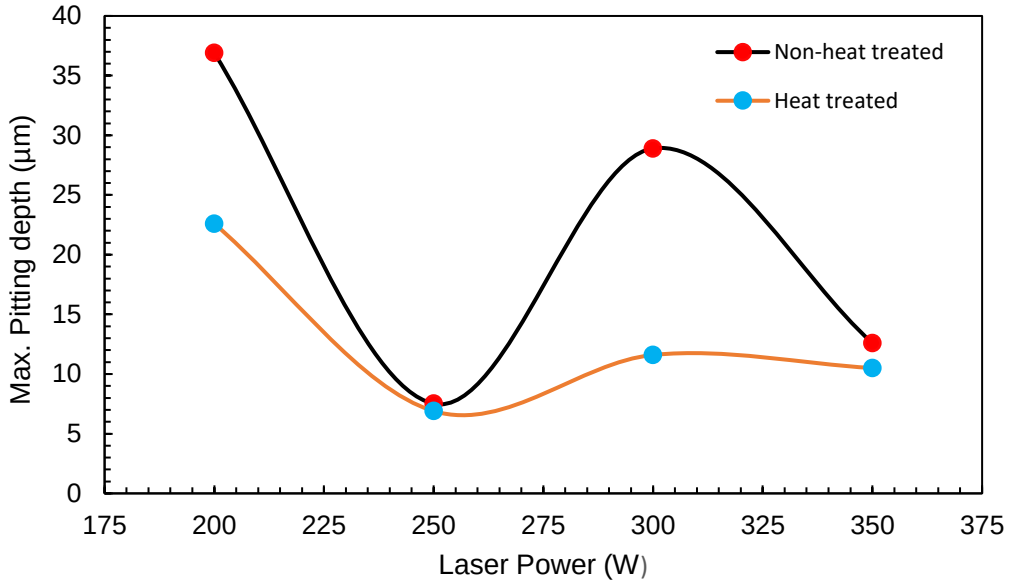

Fig. 5.46 Variation of maximum pitting depth with laser power

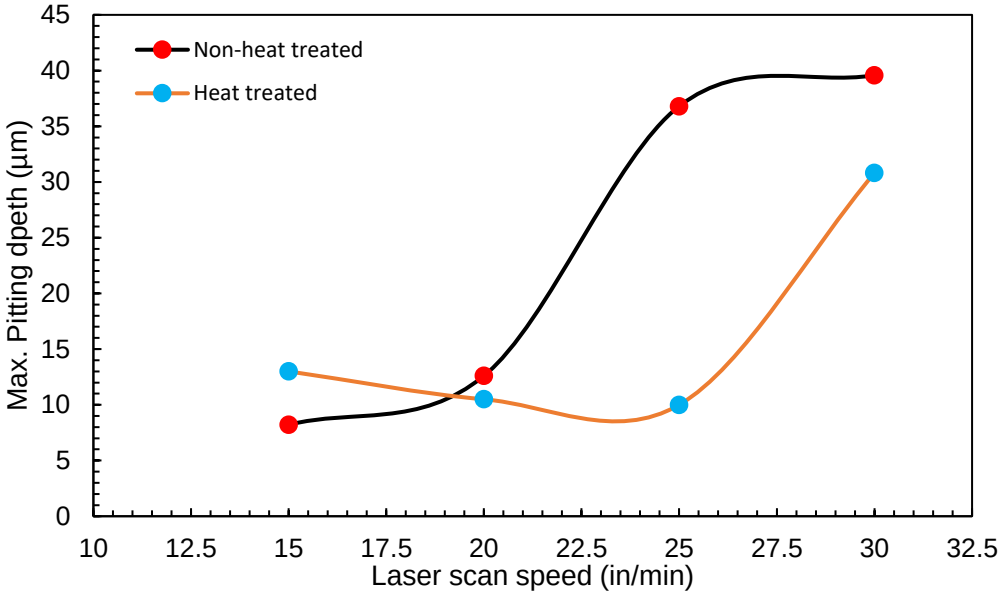

Fig. 5.47 Variation of maximum pitting depth with laser scan speed

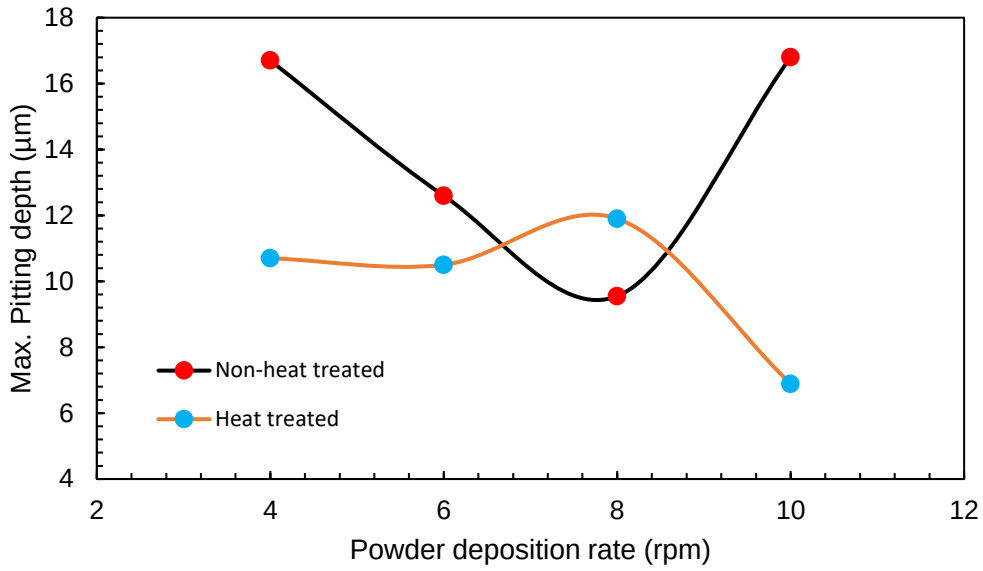

Fig. 5.48 Variation of maximum pitting depth with powder deposition rate

The corrosion rate and the corrosion penetration rate has been observed to decrease overall as the laser power increases. This is seen in the figures Fig. 5.40 and Fig. 5.41. This is also supported and substantiated by the observation of the maximum pitting depth with the laser power in the Fig. 5.46. As the laser power increases, the cooling rate reduces consequently. Higher cooling rates at lower levels of laser power induce more internal residual stresses and thermal distortions. Hence, the pitting corrosion rate decreases in an overall manner with an increase in laser power. This explanation is also substantiated with the reduction in the pitting depth with an increase in laser power as seen in the figures Fig. 5.40, Fig. 5.41, Fig. 5.46. However, the sample processed at 250 W recorded the minimal weight loss, and subsequently the minimum corrosion rate and corrosion penetration rate as observed from the figures Fig. 5.40 and Fig. 5.41. This discrepancy is explained due to the occurrence of inter-granular corrosion, which accounted for less pitting. This is depicted in Fig. 5.49. The corrosion mechanism is driven by inter-granular corrosion in the sample. This is supported by the observation for the illustration in the Fig. 5.49 (right image) with the sensitization of grain boundary and the formation of white patches of $M_{23}C_6$ complex chromium carbide only along the grain boundary [79].

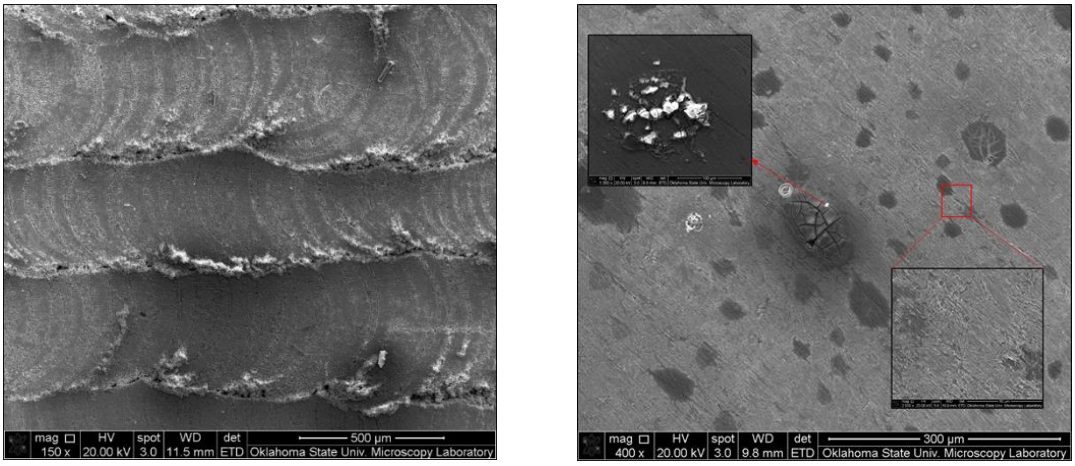

Fig. 5.49 SEM of sample processed at 250 W; as built (left), heat-treated (right)

The corrosion rate, corrosion penetration rate and the maximum pitting depth has been observed to decrease with the increase in the laser scan speed. This is coherently observed from the figures Fig. 5.42, Fig. 5.43 and Fig. 5.47. This phenomenon can be explained due to the decrease in the laser energy density as the laser scan speed increases. The incidence energy of the laser imparted to the metal alloy to melt and densify decreased when the laser energy density reduces as a consequence of laser scan speed increase.

The powder deposition rate exuded no direct coherent relationship with the pitting corrosion rate or pitting corrosion penetration rate. The powder deposition rate was also inconsistent with the pitting depth observed. This is observed from the figures Fig. 5.44, Fig. 5.45, Fig. 5.48. No direct correlation was observed with the variation of the powder deposition rate. However, the trend showed by the heat treated samples under the same processing conditions is similar to the ones exuded by the as-built samples. This observation vouches for the consistency of the experimentation.

Table.4: Pitting characteristics of wrought stainless steel 316 L

Properties	**Value**
Corrosion rate ($\mu g/m^{-2}s^{-1}$)	890.92
Corrosion penetration rate (CPR) (mm/year)	3.512
Maximum pitting depth (µm)	20.4

In all the conditions of LENS® processing, the additively manufactured samples exhibited improved pitting resistance that is manifested in the form of corrosion rate, corrosion penetration rate and maximum pitting depth. In the event of comparing the obtained properties of stainless steel 316 L additively manufactured in the LENS® process with that of wrought from the Table.4, it can be lucidly observed that the additive manufactured stainless steel 316 L is more resistant to corrosion than the wrought stainless steel 316 L. M. R. Stoudt el al also propounded that the additive manufacturing of 17-4 PH stainless steel imparts improved pitting resistance when compared with the wrought stainless steel 316 L [28]. They also observed improved pitting resistance as a consequence of the stress relieving heat treatment. In the wrought stainless steel 316 L, the pitting corrosion in the 10% dilute HCl solution is accompanied by inter-granular corrosion resulting in drastic cleavage by H_2 gas bubbles as well. As seen from the Fig. 5.50, the carbide particles were concentrated at the grain boundaries. The cleaving and pitting are vividly observed during the immersion corrosion of wrought stainless steel 316 L in 10% dilute HCl. Hence, the additively manufactured stainless steel 316 L is highly recommended in chloride pitting environment for marine applications for its durability against pitting corrosion.

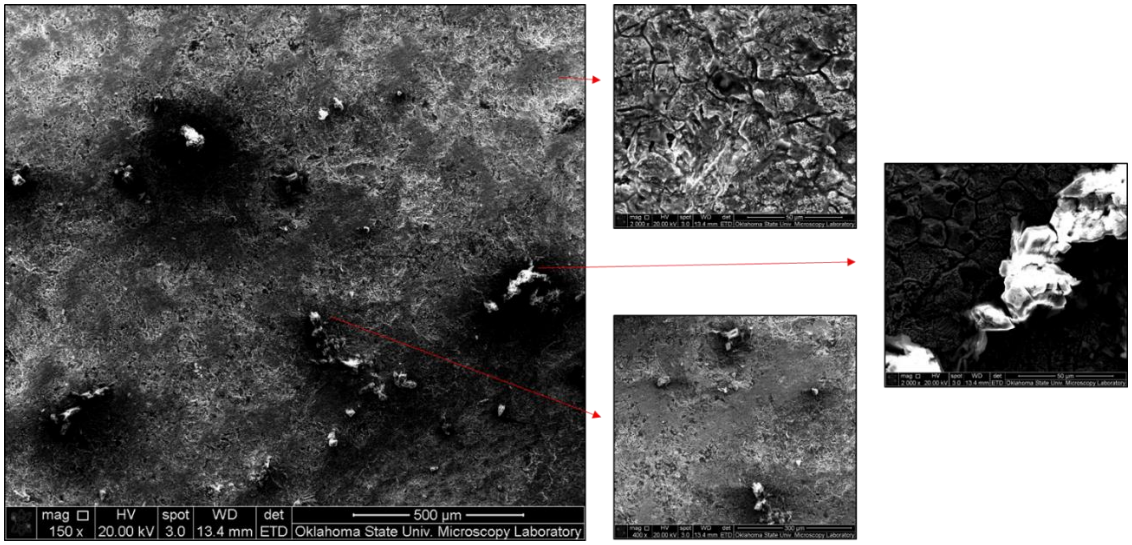

Fig. 5.50 SEM showing pitting and inter-granular corrosion in wrought stainless steel 316 L

CHAPTER VI

CONCLUSIONS

The main concern of the current research work was to investigate the effect of LENS® processing parameters namely laser power, laser scan speed, and powder deposition rate on the wear and corrosion properties of stainless steel 316 L additively manufactured using LENS® process. The results of wear and corrosion analysis of the stainless steel 316 L additively manufactured using LENS® process were compared to that of wrought stainless steel 316 L. The weight loss in the tribometry analysis was considered as the measure of wear and the potentiodynamic polarization corrosion potential was accounted as the direct measure of the corrosion resistance. The pitting depth, corrosion rate and corrosion penetration rate was used as the comparable quantities in the immersion corrosion test to study pitting resistance in dilute HCl environment. Further, the effect of surface roughness and heat treatment on the wear and corrosion properties was evaluated. The conclusions are presented in the following sections.

The wear mechanism in the stainless steel additively manufactured using LENS® process was identified as the formation and detachment of tribo-oxide layer. The wear mechanism was found to be affected predominantly by the densification of powder density and laser energy density. The wear was found to be inversely proportional to the laser power in the case of as-built surfaces and directly proportionality was observed when the effect of surface roughness is eliminated. Laser scan speed was found to directly influence the weight loss due to wear. Powder deposition rate was found to be inconsistent with the wear characteristics during LENS®. The wear performance of stainless steel 316 L additively manufactured in the LENS® process was found to be superior

to wrought-hot rolled stainless steel 316 L indicating processing parameters corresponding to high laser energy densities are conditions of good candidature for improved wear performance of the stainless steel 316 L additively manufactured in the LENS® process.

The corrosion potential of stainless steel 316 L additively manufactured in the LENS® process is lesser than that of wrought indicating that at the given LENS® parameters samples were more susceptible to corrosion. However, the corrosion potential of stainless steel 316 L additively manufactured in the LENS® process was higher than the wrought stainless steel 316 L at higher laser energy densities at 350 W power, laser scan speed 25 - 30 inch/min and powder deposition rate between 8 – 10 rpm. The increase in laser power increases the corrosion potential and subsequently the corrosion resistance. Increased powder densification with an increase in laser power also results in the increased corrosion resistance. The increase of corrosion resistance with an increase in laser scan speed was observed. The effect of powder deposition rate was found to be inconsistent with the corrosion properties. The findings suggest that LENS® processing at higher levels of laser power and laser scan speed enhance corrosion resistance of stainless steel 316 L relatively.

The stress relieving heat treatment was successful in minimizing the internal residual stresses, which manifested in the enhanced pitting corrosion resistance in the macroscopic scale. Hence, the stress relieving heat treatment is highly recommended for enhancing the pitting resistance of additively manufactured stainless steel 316 L. The effect of the LENS® processing parameters were consistent in both the as-built and heat treated samples. The pitting rate reduced overall with the increase in laser power. The pitting rate decreased with the increases in laser scan speed, which is accounted for the reduction in the energy imparted with the laser scan speed increase. The effect of powder deposition rate was observed to be inconsistent with the pitting corrosion characteristics. Overall, the additively manufactured stainless steel 316 L during the LENS® process exuded enhanced pitting corrosion properties relative to wrought stainless steel 316 L.

The future work in the direction of this research includes investigating the effect of processing parameters in the anodic polarization, cyclic polarization and optimization of processing parameters to obtain increased corrosion resistance and pitting resistance. The next future work in this research direction will also be the investigation of the effect of laser surface re-melting, laser surface alloying, laser shock peening on the corrosion characteristics of additive manufacturing of stainless steel 316 L during LENS® process.

REFERENCES

1. Callister, W.D., Material Science and Enginering, An Introduction 7ed, Department of Metallurgical Enginering The University of Utah, John Willey and Sons. 2007, Inc.
2. Budinski, K.G. and M.K. Budinski, Engineering materials. Nature, 2009. 25: p. 28.
3. Weiss, B. and R. Stickler, Phase instabilities during high temperature exposure of 316 austenitic stainless steel. Metallurgical and Materials Transactions B, 1972. 3(4): p. 851-866.
4. Standard, A., F2792 12a, 2012,". Standard Terminology for Additive Manufacturing Technologies," ASTM International, West Conshohocken, PA, doi. 10.
5. ASTM, F42 Factsheet.
6. Wang, Z., T.A. Palmer, and A.M. Beese, Effect of processing parameters on microstructure and tensile properties of austenitic stainless steel 304L made by directed energy deposition additive manufacturing. Acta Materialia, 2016. 110: p. 226-235.
7. Chen, X., et al., Microstructure and mechanical properties of the austenitic stainless steel 316L fabricated by gas metal arc additive manufacturing. Materials Science and Engineering: A, 2017. 703: p. 567-577.
8. Zhong, Y., et al., Additive manufacturing of 316L stainless steel by electron beam melting for nuclear fusion applications. Journal of Nuclear Materials, 2017. 486: p. 234-245.
9. Keicher, D.M., et al. Using the laser engineered net shaping (LENS) process to produce complex components from a CAD solid model. in SPIE. 1997.

10. Smugeresky, J., D. Keicher, and J. Romero, Laser engineered net shaping(LENS) process: optimization of surface finish and microstructural properties. Advances in Powder Metallurgy and Particulate Materials--1997., 1997. 3: p. 21.

11. Atwood, C., et al. Laser engineered net shaping (LENS): a tool for direct fabrication of metal parts. in Proceedings of ICALEO. 1998.

12. Griffith, M., et al. Free form fabrication of metallic components using laser engineered net shaping (LENS). in Solid Freeform Fabrication Proceedings. 1996. Proc. 1996 Solid Freeform Fabrication Symposium, Austin.

13. Wang, L., et al., Optimization of the LENS® process for steady molten pool size. Materials Science and Engineering: A, 2008. 474(1): p. 148-156.

14. Wang, L., S.D. Felicelli, and P. Pratt, Residual stresses in LENS-deposited AISI 410 stainless steel plates. Materials Science and Engineering: A, 2008. 496(1): p. 234-241.

15. Amano, R. and P. Rohatgi, Laser engineered net shaping process for SAE 4140 low alloy steel. Materials Science and Engineering: A, 2011. 528(22): p. 6680-6693.

16. Griffith, M., et al., Understanding thermal behavior in the LENS process. Materials & design, 1999. 20(2): p. 107-113.

17. Griffith, M.L., et al., Understanding the microstructure and properties of components fabricated by laser engineered net shaping (LENS). MRS Online Proceedings Library Archive, 2000. 625.

18. Zheng, B., et al., Thermal behavior and microstructure evolution during laser deposition with laser-engineered net shaping: part II. Experimental investigation and discussion. Metallurgical and Materials Transactions A, 2008. 39(9): p. 2237-2245.

19. Zheng, B., et al., Thermal behavior and microstructural evolution during laser deposition with laser-engineered net shaping: Part I. Numerical calculations. Metallurgical and materials transactions A, 2008. 39(9): p. 2228-2236.

20. Yasa, E. and J.-P. Kruth, Microstructural investigation of Selective Laser Melting 316L stainless steel parts exposed to laser re-melting. Procedia Engineering, 2011. 19: p. 389-395.

21. Mäkinen, M., et al., Preliminary comparison of properties between Ni-electroplated stainless steel parts fabricated with laser additive manufacturing and conventional machining. Physics Procedia, 2015. 78: p. 337-346.

22. AlMangour, B. and J.-M. Yang, Improving the surface quality and mechanical properties by shot-peening of 17-4 stainless steel fabricated by additive manufacturing. Materials & Design, 2016. 110: p. 914-924.

23. Mudge, R.P. and N.R. Wald, Laser engineered net shaping advances additive manufacturing and repair. WELDING JOURNAL-NEW YORK-, 2007. 86(1): p. 44.

24. Sun, Y., A. Moroz, and K. Alrbaey, Sliding wear characteristics and corrosion behaviour of selective laser melted 316L stainless steel. Journal of materials engineering and performance, 2014. 23(2): p. 518-526.

25. Stefanov, P., et al., XPS and SEM studies of chromium oxide films chemically formed on stainless steel 316 L. Materials Chemistry and Physics, 2000. 65(2): p. 212-215.

26. Mudali, U.K. and R. Dayal, Improving intergranular corrosion resistance of sensitized type 316 austenitic stainless steel by laser surface melting. Journal of Materials Engineering and Performance, 1992. 1(3): p. 341-345.

27. Khalfallah, I., et al., Microstructure and corrosion behavior of austenitic stainless steel treated with laser. Optics & Laser Technology, 2011. 43(4): p. 806-813.

28. Stoudt, M.R., et al., Influence of postbuild microstructure on the electrochemical behavior of additively manufactured 17-4 PH stainless steel. JOM, 2017. 69(3): p. 506-515.

29. Zietala, M., et al., The microstructure, mechanical properties and corrosion resistance of 316 L stainless steel fabricated using laser engineered net shaping. Materials Science

And Engineering A-Structural Materials Properties Microstructure And Processing, 2016. 677(EPFL-ARTICLE-225036): p. 1-10.

30. Gu, D., et al., Laser additive manufacturing of metallic components: materials, processes and mechanisms. International materials reviews, 2012. 57(3): p. 133-164.

31. Mercelis, P. and J.-P. Kruth, Residual stresses in selective laser sintering and selective laser melting. Rapid prototyping journal, 2006. 12(5): p. 254-265.

32. Yadollahi, A., et al., Effects of process time interval and heat treatment on the mechanical and microstructural properties of direct laser deposited 316L stainless steel. Materials Science and Engineering: A, 2015. 644: p. 171-183.

33. Yadollahi, A., et al., Effects of building orientation and heat treatment on fatigue behavior of selective laser melted 17-4 PH stainless steel. International Journal of Fatigue, 2017. 94: p. 218-235.

34. Kempen, K., et al., Microstructure and mechanical properties of Selective Laser Melted 18Ni-300 steel. Physics Procedia, 2011. 12: p. 255-263.

35. Liu, Z., et al., Crystal structure analysis of M2 high speed steel parts produced by selective laser melting. Materials Characterization, 2013. 84: p. 72-80.

36. Rafi, H.K., et al., Microstructure and mechanical behavior of 17-4 precipitation hardenable steel processed by selective laser melting. Journal of materials engineering and performance, 2014. 23(12): p. 4421-4428.

37. Montero Sistiaga, M., et al. Effect of heat treatment of 316L stainless steel produced by selective laser melting (SLM). in Proceedings of the 27th Annual International Solid Freeform Fabrication Symposium-An Additive Manufacturing Conference. 2016.

38. Luecke, W.E. and J.A. Slotwinski, Mechanical properties of austenitic stainless steel made by additive manufacturing. Journal of research of the National Institute of Standards and Technology, 2014. 119: p. 398.

39. Taha, M., et al., On selective laser melting of ultra high carbon steel: effect of scan speed and post heat treatment. Materialwissenschaft und Werkstofftechnik, 2012. 43(11): p. 913-923.

40. Cheruvathur, S., E.A. Lass, and C.E. Campbell, Additive manufacturing of 17-4 PH stainless steel: post-processing heat treatment to achieve uniform reproducible microstructure. Jom, 2016. 68(3): p. 930-942.

41. Niendorf, T. and F. Brenne, Steel showing twinning-induced plasticity processed by selective laser melting—An additively manufactured high performance material. Materials Characterization, 2013. 85: p. 57-63.

42. Song, B., et al., Vacuum heat treatment of iron parts produced by selective laser melting: microstructure, residual stress and tensile behavior. Materials & Design (1980-2015), 2014. 54: p. 727-733.

43. Gupta, R., et al., Metastable pitting characteristics of aluminium alloys measured using current transients during potentiostatic polarisation. Electrochimica acta, 2012. 66: p. 245-254.

44. Patella, R.F., J.-L. Reboud, and A. Archer, Cavitation damage measurement by 3D laser profilometry. Wear, 2000. 246(1-2): p. 59-67.

45. España, F.A., et al., Design and fabrication of CoCrMo alloy based novel structures for load bearing implants using laser engineered net shaping. Materials Science and Engineering: C, 2010. 30(1): p. 50-57.

46. Balla, V.K., et al., Porous tantalum structures for bone implants: fabrication, mechanical and in vitro biological properties. Acta biomaterialia, 2010. 6(8): p. 3349-3359.

47. Xue, W., et al., Processing and biocompatibility evaluation of laser processed porous titanium. Acta biomaterialia, 2007. 3(6): p. 1007-1018.

48. Krishna, B.V., S. Bose, and A. Bandyopadhyay, Fabrication of porous NiTi shape memory alloy structures using laser engineered net shaping. Journal of Biomedical Materials Research Part B: Applied Biomaterials, 2009. 89(2): p. 481-490.

49. Liu, W. and J. Dupont, In-situ reactive processing of nickel aluminides by laser-engineered net shaping. Metallurgical and materials transactions A, 2003. 34(11): p. 2633-2641.

50. Liu, W. and J. DuPont, Fabrication of carbide-particle-reinforced titanium aluminide-matrix composites by laser-engineered net shaping. Metallurgical and Materials Transactions A, 2004. 35(3): p. 1133-1140.

51. Xiong, Y., et al., Fabrication of WC–Co cermets by laser engineered net shaping. Materials Science and Engineering: A, 2008. 493(1): p. 261-266.

52. Collins, P., et al., Laser deposition of compositionally graded titanium–vanadium and titanium–molybdenum alloys. Materials Science and Engineering: A, 2003. 352(1): p. 118-128.

53. Balla, V.K., et al., Compositionally graded yttria-stabilized zirconia coating on stainless steel using laser engineered net shaping (LENS™). Scripta Materialia, 2007. 57(9): p. 861-864.

54. Balla, V.K., et al., Fabrication of compositionally and structurally graded Ti–TiO 2 structures using laser engineered net shaping (LENS). Acta biomaterialia, 2009. 5(5): p. 1831-1837.

55. Krishna, B.V. and A. Bandyopadhyay, Surface modification of AISI 410 stainless steel using laser engineered net shaping (LENS TM). Materials & Design, 2009. 30(5): p. 1490-1496.

56. Kunce, I., M. Polanski, and J. Bystrzycki, Structure and hydrogen storage properties of a high entropy ZrTiVCrFeNi alloy synthesized using Laser Engineered Net Shaping (LENS). International Journal of Hydrogen Energy, 2013. 38(27): p. 12180-12189.

57. Zheng, B., et al., Processing and behavior of Fe-based metallic glass components via laser-engineered net shaping. Metallurgical and Materials Transactions A, 2009. 40(5): p. 1235-1245.

58. Yin, H. and S. Felicelli, Dendrite growth simulation during solidification in the LENS process. Acta Materialia, 2010. 58(4): p. 1455-1465.

59. Kelly, S. and S. Kampe, Microstructural evolution in laser-deposited multilayer Ti-6Al-4V builds: Part I. Microstructural characterization. Metallurgical and Materials Transactions, 2004. 35(6): p. 1861.

60. Banerjee, R., et al., Microstructural evolution in laser deposited compositionally graded α/β titanium-vanadium alloys. Acta Materialia, 2003. 51(11): p. 3277-3292.

61. Banerjee, R., et al., Precipitation of grain boundary α in a laser deposited compositionally graded Ti–8Al–xV alloy–an orientation microscopy study. Acta materialia, 2004. 52(2): p. 377-385.

62. Semiatin, S., et al., Plastic flow and microstructure evolution during thermomechanical processing of laser-deposited Ti-6Al-4V preforms. Metallurgical and Materials Transactions A, 2001. 32(7): p. 1801-1811.

63. Gopagoni, S., et al., Microstructural evolution in laser deposited nickel–titanium–carbon in situ metal matrix composites. Journal of Alloys and Compounds, 2011. 509(4): p. 1255-1260.

64. Banerjee, R., et al., Microstructural evolution in laser deposited Ni–25at.% Mo alloy. Materials Science and Engineering: A, 2003. 347(1): p. 1-4.

65. Bauer, T., et al. Microstructure and mechanical characterisation of SLM processed Haynes® 230®. in Proceedings of the 26th Annual International Solid Freeform Fabrication Symposium. 2015. Laboratory for Freeform Fabrication and University of Texas at Austin.

66. HAO, Y.-w., et al., Effect of surface mechanical attrition treatment on corrosion behavior of 316 stainless steel. Journal of iron and steel Research, international, 2009. 16(2): p. 68-72.

67. de Lima, M.S.F. and S. Sankaré, Microstructure and mechanical behavior of laser additive manufactured AISI 316 stainless steel stringers. Materials & Design, 2014. 55: p. 526-532.

68. Meng, J., et al., Tribological behavior of 316L stainless steel fabricated by micro powder injection molding. Wear, 2010. 268(7-8): p. 1013-1019.

69. Quinn, T., Oxidational wear. Wear, 1971. 18(5): p. 413-419.

70. Tenwick, N. and S. Earles, A simplified theory for the oxidative wear of steels. Wear, 1971. 18(5): p. 381-391.

71. Quinn, T., Oxidational wear modelling: Part II. The general theory of oxidational wear. Wear, 1994. 175(1-2): p. 199-208.

72. Dogan, H., F. Findik, and O. Morgul, Friction and wear behaviour of implanted AISI 316L SS and comparison with a substrate. Materials & design, 2002. 23(7): p. 605-610.

73. Wang, X., M. Lei, and J. Zhang, Surface modification of 316L stainless steel with high-intensity pulsed ion beams. Surface and Coatings Technology, 2007. 201(12): p. 5884-5890.

74. Jakus, A.E., et al., Three-dimensional printing of high-content graphene scaffolds for electronic and biomedical applications. ACS nano, 2015. 9(4): p. 4636-4648.

75. Li, C. and T. Bell, Corrosion properties of active screen plasma nitrided 316 austenitic stainless steel. Corrosion Science, 2004. 46(6): p. 1527-1547.

76. Zou, J., et al., Mechanisms of hardening, wear and corrosion improvement of 316 L stainless steel by low energy high current pulsed electron beam surface treatment. Thin Solid Films, 2010. 519(4): p. 1404-1415.

77. Strehblow, H.-H. and P. Marcus, Mechanisms of pitting corrosion. Corrosion mechanisms in theory and practice, 1995: p. 201-238.

78. Pickering, H. and R. Frankenthal, On the mechanism of localized corrosion of iron and stainless steel I. Electrochemical studies. journal of the Electrochemical Society, 1972. 119(10): p. 1297-1304.

79. Matula, M., et al., Intergranular corrosion of AISI 316L steel. Materials characterization, 2001. 46(2-3): p. 203-210.

APPENDICES

The following research work is a collaboration with Dr. Rajeev Gupta and Kevin M. Nelson of the Department of Chemical and Bimolecular Engineering, The University of Akron.

1. Experimental Methods and Materials Procedure

a. Material

The material being studied is SS 316 L additive manufactured using Laser Metal Disposition. Three samples, as described in Table 1, were produced with different laser power levels

Table 1. AM SS 316 L processing conditions

Sample Name	Power of Laser used in production (Watts)
AM1	300
AM2	350
AM3	250

b. Sample Preparation

Each sample was tested on the top side as well the bottom where they were deposited on the initial base plate. The samples were first prepared to study the top sides. The preparation of each side to be studied included manual grinding with up to 1,200 grit SiC sandpaper (see Figure 1). The samples were then ultrasonically cleaned with ethanol (see Figure 2). Any storage of the samples.

was done within a desiccator (see Figure 3). In order to study the bottom sides of the samples, they were cut from the base plate using a saw (see Figure 4) making sure to keep the cut as close as possible to the base plate.

Figure 1. Machine used for manual grinding with SiC sandpaper

Figure 2. Ultrasonic cleaner

Figure 3. Desiccator used for sample storage

Figure 4. Saw used in bottom-side sample preparation

c. Sample Testing

The samples in this study underwent cyclic potentiodynamic polarization (CPP) to achieve polarization curves of the top and bottom sides of each sample. The samples were mounted in a three-electrode cell with 0.6 M NaCl (see Figure 5). The 1 cm^2 of sample surface area was the

working electrode with a platinized titanium mesh as the counter electrode and a saturated calomel electrode (SCE) as the reference electrode. The CPP test was run using EC Lab software and BioLogic equipment (see Figure 6). All CPP tests were run at a scan rate of 0.167mV/s. The samples were first cathodically polarized for 5 minutes to remove any atmospherically formed surface film and then polarized in the positive direction.

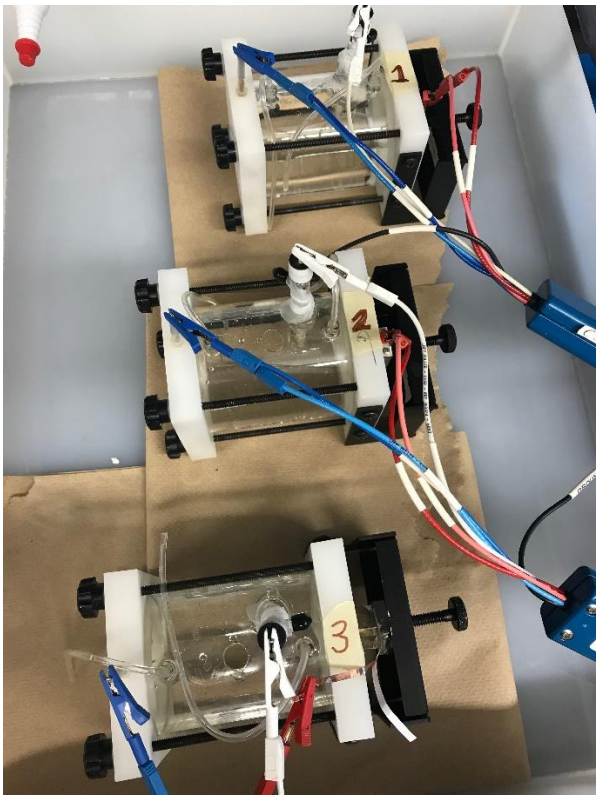

Figure 5. Submersion cells with 0.6 M NaCl

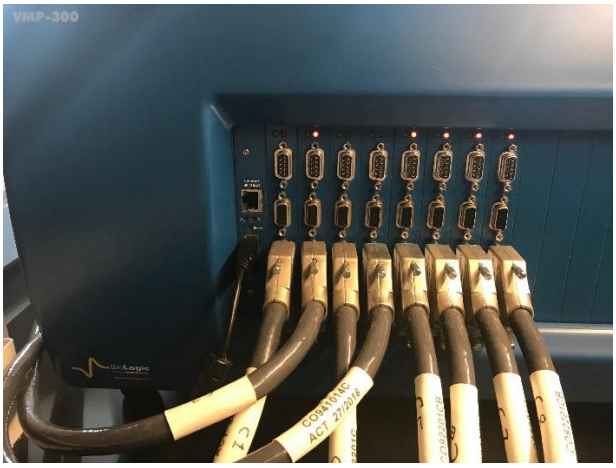

Figure 6. BioLogic equipment used during CPP testing

2. Results and Discussion

The CPP curves of the AM SS316L samples in 0.6M NaCl are shown with Figure 7 being the top sides and Figure 8 shows the results of the bottom sides of the samples.

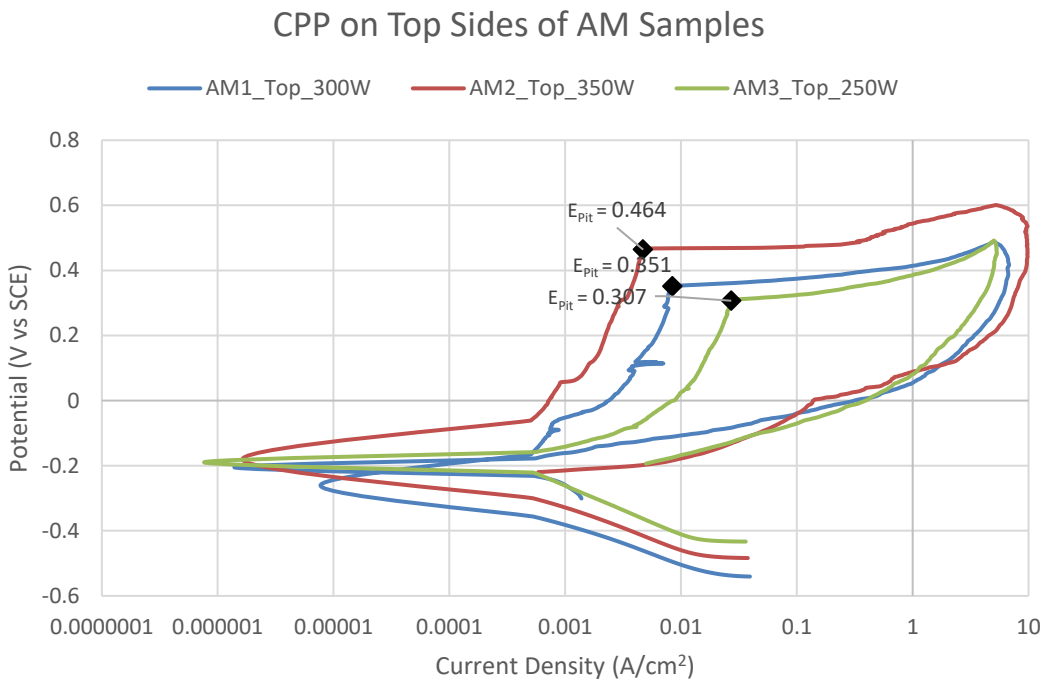

Figure 7. CPP on Top sides of AM samples

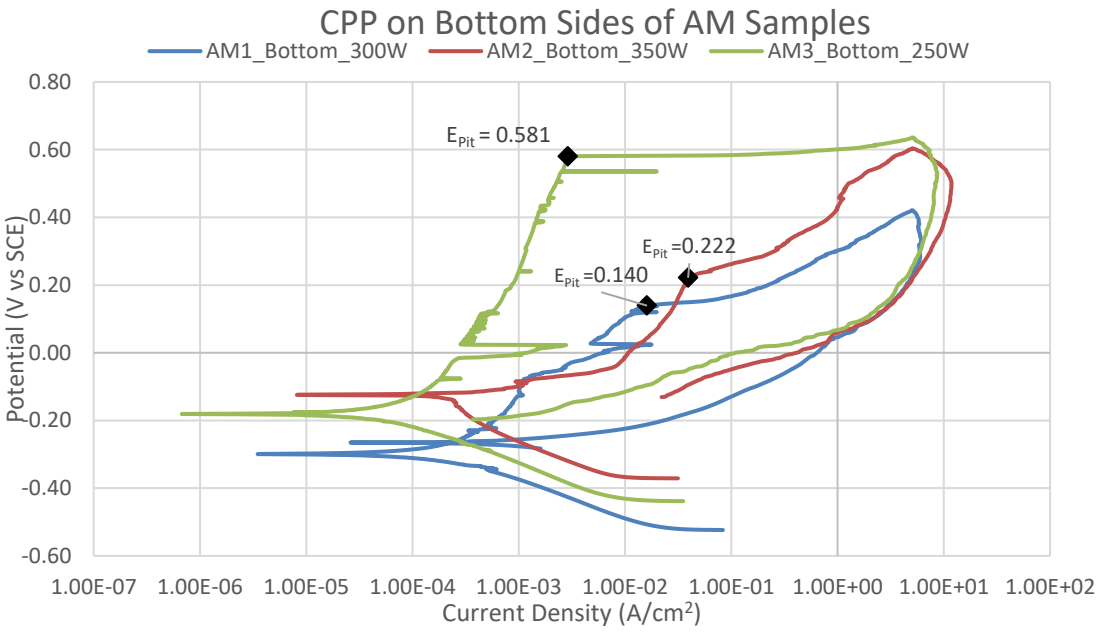

Figure 8. CPP on Bottom sides of AM samples

A comparison of the pitting, corrosion and passivation potentials along with corrosion current density is shown in Table 2. It is important to note that wrought SS316L has a stable pitting potential of 0.286 ±65 V vs SCE (see Figure 9). The AM1 sample showed passivation potentials above the open circuit potential.

Table 2. Comparison of CPP results

"Sample_Side_Power"	E_{Pit} (V vs SCE)	E_{corr} (V vs SCE)	i_{corr} (log A/cm^2)	E_{Pass} (V vs SCE)
AM1_Top_300W	0.351	-0.261	8.90E-05	-0.158
AM2_Top_350W	0.464	-0.180	7.06E-05	Below OCP
AM3_Top_250W	0.307	-0.190	3.32E-04	Below OCP
AM1_Bottom_300W	0.140	-0.299	2.38E-04	-0.265
AM2_Bottom_350W	0.222	-0.124	2.35E-04	Below OCP
AM3_Bottom_250W	0.581	-0.181	7.30E-05	Below OCP

The before (see Figure 10) and after (see Figure 11) photos of the top sides of the samples show the visual effects of the CPP test. The before (see Figure 12) and after (see Figure 13) photos of the bottom sides of the samples show the visual effects of the CPP test. In both cases, crevice corrosion is noticeable along with pitting. The evidence of crevice corrosion could be cause for some error in results and it is recommended that a lacquer be used in future studies to mitigate

this issue. Another important characteristic of the samples to note is that the bottom sides of the samples, especially with samples 1 and 2 (see Figure 12), were especially porous. This porosity is another likely source for error in results. The visual porosity is notably correspondent with the power used to produce the samples. This should be investigated in further studies.

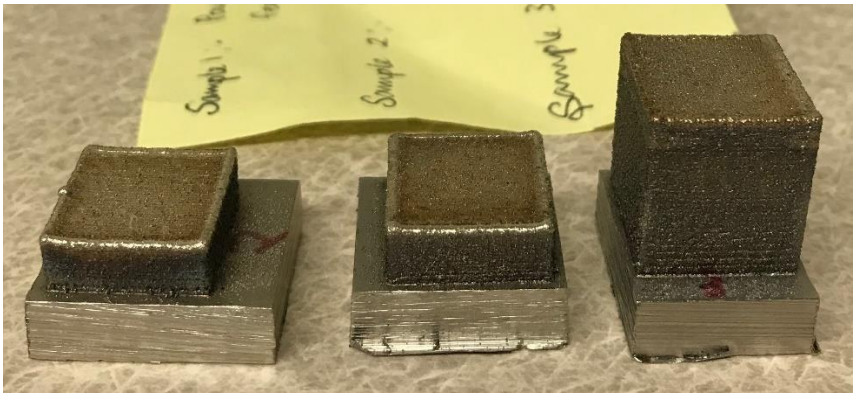

Figure 9. Top sides of AM samples before CPP testing

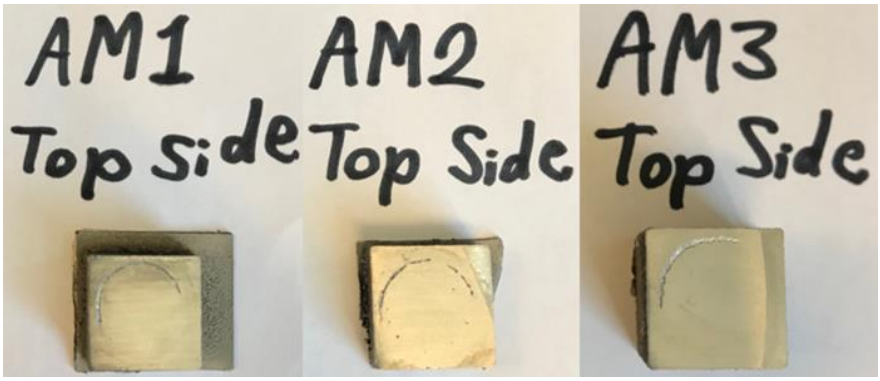

Figure 10. Top sides of AM samples after CPP testing

Figure 11. Bottom sides of AM samples before CPP testing

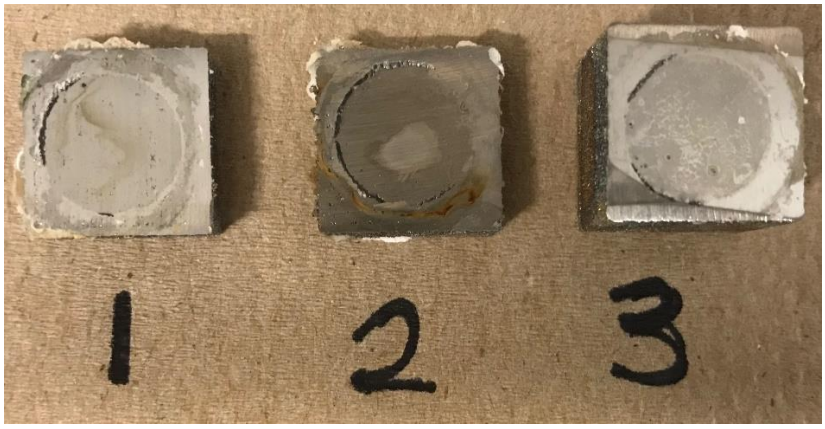

Figure 12. Bottom sides of AM samples after CPP testing

Through comparison of the two sample sides, it can determined that the top sides provide more accurate results. The top sides show a correlation between higher production power resulting in better (higher) pitting potentials. A similar conclusion may be drawn from the bottom sides of the sides, excluding sample 3 which seems to be erroneous.

3. Conclusion of appendix results:

Not much correlation can be seen with the thickness and corrosion resistance. The top sides of the samples seem to be more corrosion resistance than the bottom sides as well as less porous than the bottom sides.

VITA

NAVIN SAKTHIVEL

Candidate for the Degree of

Master of Science

Thesis: ANALYSIS OF WEAR AND CORROSION PROPERTIES OF 316 L STAINLESS STEEL ADDITIVELY MANUFACTURED USING LASER ENGINEERED NET SHAPING (LENS®)

Major Field: Mechanical and Aerospace Engineering

Biographical:

Education:

Completed the requirements for the Master of Science in Mechanical and Aerospace Engineering at Oklahoma State University, Stillwater, Oklahoma in July, 2018.

Completed the requirements for the Bachelor of Engineering in Mechanical Engineering at Anna University, India in 2016.

Experience:

Professional Memberships:

Toastmasters International